JGR Atmospheres

RESEARCH ARTICLE
10.1029/2025JD044985

Water Isotope Model Intercomparison Project (WisoMIP): Present-Day Climate

Hayoung Bong[1], Allegra N. LeGrande[2,3], Sylvia Dee[4], Jiang Zhu[5], Alexandre Cauquoin[6], Richard P. Fiorella[7,8], Qinghua Ding[9], Niels Dutrievoz[10], Masahiro Tanoue[11], Michelle Frazer[4], Mampi Sarkar[4], Cécile Agosta[10], Kei Yoshimura[6], Martin Werner[12], Atsushi Okazaki[13], Camille Risi[14], Hans Christian Steen-Larsen[15], Mathieu Casado[10], Sonja Wahl[10,15], Jesse Nusbaumer[5], John Worden[16], Stephen Good[17], Adriana Bailey[18], Matthias Schneider[19], Stefan Noël[20], Soumyajit Mandal[21], Kevin Bowman[16], Yifan Li[6], and Gavin A. Schmidt[2]

[1]NASA Postdoctoral Program Fellow, NASA Goddard Institute for Space Studies, New York, NY, USA, [2]NASA Goddard Institute for Space Studies, New York, NY, USA, [3]Center for Climate Systems Research, Columbia University, New York, NY, USA, [4]Department of Earth, Environmental, and Planetary Sciences, Rice University, Houston, TX, USA, [5]Climate and Global Dynamics Laboratory, NSF National Center for Atmospheric Research (NCAR), Boulder, CO, USA, [6]Institute of Industrial Science, The University of Tokyo, Kashiwa, Japan, [7]Earth and Environmental Sciences Division, Los Alamos National Laboratory, Los Alamos, NM, USA, [8]New Mexico Consortium, Los Alamos, NM, USA, [9]Department of Geography, University of California, Santa Barbara, Santa Barbara, CA, USA, [10]Laboratoire des Sciences du Climat et de l'Environnement (LSCE), IPSL, CEA–CNRS–UVSQ, Gif-sur-Yvette, France, [11]Meteorological Research Institute, Japan Meteorological Agency, Tsukuba, Japan, [12]Alfred Wegener Institute (AWI), Helmholtz Centre for Polar and Marine Research, Bremerhaven, Germany, [13]Institute for Advanced Academic Research/Center for Environmental Remote Sensing (CEReS), Chiba University, Chiba, Japan, [14]Laboratoire de Météorologie Dynamique (LMD) – IPSL, Sorbonne Université/CNRS/École Normale Supérieure – PSL/École Polytechnique – Institut Polytechnique de Paris, Paris, France, [15]Geophysical Institute, University of Bergen, and Bjerknes Centre for Climate Research, Bergen, Norway, [16]Jet Propulsion Laboratory, California Institute of Technology, Pasadena, CA, USA, [17]Department of Biological & Ecological Engineering, Oregon State University, Corvallis, OR, USA, [18]Department of Climate and Space Sciences and Engineering, University of Michigan, Ann Arbor, MI, USA, [19]Institute of Meteorology and Climate Research (IMK-ASF), Karlsruhe Institute of Technology, Karlsruhe, Germany, [20]Institute of Environmental Physics, University of Bremen, Bremen, Germany, [21]Space Research Organisation Netherlands, Leiden, The Netherlands

Key Points:

- Eight isotope-enabled climate models were nudged with the same winds and sea surface temperatures to compare water isotope simulations
- The ensemble mean best captures oxygen and hydrogen isotope patterns observed in global precipitation, vapor, snow, and satellite data
- Isotope changes from warming and climate modes reflect shifts in moisture transport, convergence, and large-scale atmospheric circulation

Supporting Information:

Supporting Information may be found in the online version of this article.

Correspondence to:

H. Bong,
hayoung.bong@nasa.gov

Citation:

Bong, H., LeGrande, A. N., Dee, S., Zhu, J., Cauquoin, A., Fiorella, R. P., et al. (2026). Water Isotope Model Intercomparison Project (WisoMIP): Present-day climate. *Journal of Geophysical Research: Atmospheres*, *131*, e2025JD044985. https://doi.org/10.1029/2025JD044985

Received 27 JUL 2025
Accepted 2 JAN 2026

Author Contributions:

Conceptualization: Hayoung Bong, Allegra N. LeGrande, Sylvia Dee
Data curation: Hayoung Bong, Allegra N. LeGrande
Formal analysis: Hayoung Bong, Allegra N. LeGrande
Funding acquisition: Allegra N. LeGrande, Sylvia Dee, Gavin A. Schmidt
Investigation: Hayoung Bong, Jiang Zhu, Alexandre Cauquoin, Richard P. Fiorella, Qinghua Ding, Niels Dutrievoz, Masahiro Tanoue, Michelle Frazer, Mampi Sarkar, Hans Christian Steen-Larsen, Mathieu Casado, Sonja Wahl, John Worden, Stephen Good, Adriana Bailey, Matthias Schneider, Stefan Noël, Soumyajit Mandal, Kevin Bowman
Methodology: Hayoung Bong, Allegra N. LeGrande

Abstract

We present the first results of the Water Isotope Model Intercomparison Project (WisoMIP), with Phase 1 focused on modern simulations (1979–2023) from a suite of isotope-enabled atmospheric general circulation models nudged to ERA5 reanalyzes. Water sources, mixing, and rainout history influence the isotopic composition of vapor and precipitation, making these simulations powerful tools for tracing the global water cycle. By prescribing identical winds, sea surface temperatures, and sea ice conditions, we isolate differences in water isotope behavior across models, controlling for variability in atmospheric dynamics and mean climate. Our analyses show that the ensemble mean best matches observations, as individual model errors cancel out to yield a more accurate representation of Earth's isotope distributions. We also evaluate trends and responses to major climate modes during the recent warming period, highlighting regional and temporal sensitivities in the isotope signals. These diagnostics extend beyond traditional model evaluation metrics (e.g., temperature, precipitation) to reveal uncertainties in physical processes and guide improvements in model parameterizations. The resulting modern nudged ensemble data set serves as a benchmark for isotope-enabled model development, satellite product comparison, and understanding of water cycle changes in a warming climate. Given its standardized design and broad participation, WisoMIP provides a valuable "isotope reanalysis" product for applications ranging from paleoclimate reconstruction to model tuning. Our work demonstrates the importance of coordinated isotope model evaluation in advancing the use of water isotopes as a diagnostic tool in climate science.

Plain Language Summary

Water molecules can have slightly different weights depending on the types of hydrogen and oxygen atoms they contain. These are called water isotopologues, or more simply, water isotopes. This study focuses on stable water isotopes, which serve as natural fingerprints that help track how water moves through the atmosphere, oceans, and land. They are especially useful for studying cloud processes, rainfall, temperature, and humidity, and can even reveal past climate conditions using ice cores or cave deposits. Many climate models can now simulate water isotopes, but they often produce different results, making it

Project administration: Sylvia Dee
Resources: Hayoung Bong, Allegra N. LeGrande, Kei Yoshimura, Gavin A. Schmidt
Software: Hayoung Bong, Allegra N. LeGrande, Jiang Zhu, Alexandre Cauquoin, Richard P. Fiorella, Qinghua Ding, Niels Dutrievoz, Masahiro Tanoue, Cécile Agosta, Kei Yoshimura, Martin Werner, Atsushi Okazaki, Camille Risi, Jesse Nusbaumer, Gavin A. Schmidt
Supervision: Allegra N. LeGrande, Sylvia Dee, Cécile Agosta, Kei Yoshimura, Martin Werner, Atsushi Okazaki, Camille Risi, Gavin A. Schmidt
Validation: Hayoung Bong, Michelle Frazer, Mampi Sarkar, Hans Christian Steen-Larsen, Mathieu Casado, Sonja Wahl, John Worden, Stephen Good, Adriana Bailey, Matthias Schneider, Stefan Noël, Soumyajit Mandal, Kevin Bowman
Visualization: Hayoung Bong
Writing – original draft: Hayoung Bong
Writing – review & editing: Allegra N. LeGrande, Sylvia Dee, Jiang Zhu, Alexandre Cauquoin, Richard P. Fiorella, Qinghua Ding, Niels Dutrievoz, Masahiro Tanoue, Michelle Frazer, Mampi Sarkar, Cécile Agosta, Kei Yoshimura, Martin Werner, Atsushi Okazaki, Camille Risi, Hans Christian Steen-Larsen, Mathieu Casado, Sonja Wahl, John Worden, Stephen Good, Adriana Bailey, Matthias Schneider, Stefan Noël, Soumyajit Mandal, Kevin Bowman

difficult to assess accuracy. To address this, the international Water Isotope Model Intercomparison Project (WisoMIP) tested several leading climate models by using the same conditions for winds, sea surface temperatures, and sea ice. This study compares WisoMIP model simulations over the period 1979–2023. By analyzing the models side by side and evaluating them against observations, the project identifies where the models agree, where they diverge, and why. These insights improve our understanding of water movement in the climate system and help refine climate models. The WisoMIP data set offers a valuable global resource for studying Earth's water cycle now and under future climate change.

1. Introduction

1.1. Scientific Background: Water Isotopes and the Hydrological Cycle

Stable water isotopologues—$H_2^{16}O$ (99.75%), $H_2^{18}O$ (0.20%), $HD^{16}O$ (0.01%), and $H_2^{17}O$ (0.04%)—which occur at these approximate abundances in natural waters, have long served as invaluable tracers in hydrological and atmospheric studies ((Dansgaard, 1964); see also (Bailey et al., 2025; Bowen et al., 2019; Dee et al., 2023; Galewsky et al., 2016) for topical reviews). During phase transitions such as evaporation and condensation, isotopic fractionation occurs. For example, heavier isotopologues (hereafter referred to as isotopes) will preferentially stay in or enter the condensed phase. Fractionation during phase change imprints a distinct isotopic signature that records the history of air masses, including a "memory" of moisture sources and rainout events (Rozanski et al., 1993).

Water isotopic variability is expressed in a δ notation as the ratio R of the heavier isotope (i.e., $H_2^{18}O$, $H_2^{17}O$, and $HD^{16}O$) on the lighter one ($H_2^{16}O$) relative to the standard reference Vienna Standard Mean Ocean Water (VSMOW) (Craig, 1961; Gonfiantini, 1978): $\delta = \left(\frac{R_{\text{sample}}}{R_{\text{VSMOW}}} - 1\right) \times 1000$. The reference standard V-SMOW has typical isotope ratios of 2005.20 ±0.43 ppm for $^{18}O/^{16}O$ and 155.76 ± 0.1 ppm for $D/^{1}H$. The resulting δ values, expressed in permil (‰), capture isotopic fractionation from both equilibrium and kinetic processes and thus serve as critical diagnostics of hydrological dynamics. Beyond standard oxygen and hydrogen δ values, higher-order isotopic tracers—such as deuterium excess (d-excess = $\delta D - 8 \times \delta^{18}O$) and ^{17}O-excess ($^{17}O\text{-excess} = \ln(\delta^{17}O + 1) - 0.528 \times \ln(\delta^{18}O + 1)$)—provide additional constraints, reflecting conditions like surface evaporative temperature and relative humidity at the condensation site (Luz & Barkan, 2005; Miller, 2002). Recent modeling studies have further explored the sensitivity of these tracers to hydrological processes and atmospheric dynamics (Extier et al., 2024; Risi et al., 2013; Zhang et al., 2025).

In the mid-to-high latitudes, variations in temperature on monthly and longer timescales strongly correlate with the abundances of heavier isotopes in precipitation (Sjolte et al., 2014). In contrast, at low latitudes, especially in coastal and open ocean regions, variability in isotope composition is more closely linked to precipitation intensity, sub-cloud rain evaporation, and convective and microphysical processes (Blossey et al., 2010; Lawrence et al., 2004; J.-E. Lee & Fung, 2008; Risi et al., 2008). Furthermore, a vertical lapse rate in isotopic composition emerges with altitude, reflecting the combined influences of temperature and elevation (Hu, Bailey, et al., 2022; Tripti et al., 2019; Yao et al., 2013). Recent advances in the observation and modeling of water vapor isotopes have highlighted their importance in constraining hydrological cycle processes on spatial and temporal scales (Bailey et al., 2025; Dee et al., 2023; Galewsky et al., 2016). For example, water isotope observations now play a crucial role in the evaluation and refinement of convective and cloud parameterizations in general circulation models, thus enhancing their ability to correctly represent the water cycle (Bony et al., 2008; Frazer et al., 2025; Hu et al., 2018; Nusbaumer et al., 2017; Ramos et al., 2022; Tharammal et al., 2017).

Beyond the canonical "temperature," "amount," and "altitude" effects, several known bottlenecks motivate a process-level approach to isotope interpretation. While these canonical relationships provide a useful first-order framework, their applicability is neither universal nor stationary. At high latitudes, the isotope–temperature relationship can become unstable across timescales, particularly on millennial scales, owing to precipitation seasonality, source and pathway changes, and inversion-layer and post-depositional effects (He et al., 2021a; Jouzel et al., 1997; Werner et al., 2000). In the East Asian monsoon region, isotopes in precipitation can be weak or non-monotonic in their association with local precipitation amount, with a strong timescale dependence,

because circulation regime shifts, moisture-source variability, and rainout history dominate over local rain intensity (He et al., 2021b; Jing et al., 2025; Liu et al., 2014). More generally, disequilibrium between vapor and precipitation, sub-cloud evaporation, variable condensation height, and microphysical pathways can strongly modulate $\delta^{18}O$, δD, d-excess, and ^{17}O-excess in ways that vary by region and timescale. Recognizing these bottlenecks motivates more nuanced, process-aware interpretations that integrate observations with isotope-enabled models to quantify the roles of moisture source, transport, convective organization, and microphysics.

Given their close relationship with the water cycle, oxygen and hydrogen isotopes have been the backbone of paleoclimatology for reconstructing past hydroclimate conditions. The use of isotopes has led to the discovery of glacial-interglacial cycles, orbital-scale variations in monsoon systems, and abrupt climate changes. For example, water isotopes measured in high-latitude ice cores are primarily interpreted as indicators of temperature variations (Grootes et al., 1993), based on the empirical "temperature effect" (Dansgaard, 1964). Isotopes measured in low-latitude speleothems (Wang et al., 2001) and lake sediments (Tierney et al., 2008) have been linked to the isotopic composition of precipitation and interpreted as monsoon rainfall, based on the empirical "amount effect." More nuanced interpretations of isotope records have since been proposed (Jouzel et al., 1997; Konecky et al., 2019; Liu et al., 2014). Expanding on this perspective, we frame water isotopes as integrated tracers of circulation, seasonality, moisture source, rainout history, and microphysics, rather than as simple proxies of temperature or amount. In this light, improved understanding and quantification of isotopic processes, via targeted observations and coordinated isotope-enabled model experiments, are essential to enhance the usefulness of isotopes across modern and paleoclimate contexts and directly motivate the present work.

1.2. Development of Isotope-Enabled Atmospheric General Circulation Models and Need for Inter-Comparison

The advent of isotope-enabled atmospheric general circulation models (iso-AGCMs) has allowed researchers to simulate the behavior of heavy stable isotopes alongside the most abundant water isotope, $H_2^{16}O$, within Earth's climate system—which began with Joussaume et al. (1984). In subsequent decades, stable water isotopes have been incorporated into more than a dozen GCMs—such as LMDZ (Laboratoire de Météorologie Dynamique Zoom; Joussaume et al., 1984), GISS (NASA Goddard Institute for Space Studies ModelE; Jouzel et al., 1987), ECHAM (European Center Hamburg Model; Hoffmann et al., 1998), GENESIS (Global ENvironmental and Ecological Simulation of Interactive Systems; Mathieu et al., 2002), MUGCM (Melbourne University General Circulation Model; Noone & Simmonds, 2002), CAM (Community Atmosphere Model; J.-E. Lee et al., 2007; Nusbaumer et al., 2017) and the coupled CESM (Community Earth System Model; Brady et al., 2019), GSM (Global Spectral Model; Yoshimura et al., 2008), HadCM (Hadley Center Climate Model; Tindall et al., 2009), MIROC (Model for Interdisciplinary Research on Climate; Kurita et al., 2011), LOVECLIM (LOch–VEgét–CLIMat; Roche, 2013), SPEEDY-IER (Simplified Parameterizations, Primitive Equation Dynamics – isotope-enabled reconstructions; Dee et al., 2015), and NICAM (Nonhydrostatic Icosahedral Atmospheric Model; Tanoue et al., 2023). These and other modeling efforts were made possible by theoretical and methodological advances in tracer transport schemes (Chang & Yoshimura, 2015), ice and precipitation physics (Elsaesser et al., 2017; Graf et al., 2019), parameter tuning based on observations (Moncrieff et al., 2017; Rind et al., 2020), and data assimilation (Steiger et al., 2017; M. Schneider et al., 2024; Tada et al., 2021; Toride et al., 2021; Yoshimura et al., 2014).

However, significant uncertainties remain in fully capturing the dynamical and physical mechanisms that drive isotopic variability in Earth's hydrological cycle. Differences in cloud and convection parameterizations (Bony et al., 2008; Bolot et al., 2013; Field et al., 2014; J.-E. Lee et al., 2009; Nusbaumer et al., 2017; Ramos et al., 2022), model resolution (Werner et al., 2011), tracer advection schemes (Cauquoin, Risi, & Vignon, 2019), surface boundary conditions (Ayache et al., 2024; Tsai et al., 2019), and wind circulation patterns resulting from nudging to different reanalyzes (Bong et al., 2024) have led to notable variations in simulated isotope outputs. Such discrepancies complicate the interpretation of model results and confound isotope-based climate diagnostics. To address these challenges, an international team of water isotope-enabled modelers recently initiated the Water Isotope Model Intercomparison Project (WisoMIP) with the goal of coordinating standardized, physically based simulations across multiple isotope-enabled atmospheric climate models.

1.3. Overview of Previous Isotope-Enabled Model Intercomparison Efforts

The Stable Water Isotope Intercomparison Group (SWING) was established in the early 2000s to foster community coordination and promote systematic evaluation of iso-AGCMs (Werner et al., 2004). SWING1 provided a first multi-model intercomparison including GISS-ModelE, MUGCM, and ECHAM4 with objectives that included benchmarking isotope modeling capabilities, identifying observational gaps, and bridging modeling and observational efforts. Early inter-comparisons (Hoffmann et al., 2000; Jouzel et al., 2000), focusing on paleoclimate isotope–temperature relationships, laid the groundwork for this initiative, which was based on annual means (i.e., climatological averages over the full simulation period) and the seasonal cycle. At that time, satellite retrievals were not yet available for comparisons, and nudging fields were not applied, as they would have been limited to the NCEP-R1 product (Kalnay et al., 2018). Subsequently, SWING2 sought to capitalize on recent advancements in satellite retrievals of the isotopic composition of the atmosphere (Noone, 2012; Worden et al., 2006) and introduced a protocol for including nudged simulation experiments (Hoffmann et al., 1998; Kurita et al., 2011; J.-E. Lee et al., 2007; Risi et al., 2010, 2012; Schmidt et al., 2006; Tindall et al., 2009; Yoshimura et al., 2008). Although numerous reanalysis products—each with their own strengths, limitations, and consistency with observations—were used, SWING2 did not adopt a unified protocol specifying a single reanalysis product for nudging.

This paper introduces WisoMIP Phase 1, the natural successor to the earlier SWING1 and SWING2 initiatives. A third phase, initially envisioned as SWING3, has been restructured and formally launched under the new name WisoMIP to align more clearly with the naming conventions of broader intercomparison frameworks such as Coupled Model Intercomparison Project (CMIP) and to reflect its explicit focus on water isotopes. In practice, the historical sequence now reads: SWING1 (2004) → SWING2 (2012) → WisoMIP Phase 1 (2026), with future WisoMIP phases planned. WisoMIP has three working groups, each focused on different scientific questions: (a) the modern, nudged simulations working group; (b) the paleoclimate and future (high-CO_2) simulations working group; and (c) the high resolution modeling group. In this work, we present the first results from the Group 1, that is, the modern nudged simulations working group. Building on the lessons from SWING1 and SWING2, this first phase of WisoMIP—focused on simulations nudged to reanalysis—establishes a standardized, observationally constrained framework for present-day simulations, enabling more rigorous and direct intercomparison of water isotope behavior across models.

1.4. Objectives and Approach of WisoMIP Phase 1: Simulations Nudged to Modern Climatology

Reanalyses and sea surface products combine observations with model data, which themselves have biases. Examining the degree to which each reanalysis product performs best against various observational data sets yields mixed results: different products will perform better depending on the metric examined (Elsaesser et al., 2025; Trenberth et al., 2011). A recent study systematically explored how reanalysis diversity affects simulated isotopic fields by using multiple reanalyses within the same model and applying a single reanalysis across different iso-AGCMs, but this study did not yet encompass all existing isotope-enabled models (Bong et al., 2024). For this initial phase of WisoMIP, our primary goal is to identify the key sources of inter-model variability and to diagnose differences in isotope physics, rather than to exhaustively quantify sensitivity to the choice of reanalysis. Nevertheless, we conducted a brief screening of multiple reanalysis products across a subset of models to select the most suitable nudging fields, using comparisons against a global precipitation–isotope data set. Accordingly, each Phase 1 model is nudged to a single reanalysis selected from these preliminary evaluations. The WisoMIP protocol is therefore designed not only to evaluate iso-AGCM performance within a consistent, observationally constrained framework, but also to provide a high-quality ensemble data set for broad community use, facilitating performance gains through ensemble averaging.

We produce present-day climate simulations (1979–2023) using eight iso-AGCMs: iCAM5 (Brady et al., 2019; Nusbaumer et al., 2017), iCAM6 (Fiorella et al., 2021), IsoGSM3 (Bong et al., 2024), GISS ModelE2.1 (Kelley et al., 2020; Zhang et al., 2025), MIROC5-iso (Okazaki & Yoshimura, 2019), ECHAM6-wiso (Cauquoin & Werner, 2021), LMDZ6 (Dutrievoz et al., 2025), and NICAM-WISO (Tanoue et al., 2023). All of the models were forced with identical sea surface temperature and sea ice boundary conditions and nudged toward a common circulation derived from ERA5 reanalysis (Hersbach et al., 2020). This standardized design controls for differences in atmospheric dynamics, enabling a direct, physically based intercomparison of isotopic outputs. The coordinated simulations produce an ensemble data set that allows us to: (a) evaluate model performance by

comparing outputs to surface and satellite-based observations, (b) quantify inter-model spread and expose key uncertainties in isotope diagnostics, and (c) leverage the ensemble mean—derived from multiple models to account for structural uncertainty—to enhance interpretation of isotope observations and to better constrain the processes driving their variability.

WisoMIP Phase 1 explores global patterns in atmospheric isotope ratios and their responses to climate variability and recent changes. Stable water isotopes offer crucial observational constraints on hydrological processes such as moisture recycling, atmospheric residence time, and precipitation efficiency. These processes are expected to change in a warming climate (Vystavna et al., 2021). With a suite of isotope-enabled nudged simulations in hand, we address the following key scientific questions:

1. To what extent do iso-AGCMs consistently simulate atmospheric water isotopes and their spatial patterns and variability under identical circulation and boundary conditions?
2. How have atmospheric isotope trends evolved during the recent warming period?
3. How do water isotopes respond to major modes of climate variability, such as the El Niño–Southern Oscillation, North Atlantic Oscillation, Arctic Oscillation, and Southern Annular Mode?

To explore these questions, the remainder of this paper is organized as follows. Section 2 describes the participating models, experimental design, nudging protocol, and observational data sets used for validation. Section 3 presents the results, including spatial patterns of annual mean isotopes, ensemble spread, long-term trends, comparisons with in situ and satellite observations, and isotopic responses to major climate modes of variability. Section 4 summarizes the key findings, discusses their broader implications, highlights remaining challenges, and offers recommendations for future model development and collaborative intercomparison efforts.

2. Models, Experimental Design, and Observations for WisoMIP

2.1. Reanalysis-Nudged Simulations

All participating models in WisoMIP followed a standardized experimental protocol to ensure consistent and rigorous inter-model comparison. Each model included prognostic tracers for water isotopologues and conducted atmosphere-only simulations.

Monthly model outputs were archived from 1979 to 2023, providing a comprehensive evaluation period for comparison with a range of in situ and satellite-based isotope observations. Each model archived a consistent set of variables describing water isotopes and hydrological fields, including $\delta^{18}O$, δD, d-excess, precipitation, evaporation, and moisture fluxes at the surface, pressure levels, and as vertically integrated quantities (Table S1 in Supporting Information S1). The simulations were driven by ERA5-based boundary conditions, including sea surface temperature, sea ice concentration, and three-dimensional atmospheric zonal and meridional wind components (Hersbach et al., 2020). These four variables constitute the core boundary conditions for this study. In addition, some models (iCAM5, IsoGSM3, ECHAM6-wiso, LMDZ6, and NICAM-WISO) also applied nudging to atmospheric temperature, whereas others did not, to avoid potential inconsistencies with their internal radiative schemes. Humidity and precipitation were not nudged because the primary objective of WisoMIP is to compare isotope-enabled model physics under consistent large-scale dynamical forcing. These identical boundary conditions ensured that large-scale circulation and synoptic variability were consistently represented across models.

Although the nudging fields were the same, the effective strength of nudging, diagnosed from the correlation coefficients between model-simulated and ERA5 winds, varied slightly among models. Because each model employs a different constraining approach for nudging strength, a direct quantitative comparison is not straightforward. Nevertheless, the correlations for zonal and meridional wind components, averaged across all pressure levels, follow the order iCAM5 (0.984), IsoGSM3 (0.980), ECHAM6-wiso (0.977), LMDZ6 (0.973), MIROC5-iso (0.971), GISS-E2.1 (0.964), iCAM6 (0.929), and NICAM-WISO (0.329). Conversely, the root-mean-square errors (RMSE) of zonal and meridional winds increase in the order ECHAM6-wiso (0.503), iCAM5 (0.547), IsoGSM3 (0.570), LMDZ6 (0.618), MIROC5-iso (0.712), GISS-E2.1 (1.010), iCAM6 (1.645), and NICAM-WISO (6.006), in m s^{-1}. These values (Figure S1 in Supporting Information S1), derived from monthly mean data for the evaluation period, indicate how closely each model reproduces the ERA5 reanalysis fields under the prescribed nudging setup.

While the primary boundary conditions were standardized across all models, an additional boundary condition concerns the isotopic composition of sea-surface water. Depending on the model setup, it was either fixed at 0‰ in iCAM5, iCAM6, IsoGSM3, NICAM-wiso, and MIROC5-iso, set to $\delta^{18}O = 0.5‰$ and $\delta D = 4‰$ in LMDZ6, or prescribed from observational climatology (A. N. LeGrande & Schmidt, 2006) in GISS-E2.1 and ECHAM6-wiso. This choice can influence the isotopic composition; the prescribed LS06 pattern (Figure S1a in Supporting Information S1) enriches atmospheric water vapor over the Atlantic (Figures S1b and S1d in Supporting Information S1) and, through prevailing westerlies, enhances precipitation $\delta^{18}O$ in regions downstream of areas with higher oceanic $\delta^{18}O$ (Figure S1c in Supporting Information S1). In contrast, lower Arctic values result in more depleted surface vapor (Figure S1b in Supporting Information S1), reflecting the lower $\delta^{18}O$ in evaporation, as inferred from Figures S2a and S2b in Supporting Information S1. The resulting differences generally remain within about 0.75‰ over most land regions, suggesting a limited influence on large-scale atmospheric $\delta^{18}O$ patterns while still contributing to minor inter-model variations.

Atmospheric constituents such as greenhouse gases (GHGs) and aerosols followed the CMIP6 historical protocol from 1979 to 2014 and were extended beyond 2015 using either Representative Concentration Pathway (RCP) scenarios (Eyring et al., 2016), Shared Socioeconomic Pathway (SSP) greenhouse gas concentrations (Meinshausen et al., 2020), or observational data from the NOAA Global Monitoring Laboratory. Because sea surface temperature and atmospheric winds were consistently nudged to the ERA5 reanalysis, all models were forced with the same boundary conditions, resulting in nearly identical atmospheric temperature evolution, water vapor content, and long-term trends regardless of the specific greenhouse gas data set used. Although a common constraint on post-2015 greenhouse gas concentrations was not imposed, the use of nudged simulations is expected to minimize the influence of different GHG data sets across models, while acknowledging that minor discrepancies may still contribute to inter-model differences after 2015.

Most models followed the CMIP6 protocol, with the following specific configurations after 2015: iCAM5 (RCP 4.5), iCAM6 (SSP 3–7.0), ECHAM6-wiso (RCP 4.5), GISS-E2.1 (RCP 6.5), IsoGSM3 (constant CO_2 = 348 ppm), MIROC5-iso (NOAA Global Monitoring Laboratory record), NICAM-WISO (constant CO_2 = 393 ppm), and LMDZ6 (constant CO_2 = 368 ppm). For models with constant greenhouse gas concentrations, atmospheric temperature is constrained by nudging to ERA5, so that the simulated thermodynamic responses were primarily influenced by the reanalysis-based constraints and were less affected by differences in radiative forcing.

2.2. WisoMIP Climate Models

2.2.1. iCAM5

We use the isotope-enabled Community Earth System Model version 1.3 (iCESM) in an atmosphere–land-only configuration. This model version is capable of simulating stable water isotopes across all components, including the atmosphere, land, ocean, and sea ice (Brady et al., 2019). The atmospheric component is CAM5.3 (Neale et al., 2012; Nusbaumer et al., 2017), integrated on a finite-volume grid with a horizontal resolution of 2.5° longitude × 1.9° latitude and 30 hybrid vertical levels. The land component is CLM4 (Thornton, 2010; Wong et al., 2017), which shares the same horizontal resolution and includes 10 vertical soil layers, with the carbon–nitrogen biogeochemistry module activated. Monthly sea surface temperature and sea ice boundary conditions, as well as 6-hourly three-dimensional winds and temperatures (from the surface to the model top), are fully nudged toward ERA5 reanalysis at each time step using linear interpolation between time intervals. Other forcings such as solar radiation, ozone, and aerosols are held constant throughout the simulation period. This setup ensures that the model is driven by observed atmospheric, oceanic, and anthropogenic radiative forcing conditions.

2.2.2. iCAM6

Simulations in iCAM6 were conducted using a configuration of CESM2 with the atmosphere and land components active, and ocean sea surface temperatures and sea ice boundary conditions prescribed from the ERA5 reanalysis data set. The simulations employed a horizontal resolution of 0.9 × 1.25°, with 32 vertical levels extending from the surface to approximately 3 hPa on hybrid coordinates. Relative to iCAM5, iCAM6 features updated cloud microphysics (MG2.0; Gettelman and Morrison (2015), Morrison and Gettelman (2008)) and a different parameterization for shallow convection, turbulence, and warm clouds (CLUBB; Bogenschutz

et al., 2012). The simulation was nudged toward horizontal winds and surface pressure fields every 6 hr, with the nudging strength increasing as the model approaches the next ERA5 state. Evaporation from the ocean assumes a uniform isotope distribution equivalent to VSMOW. Isotopic fluxes from the land surface are handled using a two-layer bucket model described in Fiorella et al. (2021). Briefly, evaporation from soils or vegetation surfaces is treated as isotopically fractionating, while transpiration is not (e.g., Ehleringer & Dawson, 1992). For the fractionating land surface fluxes, the kinetic fractionation factor is calculated following Merlivat and Jouzel (1979), implemented in CAM by Nusbaumer et al. (2017), with the Reynolds number computed using friction velocity and roughness length from the land model. Isotopic fractionation in mixed-phase clouds is dependent on supersaturation, parameterized as $S = 1 - 0.002 \cdot T$. Further details on the simulation setup are provided in Fiorella et al. (2021).

2.2.3. IsoGSM3

IsoGSM (Isotope-incorporated Global Spectral Model) is an atmospheric general circulation model that incorporates stable water isotopes (e.g., $\delta^{18}O$ and δD) into global simulations of the hydrological cycle. Built upon the NCEP Global Forecast System, it simulates isotopic fractionation associated with atmospheric processes such as evaporation, condensation, and transport (Yoshimura et al., 2008). IsoGSM can be run with a spectral nudging technique that assimilates reanalysis data to reproduce realistic present-day atmospheric conditions (Yoshimura & Kanamitsu, 2008). In this study, IsoGSM3 (Bong et al., 2024) is configured with ERA5-based nudging to constrain horizontal winds and temperature and employs the Non-iteration Dimensional-split Semi-Lagrangian (NDSL) advection scheme (Chang & Yoshimura, 2015; Henry Juang & Hong, 2010; Yeo et al., 2025).

2.2.4. GISS-E2.1

Simulations were conducted using the fully coupled GISS-E2.1 GCM with a horizontal resolution of 2° latitude × 2.5° longitude, and 40 vertical levels extending from the surface to 0.1 hPa (Kelley et al., 2020). Compared to GISS-E2 (Schmidt et al., 2014), the standard E2.1 setup features improved handling of mixed-phase clouds, enhancements in the planetary boundary layer parameterization, and consistent enhancements in the rates of convective entrainment. The water tracers, including "normal" water ($H_2^{16}O$, $H_2^{18}O$, $HD^{16}O$ and $H_2^{17}O$), are integrated into the model for the land surface, sea ice, sea surface, and atmosphere. These isotopes are monitored throughout the entire water cycle and are transported alongside water in the model while undergoing isotope fractionations between phases (Schmidt, 1999; Schmidt et al., 2005; A. LeGrande & Schmidt, 2009). The kinetic isotope fractionation typically used in GISS-E2.1 is Merlivat and Jouzel (1979), and the supersaturation factor, parameterized as $S = 1 - a * T$, is 0.003. Parameterizations for this version of the GISS model are further explored in Zhang et al. (2025).

2.2.5. MIROC5-iso

Simulations were performed using MIROC5-iso (Okazaki & Yoshimura, 2017, 2019), an isotope-enabled version of MIROC5 (Watanabe et al., 2010). Stable water isotopes ($H_2^{18}O$, $HD^{16}O$) were incorporated into atmospheric and land-surface components. Fractionation at phase transitions generally assumes equilibrium, except for kinetic fractionation at open-water evaporation (Merlivat & Jouzel, 1979), supersaturated ice formation below −20°C ($S = 1 - 0.002T$), and evaporation from raindrops (Stewart, 1975; Yoshimura et al., 2008). For cloud microphysics, the isotopes are incorporated following Federer et al. (1982) and Blossey et al. (2010). The land-surface model MATSIRO (Nitta et al., 2014; Takata et al., 2003) includes six soil layers, one canopy (with five leaf layers and one trunk), and up to three snow layers, considering both equilibrium and kinetic fractionation during surface phase changes (Yoshimura et al., 2006). The model simulations used a T42 horizontal resolution (approximately 280 km at the equator) with 40 vertical layers, constant isotopic compositions for sea surface water (0‰) and sea ice (3‰) as in Joussaume and Jouzel (1993).

2.2.6. ECHAM6-wiso

ECHAM6 (Stevens et al., 2013) is the sixth generation of the atmospheric general circulation model ECHAM, developed at the Max Planck Institute for Meteorology. It consists of a dry spectral-transform dynamical core, a transport model for scalar quantities other than temperature and surface pressure, a suite of physical parameterizations for the representation of diabatic processes, and boundary data sets for externalized parameters, such as

trace gas and aerosol distributions and land surface properties. The implementation of the water isotopes in ECHAM6, which is the atmospheric component of the atmosphere-ocean fully coupled model MPI-ESM (Giorgetta et al., 2013; Mauritsen et al., 2019), has been described and evaluated in detail by Cauquoin, Werner, and Lohmann (2019), and this model version has been labeled ECHAM6-wiso. At a later stage, Cauquoin and Werner (2021) updated the water isotope module of ECHAM6-wiso in several respects. The supersaturation equation has been slightly retuned to $S = 1.02 - 0.0045T$, the kinetic fractionation factors for evaporation over the ocean are now assumed to be independent of wind speed, and the isotopic content of snow on sea ice is taken into account for sublimation processes in sea-ice-covered regions. In this study, the ECHAM6-wiso version at T63L47 spatial resolution was used (approx. $1.9° \times 1.9°$ horizontal resolution and 47 vertical levels), with the top pressure level at 0.01 hPa.

2.2.7. LMDZ6

Simulations are performed with the AGCM LMDZ6, described in Hourdin et al. (2020), using version 20231022. trunk with the NPv6.3 physical package (Hourdin et al., 2023). This configuration is closely aligned with the atmospheric setup of the coupled climate model IPSL-CM6A (Boucher et al., 2020), developed for Phase 6 of the Coupled Model Intercomparison Project (CMIP6; Eyring et al., 2016). The simulation is conducted using LMDZ6's standard horizontal low resolution (LR) grid (2.0° in longitude and 1.67° in latitude). The vertical grid comprises 79 sigma-pressure levels, with the lowest atmospheric level approximately 10 m above ground level. The simulation is nudged toward 6-hourly three-dimensional fields of temperature and wind from the ERA5 reanalysis, using a relaxation time scale of 12 hr. Nudging is excluded below the sigma-pressure level equivalent to 850 hPa above sea level, allowing the model's physics and dynamics to operate freely within the boundary layer. Equilibrium fractionation coefficients between water vapor and liquid or ice are derived from Merlivat and Nief (1967), Majoube (1971a, 1971b). Kinetic fractionation effects are parameterized for sea surface evaporation following Merlivat and Jouzel (1979), and for ice condensation and supersaturation based on Jouzel and Merlivat (1984). The supersaturation is parameterized as a linear function of temperature for sub-freezing conditions, $S = 1 - 0.004 \cdot \left(T - T_{\text{freeze}}\right)$, with T_{freeze} equals to 273.15 K. The isotopic processes in LMDZ6iso are described in Risi et al. (2010) and evaluated in Antarctica in Dutrievoz et al. (2025).

2.2.8. NICAM-WISO

NICAM-WISO is the isotope-enabled version of the Non-hydrostatic Icosahedral Atmospheric Model (NICAM; Satoh et al., 2008, 2014), which employs an icosahedral grid enabling arbitrarily high horizontal resolution via recursive subdivision (Satoh et al., 2014). Its nonhydrostatic framework ensures conservation of mass, energy, and tracers. Core physical components include the MATSIRO land model (Takata et al., 2003), mstrnX radiation scheme (Sekiguchi & Nakajima, 2008), MYNN level 2 PBL scheme (Nakanishi & Niino, 2006; Noda et al., 2010), orographic gravity wave drag (McFarlane, 1987), ocean flux formulation (Louis, 1979), and surface roughness parameterizations (Fairall et al., 2003; Moon et al., 2007), along with a slab ocean. Cloud microphysics use NICAM's single-moment scheme (Tomita, 2008), with NSW6-Roh modifications for particle size distributions (Roh & Satoh, 2014; Roh et al., 2017). Isotope physics includes equilibrium fractionation for liquid–vapor and solid–vapor phases of $H_2{}^{18}O$ and HDO (Lamb et al., 2017; Majoube, 1971a, 1971b), molecular diffusivity (Merlivat, 1978), ice crystal formation (Jouzel & Merlivat, 1984), and open-water evaporation (Merlivat & Jouzel, 1979). Isotopic microphysics follow Blossey et al. (2010), incorporating saturation adjustment, raindrop evaporation, and vapor deposition. The ocean surface is assumed to have constant isotopic composition ($\delta^{18}O = \delta D = 0‰$), with no fractionation over land evapotranspiration. In WisoMIP simulations, the GL05 grid (~224 km resolution) was adopted. While this resolution tends to overestimate precipitation relative to higher resolutions, it has shown improved climatological performance in AMIP-type simulations (Tanoue et al., 2023).

2.3. Water Isotope Data Sets Employed for Validation

The observational data sets used to evaluate the model simulations include measurements of isotopes in precipitation and snow, near-surface water vapor isotopes, and atmospheric water vapor observed by satellites. Because these data sets differ in temporal coverage and sampling frequency, comparisons among them may involve mixed temporal sampling. This limitation may influence the interpretation of model–observation agreement.

Precipitation isotope observations: GNIP (Global Network of Isotopes in Precipitation), a long-term international monitoring program coordinated by the IAEA and WMO (IAEA/WMO, 2006), is used to validate model simulations of precipitation isotopes. From this data set, we selected sites with at least 12 consecutive months of valid isotope observations (i.e., non-missing values) between 1979 and 2020, resulting in a subset of 1,017 stations. The 12-month criterion ensures that each selected site captures at least one complete seasonal cycle of isotopic variability. For each month within this period, GNIP isotope values were directly paired with model-simulated precipitation isotopes at the nearest model grid point. If multiple GNIP sites were located within the same grid cell, their monthly isotope values were averaged to represent that grid. Months with zero precipitation were not treated as missing, as long as isotope values were reported. This approach ensures that sites with strong seasonality, such as those with dry months and little or no rainfall, were still included if continuous isotope records were available. Because GNIP observations are not spatially or temporally continuous, the comparison is limited by data gaps and uneven temporal coverage across sites. Nevertheless, this approach provides a consistent basis for evaluating modeled isotope variability at observational locations. Seasonal variability was removed prior to conducting regional timeseries correlation analyses between the isotopic composition of precipitation and precipitation rate and temperature.

Near-surface water vapor isotope observations: To complement the model evaluation and provide observational benchmarks for near-surface water vapor isotopic composition, we compile a comprehensive set of site-based measurements from published and ongoing studies. These observations span diverse geographic and climatic regions—including continental, coastal, and polar environments—and include both continuous and campaign-based records. The data set represents the most comprehensive collection to date of near-surface water vapor isotope measurements, primarily focusing on annual mean values of δ^{18}O and d-excess. It includes 47 stations where at least one full year of observations has been conducted, and it serves as the basis for the global distributions of vapor isotope composition shown in the study. The following references represent key sources contributing to this observational data set: Bonne et al. (2014), H. Steen-Larsen et al. (2015), H. C. Steen-Larsen et al. (2014), Jacob and Sonntag (1991), Bastrikov et al. (2014), Tremoy et al. (2012), Angert et al. (2008), Berkelhammer et al. (2016), Samuels-Crow et al. (2014), Galewsky (2018), Wen et al. (2010), X. Lee et al. (2006), Salamalikis et al. (2015), González et al. (2016), Christner et al. (2017), Wei et al. (2016), Lai et al. (2014), Dai et al. (2021), Tian et al. (2020), Kurita et al. (2015, 2012), Bailey et al. (2015), Leroy-Dos Santos et al. (2020), Vimeux et al. (2015, 2014, 2024), Wu et al. (2025), Chen et al. (2024), Landais et al. (2024), Bagheri Dastgerdi et al. (2021), Leroy-Dos Santos et al. (2023), Galewsky (2019, 2024), Bonne et al. (2020), Griffis et al. (2016), Laskar et al. (2014). Details on site location and elevation are summarized in Table S2 of Supporting Information S1, providing a useful benchmark for model–observation comparison.

Snow isotope observations in Antarctica: Stable isotope records from Antarctic snow are used to evaluate model skill in polar regions, where the spread among modeled water isotopes is the largest. Although the data set includes measurements collected across different years, seasons, and sampling strategies, we aggregated the available data into annual means to facilitate model comparison. We note that temporal sampling differences across sites (e.g., different years, seasons, and sampling strategies) may introduce additional uncertainty in the validation, although our comparison focuses primarily on large-scale spatial patterns. For this purpose, we utilized the Database of Antarctic Snow Isotopic Composition, which provides spatially distributed measurements of δ^{18}O and δD in surface snow. The data set includes 1,279 records, with 1,125 entries for δ^{18}O, 938 for δD, and 794 with both isotopes available, allowing the computation of deuterium excess (Masson-Delmotte et al., 2008). In addition, to evaluate seasonal isotope variations at a single site, we used precipitation isotope observations from Dome C, Concordia Station (75°06′ S, 123°21′ E; elevation 3,233 m a.s.l.), covering the period 2008–2017 (Dreossi et al., 2024; Ollivier et al., 2025; Stenni et al., 2016).

Satellite Observations: To evaluate the modeled water isotopes, we conduct additional validation using satellite-based retrievals from seven platforms: TES, AIRS, CrIS, IASI, GOSAT, GOSAT-2, and TROPOMI. These data sets collectively span the mid-troposphere to column-integrated estimates of deuterium content, and enable evaluation of both spatial and temporal aspects of the modeled δD and water vapor variability. The TES/Aura Level-2 HDO Lite Nadir product (version TL2HDOLN_6) provides vertically resolved deuterium profiles from September 2004 to September 2015 (Worden et al., 2006). Monthly gridded fields were created by applying filtering criteria based on degrees of

freedom (DOF) and cloud optical depth (COD) "relaxed" filter (DOF ≥ 0.5 and COD ≤ 3.6) followed the approach of Bailey et al. (2017). Complementary validation is carried out using deuterated water vapor retrievals from the TROPESS project. For AIRS, the TRPSYL2HDOAIRSORS product spans September 2002 to March 2020 (Bowman, 2023a), while the TRPSYL2HDOCRSRS product from CrIS covers December 2015 to May 2021 (Bowman, 2023b). These are summary-level data sets, which are quality-screened, integrated monthly fields intended for reanalysis and broad consistency assessments. They provide 1° and 5° spatial coverage but do not include averaging kernels, DOF, or a priori profiles, nor do they support custom filtering. In this study, they are used to provide broad spatial and temporal context under the same large-scale dynamical forcing, while more detailed model–data evaluations are being conducted in follow-on studies. The MUSICA IASI data set consists of individual retrievals, providing a large number of vertically resolved δD and H_2O profiles—approximately 350,000 profiles every 24 hr, which is significantly more than other satellite data sets. Each profile includes its own averaging kernel, resulting in a very large data set comprising roughly 1.5 billion individual profiles with associated averaging kernels and uncertainty estimates. In this study, we use the 1°× 1° regridded Level-3 product, which is a daily average of all individual retrievals within each grid cell and is available only at selected altitudes with the highest vertical sensitivity (3.0 km, 4.2 km, and 6.4 km). Both the full-resolution and Level-3 data sets are described in Diekmann et al. (2021). To complement these mid-tropospheric data sets, column-averaged δD and HDO retrievals from GOSAT (2009–2021) and GOSAT-2 (2019–2021) are also utilized. These were provided by Noël et al. (2022) and processed using the Fast atmOspheric traCe gAs retrievaL (FOCAL) algorithm (version 3.0). Both products incorporate rigorous quality and convergence filtering, with variable-specific thresholds for solar zenith angle, scattering optical depth, and retrieval uncertainties applied over land and ocean. Finally, we include total column δD retrievals from TROPOMI, which offers enhanced spatial coverage by incorporating both clear-sky and low-cloud scenes through a scattering-aware retrieval algorithm (A. Schneider et al., 2022). The data set has been validated against TCCON ground-based observations and aircraft campaigns, showing small biases in both H_2O and δD. Cloud classification is based on retrieved effective cloud parameters, including cloud height and optical thickness.

3. Results 1: Ensemble Mean and Validation

3.1. Mean State and Ensemble Spread

As a multi-model comparison data set, this section presents the annual means and ensemble spreads of each variable to facilitate interpretation and deepen understanding of the global hydrological cycle from a long-term perspective, while also providing insight into modeling uncertainties.

3.1.1. Key Climate Variables

The distribution of modeled water isotopes is primarily determined by fractionation processes related to temperature and humidity. Therefore, key variables of focus include surface temperature and water isotopes in precipitation, surface water vapor, and column precipitable water (Figure 1). To capture their seasonal behavior and inter-model spread, climatological means and standard deviations across four seasons (DJF, MAM, JJA, SON) are provided in Figures S3–S6 of Supporting Information S1. Since all models are forced with the same sea surface temperature and sea ice concentration fields, the spread in surface temperature is small over the ocean but increases over land (Figure 1b). This is primarily due to differences in atmosphere-land coupling, including the atmospheric conditions passed to the land surface (e.g., radiation, humidity, wind). Further spread is driven by the land surface schemes coupled with the atmosphere, which simulate varying temperatures and evaporation rates due to differences in evapotranspiration and water storage processes across models (Koster et al., 2006; Yuan et al., 2023).

The spread among models in their simulated water cycles arises mainly from differences in the representation of water vapor transport, condensation, and re-evaporation processes, particularly over the equatorial region where atmospheric moisture content is the highest. In these regions, solar insolation strongly heats the surface, trade winds transport moisture westward, and the Intertropical Convergence Zone (ITCZ) migrates seasonally (Figure 1g). This results in zonal Walker-type circulations, characterized by convection in rising branches and subsidence in descending branches, which strongly influence vertical and horizontal moisture redistribution

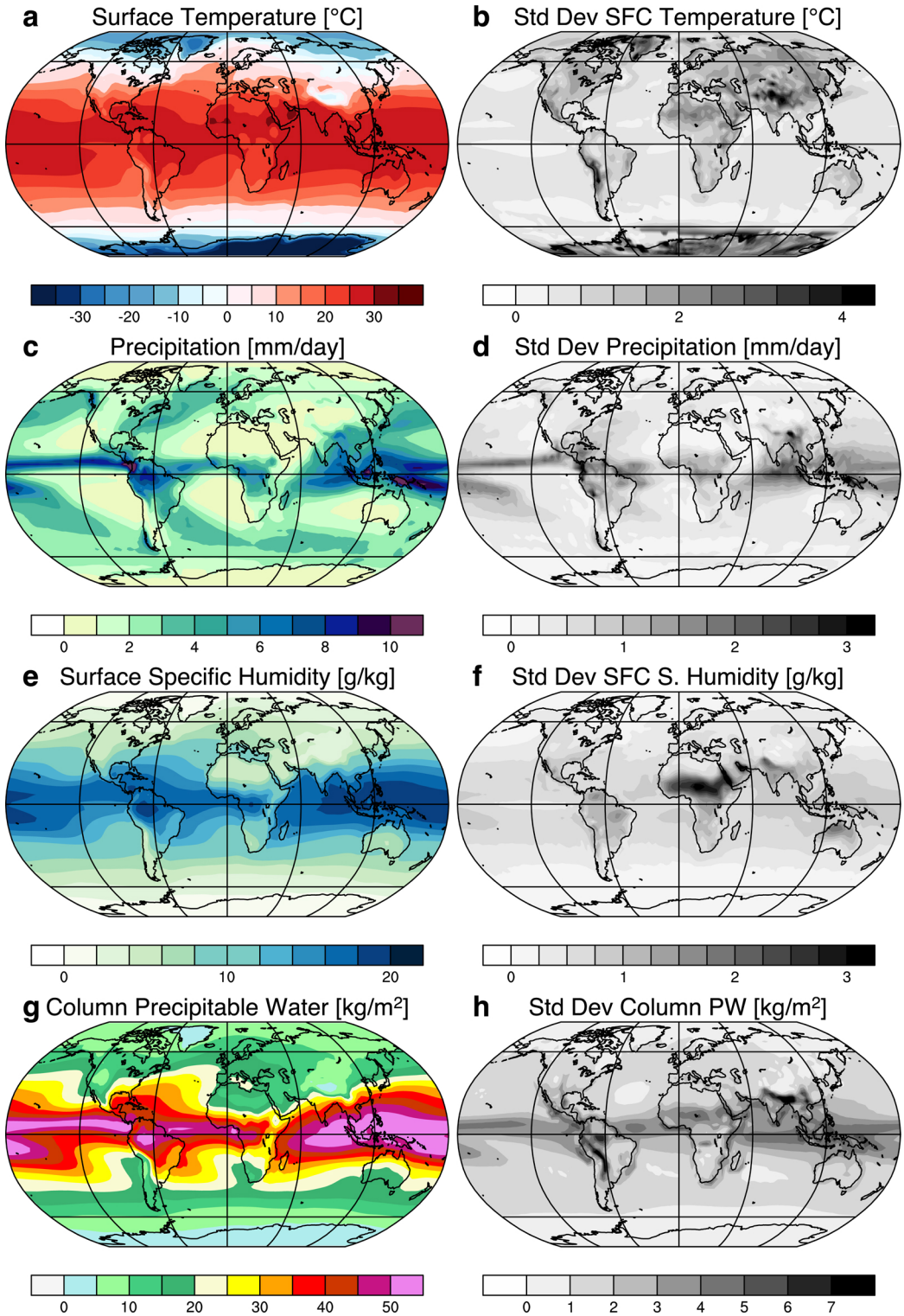

Figure 1. Annual mean and ensemble spread (standard deviation) of the WisoMIP ensemble, based on monthly data from 1979 to 2023. Variables shown are surface temperature (°C; a, b), precipitation (mm day^{-1}; c, d), surface specific humidity (g kg^{-1}; e, f), and vertically integrated precipitable water (kg m^{-2}; g, h). Panels (a, c, e, and g) show the ensemble mean; panels (b, d, f, and h) show the ensemble standard deviation.

(Figure 1c). Even though the same wind fields are used, substantial differences in model physics—not only in the physical parameter values but also in the representation of moist processes within each model's physics schemes—can result in divergent representations of large-scale moisture-related circulations across models (Figures 1d and 1h). For instance, over the African ITCZ region, a large inter-model spread is evident. This primarily reflects differences in the treatment of moist processes in monsoon regions, such as convection and re-evaporation, with the LMDZ model simulating a more humid atmosphere and the ECHAM model being comparatively drier. Notably, the spread is more pronounced in surface water vapor than in precipitable water, suggesting a possible contribution from differences in the coupled land-surface schemes—such as soil moisture availability and surface flux parameterizations.

While the inter-model spread in total water variables, as shown in Figure 1, appears relatively small over polar and high-altitude regions, this may partly reflect the low absolute values of these variables rather than consistent model behavior. Such environments can mask substantial relative differences between models. To complement the interpretation of the ensemble spread shown in the main figures, we further examined the normalized inter-model spread ($|\sigma|/|\mu| \times 100\ \%$) for key hydrological variables (Figures S7a, S7c, and S7e in Supporting Information S1). The normalization highlights regions where small mean values amplify relative variability, such as subtropical areas with weak rainfall or polar regions with low humidity. This additional analysis provides a scale-independent perspective on model spread and helps identify regions where absolute differences may underestimate relative inter-model variability.

In contrast, tracers sensitive to phase change and transport history, such as stable water isotopes, offer additional perspectives on hydrological differences across models, particularly in cold and dry regions. These isotopic diagnostics are further explored in the following sections.

3.1.2. δ^{18}O: Spatial Distribution and Inter-Model Variability

Water evaporated from the ocean become progressively depleted in heavier isotopes as it is transported poleward and inland through Rayleigh distillation (Figure 2). This leads to a clear meridional gradient in δ^{18}O, with the lowest values modeled over the cold, dry, and high-elevation interiors of high-latitude regions. In East Antarctica, δ^{18}O reaches approximately $-50‰$ in precipitation, $-55‰$ in surface water vapor, and $-70‰$ in column precipitable water, with a spatial distribution of surface snow isotope values similar to observations (Masson-Delmotte et al., 2008).

The seasonal contrast (JJA–DJF; Figure S8 in Supporting Information S1) shows that δ^{18}O is relatively enriched over Northern Hemisphere continents during boreal summer (JJA) and over Antarctica during austral summer (DJF). This hemispheric pattern is shaped by a variety of interacting processes. Rather than a simple dependence on temperature during condensation, δ^{18}O variability reflects changes in the sources and transport pathways of atmospheric moisture, the extent of evaporation and precipitation recycling, and regional circulation patterns. For example, in high-latitude continental interiors during JJA, enhanced local evaporation and shorter moisture transport pathways can lead to isotopic enrichment, while in Antarctica during DJF, relatively warmer summer conditions support increased poleward moisture transport and precipitation, resulting in higher δ^{18}O values. In tropical regions, δ^{18}O exhibits more complex and spatially variable behavior. Here, seasonal changes are heavily influenced by monsoon dynamics and the migration of the Intertropical Convergence Zone (ITCZ); in these settings, fractionation is controlled not just by temperature but also by convective intensity, moisture recycling, and shifting precipitation regimes.

This vertical ordering in δ^{18}O—column water vapor < surface vapor < precipitation—is consistently found across WisoMIP models (Figures 2a, 2c, and 2e) and likely reflects altitude-dependent processes such as condensation, re-evaporation, and near-surface exchange. While the precise mechanisms are complex and model-dependent, this pattern suggests that different components of the atmospheric water cycle retain distinct isotopic signatures as a result of the cumulative effects of processes such as altitude-dependent condensation, re-evaporation under subsaturated conditions, and near-surface exchange—each governed by specific thermodynamic and kinetic fractionation pathways. Because fractionation efficiency depends strongly on ambient humidity through the Rayleigh distillation process, the ability of each model to reproduce realistic humidity fields directly influences its simulated isotopic composition. In particular, differences in the fraction of remaining vapor (q/q_0) along transport pathways can lead to varying isotopic depletion rates, even under similar large-scale circulation

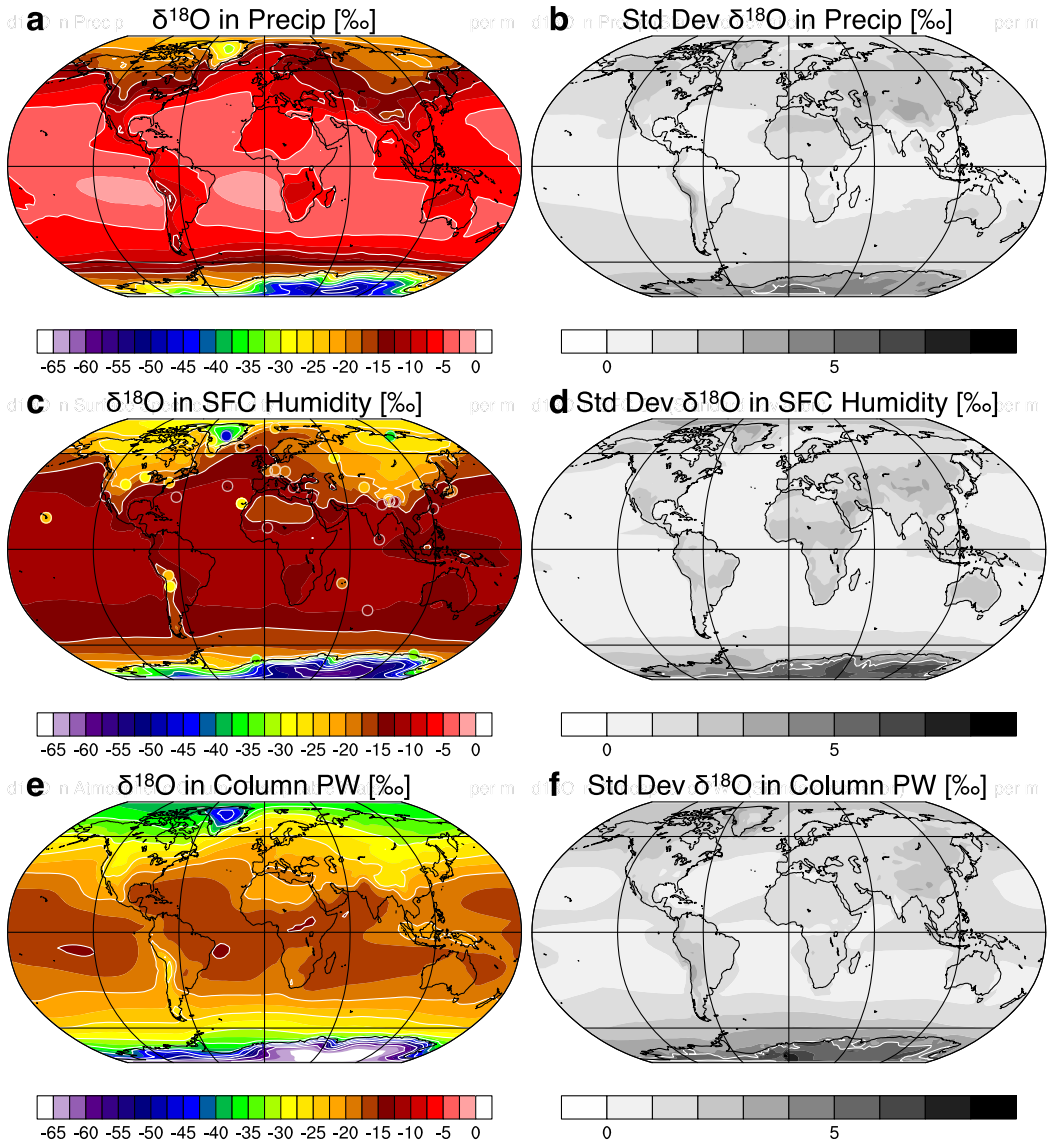

Figure 2. Annual mean and ensemble spread (standard deviation) of $\delta^{18}O$ (‰) from the WisoMIP ensemble, based on monthly data for 1979–2023. Panels (a, c, and e) show the ensemble mean, whereas panels (b, d, and f) show the ensemble standard deviation. To capture the wide $\delta^{18}O$ range from the surface to the atmosphere, panels (a, c, and e) use a piece-wise color scale. White contour lines with numeric labels matching the color-bar values help estimate local values on each global map. Variables: $\delta^{18}O$ in precipitation (a, b); near-surface water vapor (c, d); and column precipitable water vapor (e, f). In c, white-outlined circles mark annual-mean $\delta^{18}O$ from water-vapor isotope observations at 44 global stations compiled from published and unpublished sources. Statistical comparisons appear in Table S6 of Supporting Information S1.

patterns. Therefore, evaluating modeled water vapor content, particularly its column-integrated amount and potentially its vertical distribution, would provide a useful diagnostic for understanding inter-model differences in isotopic distributions.

Building on this pattern, the inter-model spread increases from precipitation to column water vapor, and is greatest over inland East Antarctica (Figures 2b, 2d, and 2f). The enhanced spread in these regions likely arises from accumulated differences along the moisture transport pathway in model parameterizations—such as supersaturation thresholds, phase transitions, cloud microphysics, and vertical mixing—under extremely cold and dry conditions. These parameterization differences induce distinct distillation pathways along the transport

trajectory, leading to varying degrees of progressive rainout and, ultimately, divergence in isotopic composition across models.

Consistent with this behavior, the normalized inter-model spread for $\delta^{18}O$ (Figures S7b, S7d, and S7f in Supporting Information S1) indicates that relative variability decreases toward high-latitude regions such as Antarctica, where lower mean isotope values reduce the apparent spread. This result suggests that the large ensemble spread seen in absolute terms mainly reflects the small magnitude of mean isotope values in cold and dry environments, rather than enhanced physical divergence among models. This highlights persistent challenges in simulating isotopic processes in polar environments and, to some extent, in validating them, since observational records can be affected by factors such as measurement uncertainty or local snow processes (Casado et al., 2016; Dütsch et al., 2019; Dietrich et al., 2023; Ollivier et al., 2025; H. Steen-Larsen et al., 2017; Wahl et al., 2022). Future cryosphere- and glacial-ice-specific analyses within the WisoMIP group will further explore these issues by explicitly linking modeled precipitation isotopes with snow and firn records, including the influence of post-depositional equilibration and related surface processes.

3.1.3. Deuterium Excess: Spatial Distribution and Inter-Model Variability

The spatial distribution of d-excess reveals key characteristics of the hydrological cycle beyond $\delta^{18}O$ alone, as it is sensitive to non-equilibrium fractionation during both evaporation and re-evaporation. On a global scale, d-excess exhibits a vertical ordering opposite to $\delta^{18}O$, with higher values in column precipitable water, intermediate values in surface water vapor, and the lowest in precipitation (Figures 3a, 3c, and 3e). This pattern reflects the cumulative effects of kinetic fractionation, which tend to enhance d-excess in vapor through surface evaporation, the re-evaporation of falling raindrops, and sublimation in cold regions.

Spatially, d-excess tends to be lower over oceans (generally below 10‰) and higher over land (typically above 10‰), driven by stronger vertical humidity gradients, land–atmosphere interactions such as the re-evaporation of precipitation after reaching the surface, and efficient local recycling. Lower d-excess values persist over the Southern Ocean, particularly within the Antarctic Circumpolar Current (ACC) than other regions, where cold and moist near-equilibrium conditions suppress evaporation and re-evaporation. Conversely, the highest d-excess values are simulated over inland East Antarctica, where extremely cold and dry conditions likely contribute to elevated d-excess through a combination of low-temperature distillation effects and kinetic fractionation. These values may also be influenced by how d-excess is calculated in models—particularly in formulations that do not apply a logarithmic definition. These polar regions also exhibit the largest inter-model spread in d-excess across all levels—precipitation, surface vapor, and column water vapor (Figures 3b, 3d, and 3f).

Although d-excess generally decreases with condensation toward precipitation, it remains highly sensitive to droplet exchange, microphysical processes, and both vertical and horizontal mixing pathways. Horizontal moisture transport, including long-range advection and interaction with precipitation and convection, contributes to isotope variability through the mixing of air masses with distinct water cycle histories. These processes collectively contribute to significant spatial variability and inter-model disagreement. Nevertheless, the ensemble mean shows consistent large-scale features that reflect the integrated influence of surface conditions and transport pathways. These patterns suggest that, despite inter-model spread, d-excess offers useful diagnostics for identifying regions dominated by kinetic fractionation and low-humidity moisture recycling. As such, interpreting modeled d-excess—especially in precipitation—requires caution, particularly in regions characterized by strong recycling, re-evaporation, or sparse observational constraints.

3.2. Model Validation

3.2.1. Surface Isotopic Variables: Precipitation and Surface Vapor Isotope

To evaluate individual model performance and the impact of ensemble averaging, we compare simulated precipitation isotopes with GNIP observations (IAEA/WMO, 2006) using correlation coefficients (Table S3 in Supporting Information S1) and variance-based metrics, as summarized in Taylor diagrams (Figure 4). Taylor diagrams provide a compact visual summary of model fidelity by directly displaying the correlation coefficient and the normalized standard deviation, defined as the ratio of the model to observed standard deviation ($\sigma_{model}/\sigma_{obs}$). These two metrics together allow the centered root-mean-square error (RMSE) to be inferred, which

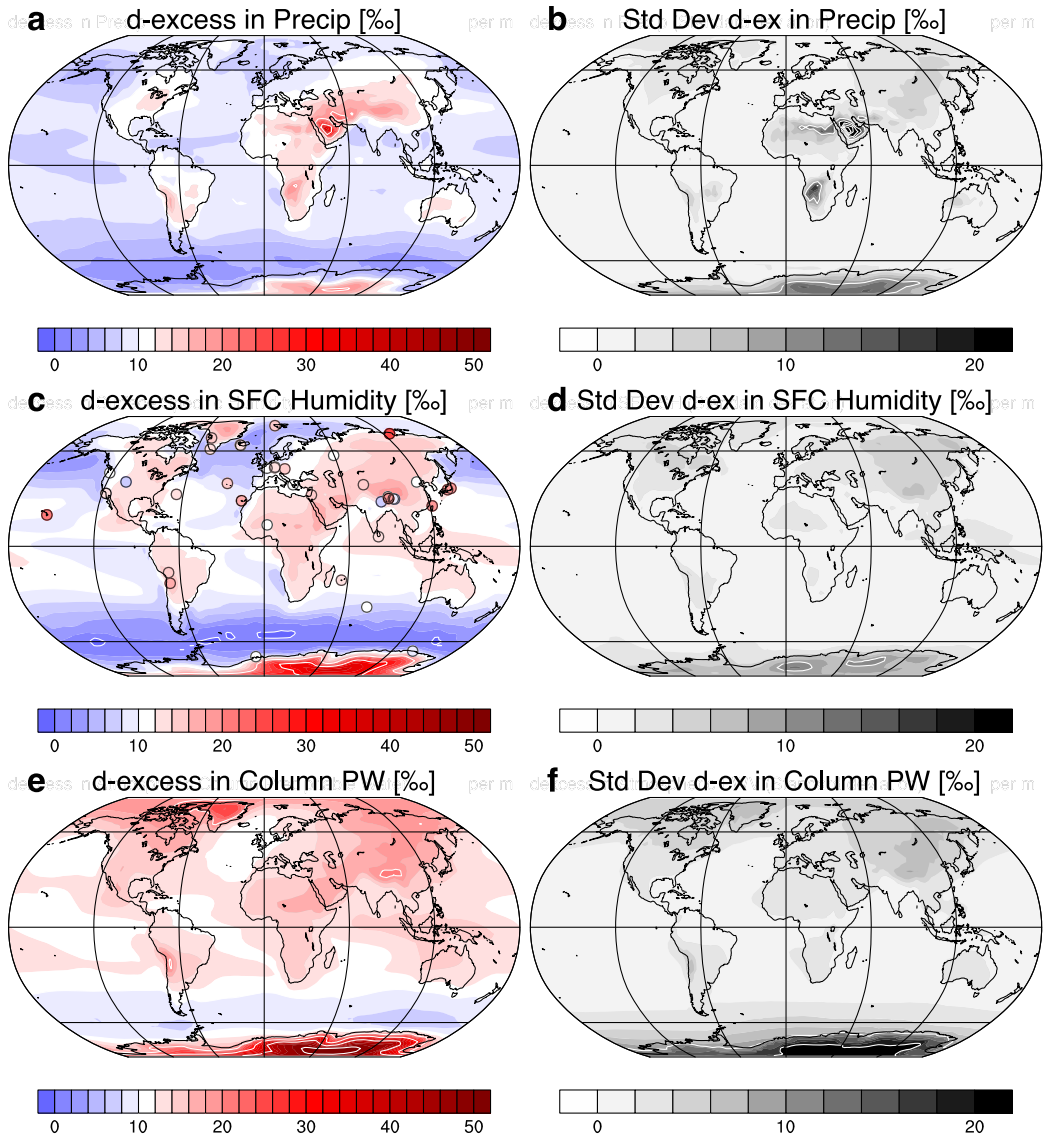

Figure 3. Annual mean and ensemble spread (standard deviation) of d-excess (‰) from the WisoMIP ensemble, based on monthly data from 1979 to 2023. Panels (a, c, and e) show the ensemble mean, and panels (b, d, and f) show the ensemble standard deviation. The variables are d-excess in precipitation (a, b), near-surface water vapor (c, d), and column precipitable water vapor (e, f). In panel (c), circular markers outlined in black indicate the annual mean d-excess values from water vapor isotope observations at 41 global stations, compiled from both published and unpublished sources. Statistical comparisons are provided in Table S6 of Supporting Information S1.

corresponds to the geometric distance between a modeled point and the ideal reference point on the diagram—where correlation and normalized standard deviation are both equal to 1.

To place the present analysis in context with earlier phases of isotope model intercomparison, we evaluated the progress in model skill across SWING1, SWING2, and WisoMIP1 (Table S4 in Supporting Information S1). Using annual mean GNIP observations interpolated to the WisoMIP grid, we find that the overall ability of isotope-enabled AGCMs to reproduce observed precipitation $\delta^{18}O$ has gradually improved over the past two decades. The mean spatial correlation increased from 0.8820 → 0.8988 → 0.9063, and the regression slope from 0.5889 → 0.6554 → 0.6754 from SWING1 to SWING2 to WisoMIP1. Although some individual models show reduced performance, the ensemble skill consistently improved, reflecting advances in both model physics and the use of a common ERA5-based nudging framework. For d-excess, the spatial correlation improved in four of

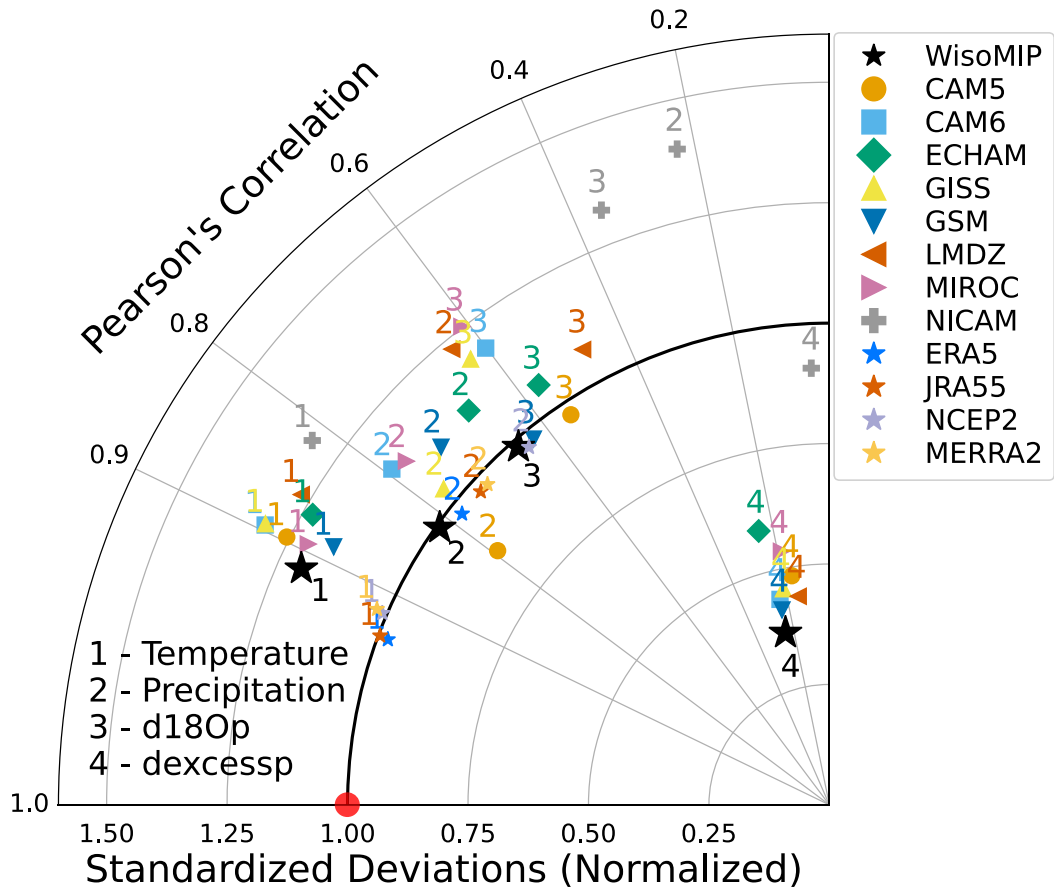

Figure 4. Taylor diagram summarizing model performance for surface variables, evaluated against observations from GNIP sites during the period 1979–2020. Reference data sets include CRU TS v4.06 (Harris et al., 2020) for near-surface temperature, GPCP v2.3 for precipitation (Adler et al., 2017), and GNIP for water isotopes. The numbered labels indicate (1) temperature, (2) precipitation, (3) $\delta^{18}O$ in precipitation ($\delta^{18}O_p$), and (4) d-excess in precipitation (d-excess$_p$). The diagram displays correlation coefficients and normalized standard deviations (model standard deviation divided by observed standard deviation), with centered root-mean-square error represented by the geometric distance from the reference point (correlation = 1, normalized SD = 1), shown as a red circle. Black stars represent ensemble means of WisoMIP models, which generally outperform individual models except for d-excess$_p$, where the correlation remains notably low. Smaller non-black stars represent reanalysis data sets (ERA5, MERRA-2, JRA-55, and NCEP-R2), which are evaluated only for temperature and precipitation based on their correlation and normalized standard deviation with respect to CRU and GPCP at GNIP sites.

the six SWING2 models that continued into the subsequent WisoMIP phase (ECHAM4 → ECHAM6-wiso, GISS-E → GISS-E2.1, IsoGSM → IsoGSM3, and MIROC3.2 → MIROC5-iso), but when all models are considered together, the overall WisoMIP1 correlation is lower than that in SWING1 and SWING2. This indicates that while isotopic fractionation processes for $\delta^{18}O$ have improved steadily, d-excess remains a persistent challenge, underscoring the need for enhanced representation of kinetic fractionation in future model generations. Despite differences among phases in simulation period, nudging strategy, and GNIP coverage that prevent a fully rigorous comparison, the results collectively demonstrate a clear trajectory of improvement and confirm that WisoMIP1 provides higher-resolution, more observationally consistent isotopic fields for present-day climate applications.

The iso-AGCMs generally reproduce the observed temporal variability in the following order of skill: temperature, precipitation, $\delta^{18}O_p$, and d-excess$_p$. The ensemble mean (excluding NICAM-WISO, which shows a correlation coefficient of 0.23 for precipitation, whereas the other models range from 0.64 to 0.80, and therefore falls below the 0.3 threshold for consistency with an observation-based data set.) improves upon the individual models for the first three variables by reducing temporal variability influenced by outlier simulations. Consequently, the

normalized standard deviation moves closer to 1.0, and the correlation coefficient increases beyond the values of any single model.

While the normalized standard deviation of temperature, precipitation, and $\delta^{18}O_p$ simulations tends to be up to 25% larger than observed values, d-excess shows the opposite behavior: its simulated variance is only about 50% of the observed variability. Although ensemble averaging modestly improves the correlation for d-excess, its value remains substantially lower than for the other variables. For example, the correlation coefficients of the ensemble mean with observations for temperature, precipitation, $\delta^{18}O_p$, and δD_p are 0.91, 0.82, 0.66, and 0.66, respectively, whereas that for d-excess$_p$ is markedly lower at just 0.25 (Table S3 in Supporting Information S1) at GNIP sites (Figure S9 in Supporting Information S1). This indicates that although ensemble means help reduce model-specific noise and improve statistical consistency, they do not resolve the fundamental challenges associated with accurately simulating d-excess due to its nature involving higher-order processes.

Additional analysis of selected WisoMIP models nudged with different reanalysis data sets reveals that the choice of atmospheric forcing clearly influences simulation quality (Table S5 in Supporting Information S1). In particular, simulations nudged with ERA5 reanalysis exhibit higher correlations with observations for $\delta^{18}O_p$ than those nudged with JRA-55 (Kobayashi et al., 2015), MERRA-2 (Koster et al., 2016), and NCEP-R2 (Kanamitsu, Ebisuzaki, et al., 2002; Kanamitsu, Kumar, et al., 2002), suggesting that the skill of isotopic modeling is sensitive not only to internal model physics but also to the quality of the driving meteorology and sea surface conditions. Interestingly, ensemble means that incorporate outputs from different reanalysis-driven simulations generally outperform any individual nudging case.

Meanwhile, the ensemble precipitation output (WisoMIP), represented by the large black star labeled "2" in Figure 4, shows better agreement with GPCP v2.3 precipitation (Adler et al., 2017) than any of the four reanalysis data sets, which are shown as smaller stars in the same figure, in terms of both correlation and temporal variability. This finding underscores a critical point: although reanalysis data sets are widely used as observational benchmarks, they still contain uncertainties in precipitation-related physical processes. In contrast, the model ensemble—nudged to the same ERA5 atmospheric fields in this study—produces outputs that are more consistent with observations and physically coherent, particularly with respect to simulated water isotopes. This highlights the added value of ensemble-based approaches in capturing hydrological variability and mitigating biases present in individual models or reanalyses.

Compared with the dense GNIP precipitation network, near-surface vapor isotope measurements are available at far fewer sites; the 44 stations plotted in Figure 2c (for $\delta^{18}O$) and the 41 stations in Figure 3c (for d-excess) nevertheless provide a valuable global benchmark at the annual-mean scale. Because these records sample the atmospheric boundary layer rather than condensed phases, their values are strongly influenced by local elevation and topographic setting, which are often underrepresented in coarse-resolution model grids. In areas of complex relief, coarse-resolution model grids therefore diverge more markedly from point observations. For $\delta^{18}O$ in particular, the models underestimate altitude-dependent depletion along upslope transport pathways, resulting in a positive mean bias of roughly +10‰ relative to station data (Table S6 in Supporting Information S1). This altitude-related mismatch highlights the need for higher-resolution simulations or explicit elevation corrections when evaluating near-surface vapor isotopes.

3.2.2. Surface Isotopic Variables: Antarctic Snow Isotope

The simulation spread of water isotopes is largest over Antarctica, where the climate is extremely cold and dry. This may partly reflect the strongly depleted isotope values in this region, which can amplify relative differences between models even when absolute variations are modest. Given the paleoclimatic importance of this region—particularly for interpreting ice core records—evaluating model performance here is critical. Using spatially extensive observations of annual-mean snow isotopes over Antarctica (Masson-Delmotte et al., 2008), we constructed scatter plots comparing observations with model outputs and calculated multiple statistical metrics: regression slope, correlation coefficient, root-mean-square deviation, and mean bias for $\delta^{18}O_p$, δD_p, and d-excess$_p$. The results, summarized in Table S7 of Supporting Information S1, show that the ensemble mean exhibits improved agreement with observations compared to individual models across all metrics, highlighting the value of multi-model ensembles in regions where individual model performance remains limited, likely due to

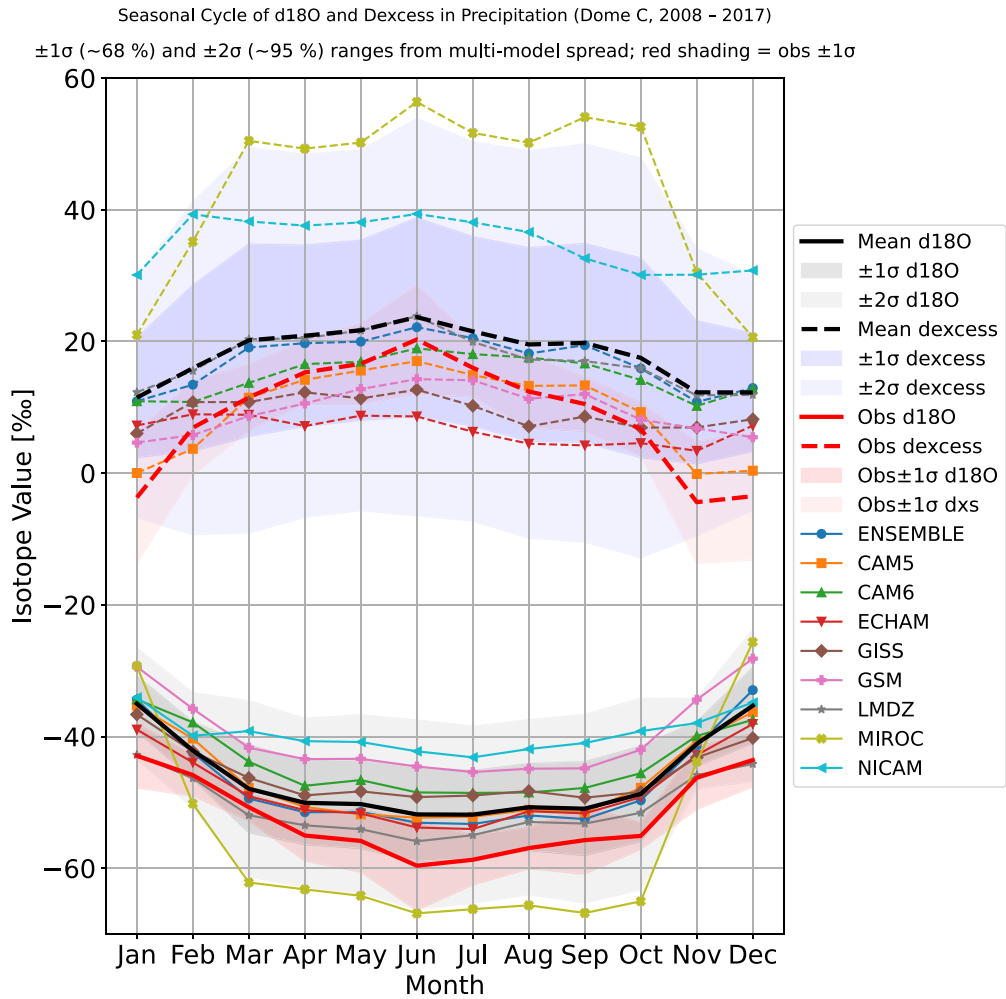

Figure 5. Seasonal cycle of Antarctic precipitation isotopes at Dome C (δ^{18}O and d-excess, 2008–2017 (Dreossi et al., 2024)). Black solid (dashed) lines show the multi-model mean of δ^{18}O (d-excess), with gray and light-gray shading indicating the inter-model spread ($\pm1\sigma$ and $\pm2\sigma$). Blue line with circular markers (ENSEMBLE) denotes the ensemble mean obtained by averaging isotope fields before delta conversion. Red solid (dashed) lines represent the observational mean; the surrounding light-red band denotes the observational uncertainty ($\pm1\sigma$). The most depleted δ^{18}O and highest d-excess occur during the austral winter, while inter-model spread is larger for d-excess.

challenges in simulating isotopic processes under extremely cold and dry conditions, as well as the effects of post-depositional modifications that are not fully captured in the models.

During the 10-year period from 2008 to 2017, seasonal variability of precipitation isotopes observed at Dome C (Dreossi et al., 2024) was compared with model outputs (Figure 5). For δ^{18}O, the models generally simulated less depleted values across all seasons compared to the observations. While d-excess values tended to fall within the observational uncertainty more consistently than δ^{18}O, the models exhibited a weaker seasonal cycle, particularly underestimating the summertime decrease during the austral summer. These comparisons with observations provide a useful benchmark for evaluating isotope-related model physics and suggest that future experiments—such as adjustments to parameterizations—could potentially improve model performance, particularly in this part of East Antarctica, where simulating the full seasonal cycle remains a challenge.

We additionally analyzed the seasonal cycles of precipitation isotopes over East Antarctica, focusing on δ^{18}O in precipitation (Figure S10 in Supporting Information S1), surface water vapor (Figure S11 in Supporting Information S1), and precipitable water vapor (Figure S12 in Supporting Information S1). The ensemble mean shows

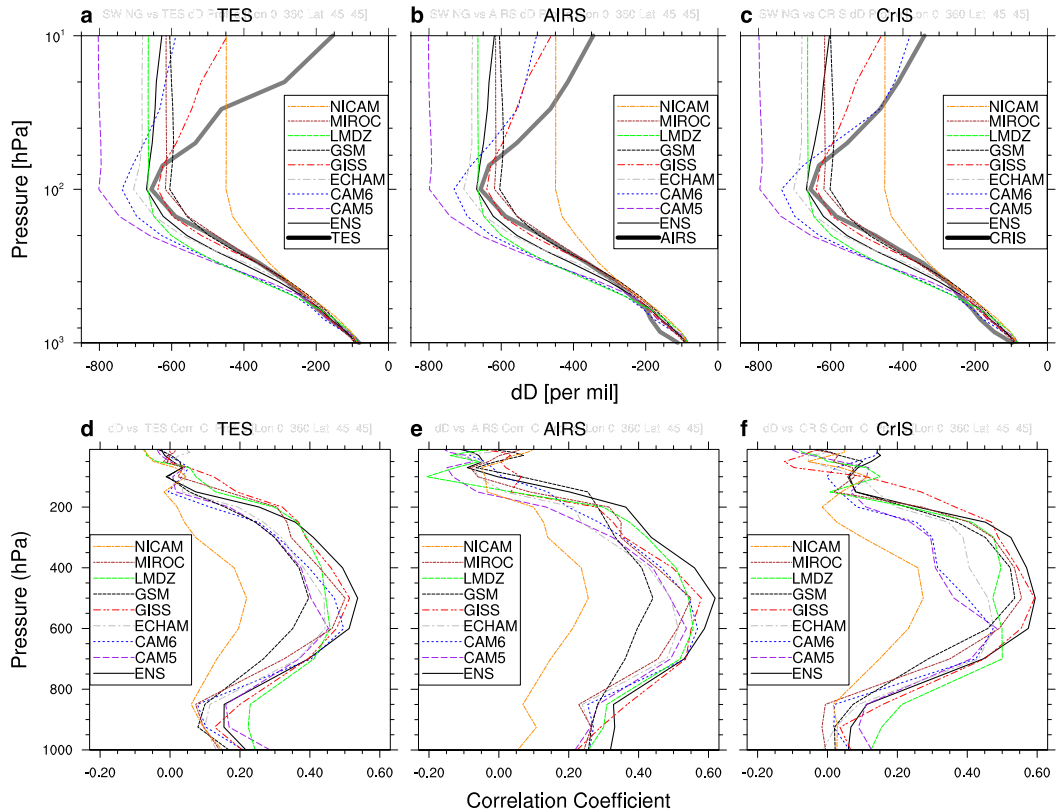

Figure 6. Vertical profiles of water vapor δD and the corresponding correlation with satellite observations, averaged over 45°S–45°N. Panels (a–c) show the vertical profiles of δD from isotope-enabled AGCMs and satellite retrievals: TES (a), AIRS (b), and CrIS (c). Panels (d–f) show the altitude-dependent correlation coefficients of temporal variability between models and satellite data for the same instruments: TES (d), AIRS (e), and CrIS (f). The ensemble mean (ENS) is shown as a black line. Summary statistics for the 500 hPa correlation values, including results from IASI, are provided in Table S8 of Supporting Information S1, and correlations for three additional column-integrated vapor isotope data sets—GOSAT, GOSAT-2, and TROPOMI—are presented in Table S9 of Supporting Information S1.

the most depleted δ^{18}O and the highest d-excess in July (austral winter), with opposite conditions in summer. Notably, the inter-model spread (± 1 standard deviation) of total precipitation isotopes (mostly snowfall) is about twice as large during winter than in summer—approximately 20 versus 10‰ for δ^{18}O, and 40‰ versus 20‰ for d-excess.

Furthermore, consistent with the Taylor diagram analysis showing lower temporal variability in d-excess than in δ^{18}O, the seasonal amplitude of d-excess (18.1‰; 14.9‰ in July to 24.7‰ in January) is about half that of δ^{18}O (9.8‰; from −52.1‰ in July to −34.0‰ in December). These findings suggest that the relatively weak seasonal signal and larger spread in d-excess may contribute to its poor model representation. This deficiency may arise from how models simulate kinetic fractionation during evaporation and re-evaporation, particularly over the Southern Ocean, where relative humidity, wind speed, and sea surface temperature strongly influence d-excess in the source vapor. In addition, simplified or inconsistent treatment of non-equilibrium processes and vertical mixing may further limit model performance. These factors should be considered in future efforts to improve d-excess simulations.

3.2.3. Atmospheric Isotopic Variables: Comparison With Satellite Retrievals

To evaluate the water vapor isotope delta values simulated by WisoMIP, we examined their vertical profiles (Figures 6a–6c) and the altitude-dependent area-averaged correlation coefficients of temporal variations (Figures 6d–6f), averaged over 45°S–45°N to reflect the main latitudinal coverage of satellite data and to avoid biases from limited accuracy and high cloud occlusion in high-latitude regions. The generally decreasing trend of

δD with altitude up to ~100 hPa is captured by both the models and the satellite retrievals. Above this level, δD increases, a reversal attributed to CH_4 oxidation by OH radicals that produces isotopically heavier water vapor and offsets Rayleigh-type depletion at lower pressures. Among the models, only iCAM6 and GISS-E2.1 represent this enrichment; other models keep δD low above 100 hPa.

However, we note that satellite averaging kernels were not applied to the model output in this study. This omission represents a known limitation, as the vertical sensitivity of satellite retrievals cannot be directly replicated by model data. As such, this comparison should be considered more qualitative than strictly one-to-one. Due to differences in vertical sensitivity, correlations above 100 hPa are generally low or even negative. Moderate correlations (up to 0.4) are found between approximately 700 and 200 hPa, indicating reasonable temporal agreement between the model simulations and satellite observations in the mid-to upper-troposphere. The strongest agreement appears near 500 hPa (Figure 6 and Table S8 in Supporting Information S1); however, this likely reflects the peak sensitivity of TES, AIRS, and CrIS retrieval kernels rather than representing a universal optimum across all instruments. Likewise, the presentation of vertical profiles (Figures 6a–6c) may give the impression of agreement in the stratosphere. Given the limited sensitivity of current satellite instruments above approximately 100 hPa, interpretations at these higher altitudes should be viewed with caution, as they may not fully meet the standards for rigorous evaluation. Nonetheless, it is worth noting that the ensemble mean consistently shows better agreement with satellite observations than individual models, highlighting the potential value of ensemble-based approaches in capturing atmospheric water vapor isotope variability.

In addition to the vertically resolved evaluation, column-integrated comparisons between WisoMIP model outputs and satellite retrievals of precipitable water vapor and its isotopic composition were conducted using GOSAT, GOSAT-2, and TROPOMI (Table S9 in Supporting Information S1). Overall, all models exhibit higher correlation coefficients for H_2O than for δD, indicating that large-scale variability in total column water vapor is more consistently reproduced than the corresponding isotope signal. Nonetheless, the ensemble mean outperforms most individual models for both variables across all three satellite products. Moreover, when directly comparing each model's performance across the two variables, a strong positive relationship emerges: the Pearson correlation between model skill in H_2O and δD reaches 0.95 for GOSAT, 0.93 for GOSAT-2, and 0.91 for TROPOMI. This consistent relationship across satellite products suggests that models which better capture the spatial and temporal variability in total water vapor also tend to better reproduce its isotopic composition. This may reflect the fact that errors in simulating total water vapor often lead to similar errors in its isotopic signal, or that the two variables are physically linked. Although Table S9 in Supporting Information S1 does not explicitly quantify internal model processes, this paired evaluation highlights systematic performance differences and reinforces the value of water isotopes as an additional and informative constraint on hydrological model fidelity.

Among the participating models, we find that NICAM-WISO, a non-hydrostatic model that does not employ cumulus parameterization, shows notably different behavior in both the vertical depletion of water vapor isotope content and model-data temporal correlations across vertical layers. While these differences may partly arise from the lack of cumulus parameterization, they are likely also influenced by deficiencies in the representation of vertical transport and condensation processes. This highlights the importance of accurately representing atmospheric water processes, such as condensation, evaporation, re-evaporation, and convective mixing, all of which play key roles in shaping the isotopic composition of atmospheric moisture. Since these processes ultimately manifest in precipitation isotope signals, the poor agreement of NICAM-WISO with observed precipitation isotopes suggests that water isotopes provide a sensitive and integrative constraint for evaluating the coupling between atmospheric moisture processes and surface water exchange.

4. Results 2: Isotopic Signals of a Changing Climate

4.1. Isotopic Trends Under Global Warming

4.1.1. Climate Variables

One of the key aspects of isotope-enabled modeling for the present-day climate is understanding the processes that govern atmospheric water vapor, including its residence time, surface evaporation, and cloud microphysics such as condensation and re-evaporation. These processes influence both the distribution and variability of water vapor in the atmosphere, which are crucial for interpreting current extreme events and projecting future changes under global warming.

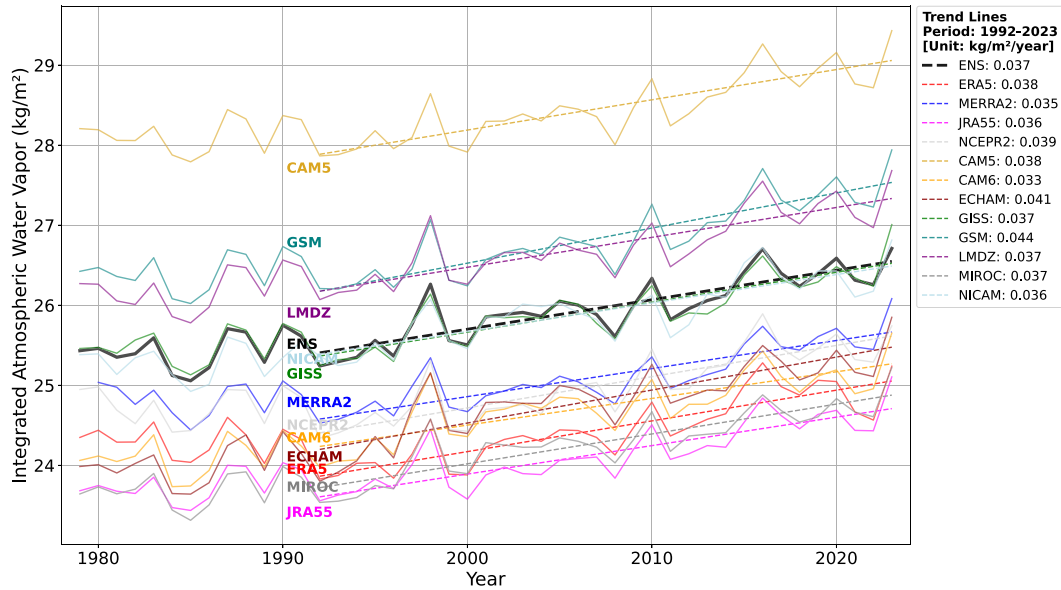

Figure 7. Time series of global mean vertically integrated atmospheric water vapor (precipitable water vapor, PWV; kg m^{-2}) from 1979 to 2023, based on reanalysis data sets (ERA5, MERRA-2, JRA-55, and NCEP-R2) and isotope-enabled AGCMs participating in WisoMIP. Solid lines represent annual mean PWV, and dashed lines indicate linear trends over the recent 32-year period (1992–2023). The thick black line denotes the ensemble mean (ENS).

In this study, we first examined the trend in vertically integrated atmospheric water vapor, confirming that atmospheric moisture has increased in association with rising temperatures (Figure 7). Compared to reanalysis products (ERA5, MERRA-2, JRA-55, and NCEP-R2), the WisoMIP ensemble simulates a generally more humid atmosphere. Over the recent 30-year period (1992–2023), the trends in total column water vapor were 0.038, 0.035, 0.036, and 0.039 kg m^{-2} yr^{-1} for ERA5, MERRA-2, JRA-55, and NCEP-R2, respectively. The ensemble mean of the iso-AGCMs shows a comparable trend of 0.037 kg m^{-2} yr^{-1}, suggesting that the modeled increase in water vapor is consistent with the theoretical expectations from the Clausius–Clapeyron relationship and supported by observational data sets. Although all models were nudged to the same large-scale wind circulation and sea surface conditions from reanalysis, there is substantial spread in the simulated water vapor fields. This discrepancy primarily arises from differences in model physics, as water vapor itself was not nudged. It is worth noting, however, that the WisoMIP ensemble mean exhibits greater atmospheric moisture than any individual reanalysis product. Moreover, reanalysis products themselves show non-negligible differences in precipitable water content. This implies that the choice of reanalysis product used for nudging could introduce additional uncertainty, especially for unconstrained variables such as water vapor. Interannual variability in vertically integrated water vapor also shows strong correspondence with major climate modes such as ENSO. In particular, years with strong El Niño events—such as 1997–1998, 2015–2016, and 2023—are associated with pronounced increases in global atmospheric moisture in the ensemble, consistent with enhanced tropical evaporation and convection during these periods. As trend significance was assessed at each grid point independently, no correction for multiple testing was applied; therefore, it is preferable to focus on coherent large-scale signals rather than isolated local significance.

Over the past 45 years, temperature increases have been most pronounced in the high-latitude regions of the Northern Hemisphere, primarily due to Arctic amplification (Figure 8a). This amplification is driven by sea ice loss, which reduces surface albedo and enhances local warming through greater absorption of solar radiation. Warming over land has been stronger than over oceans, reflecting the lower heat capacity of land and reduced evaporative cooling. In contrast, parts of the Southern Ocean, particularly near the Antarctic Circumpolar Current, have shown muted or even negative temperature trends—likely due to strong vertical mixing and the upwelling of cold deep waters (Armour et al., 2016).

The most prominent increases in precipitable water are found in the tropics (Figure 8d). In contrast, the subtropical dry zones over the Pacific and the midlatitude to subpolar North Atlantic exhibit relatively weak—or even

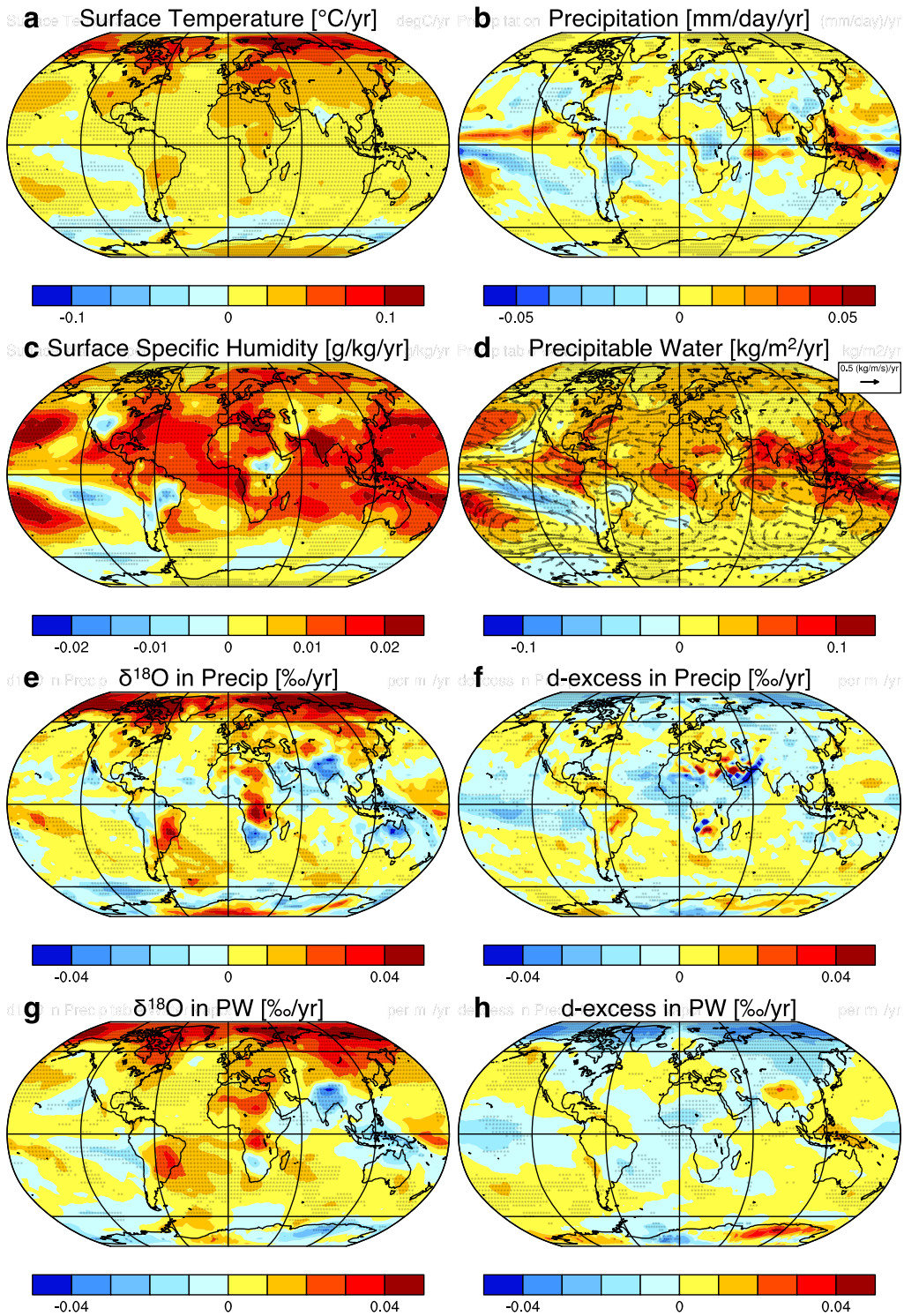

Figure 8. Spatial trends from 1979 to 2023 in key climate and isotopic variables from the WisoMIP ensemble. Panels (a–d) show thermodynamic and hydrological variables: surface temperature (a), precipitation (b), surface specific humidity (c), and vertically integrated precipitable water with overlaid horizontal moisture flux trends (vectors; d). Panels (e–h) show isotopic variables: $\delta^{18}O$ in precipitation (e), d-excess in precipitation (f), $\delta^{18}O$ in precipitable water (g), and d-excess in precipitable water (h). Trends were calculated using the non-parametric Mann–Kendall test, which detects monotonic tendencies in time series without assuming a specific data distribution. Dots on each map indicate regions with statistically significant trends at the 95% confidence level ($p < 0.05$), where the null hypothesis of no trend is rejected.

negative—trends in atmospheric and surface vapor and precipitation. These muted responses are likely related to persistent large-scale subsidence and limited moisture convergence in the subtropics, while reduced poleward ocean heat transport associated with a weakening Atlantic Meridional Overturning Circulation (AMOC) may contribute to the subdued trends in the North Atlantic. Nevertheless, modest increases in both surface vapor and precipitation are observed in mid-to high-latitude regions (Figures 8b and 8c). These increases in atmospheric water vapor can directly influence the isotopic composition of water, especially $\delta^{18}O$, through both thermodynamic mechanisms (such as reduced Rayleigh distillation) and dynamic processes (e.g., changes in moisture source and transport).

4.1.2. Water Isotopes

To explore how this increase in water vapor affects changes in isotopic composition, we examined the spatial trends in $\delta^{18}O$ and d-excess across precipitation, surface vapor, and column vapor fields (Figures 1–3). These trends are further visualized in map form in Figure 8, allowing us to assess the geographic patterns and magnitudes of isotopic responses to warming.

In general, higher atmospheric moisture leads to reduced Rayleigh distillation along moisture transport pathways, as more vapor is retained in the atmosphere before precipitation occurs. This is primarily because the increase in atmospheric water vapor content (ΔQ) exceeds the increase in precipitation (ΔP; i.e., $\Delta Q > \Delta P$), as discussed in Held and Soden (2006), which results in longer vapor residence times and reduced isotopic depletion during transport. As a result, water vapor arriving in continental interiors or high-latitude regions tends to be less isotopically depleted than before, leading to an overall increase in $\delta^{18}O$ in both precipitation and precipitable water (Figures 8e and 8g),consistent with analyses of GNIP data (Putman et al., 2021). This effect is particularly evident over land, where moisture transport plays a dominant role and where there is less local evaporative source to buffer isotopic changes.

At the same time, d-excess, which reflects non-equilibrium fractionation during evaporation and is sensitive to relative humidity and sea surface conditions at the moisture source, shows more complex spatial patterns (Figures 8f and 8h). In some continental regions, including interior areas, d-excess has increased (Cropper et al., 2021; Masiol et al., 2021) alongside $\delta^{18}O$, likely due to enhanced recycling of water vapor and more frequent re-evaporation under warmer and more convective conditions. As surface temperatures rise, more water evaporates from soils, vegetation, and surface waters, and this moisture is rapidly recycled through the lower atmosphere. When raindrops partially re-evaporate while falling through dry air, or when water vapor is sourced from land evaporation under low relative humidity, kinetic fractionation becomes stronger, leading to higher d-excess values.

In contrast, over high-latitude regions in the Northern Hemisphere, where temperature increases have been most pronounced, both near-surface vapor and precipitation show decreasing d-excess, even as $\delta^{18}O$ increases. This opposite behavior indicates a shift from the recycling-dominated continental regime to a source-controlled marine regime, where changes in evaporation conditions rather than temperature alone determine the isotopic response.

There are several plausible explanations for the decline in modeled d-excess. First, warmer temperatures and increased atmospheric moisture are associated with higher evaporation relative humidity, which suppresses kinetic fractionation at the oceanic source. Higher relative humidity over the ocean (Figure S17a in Supporting Information S1) reduces the disequilibrium between the ocean surface and the overlying air, thereby limiting the extent of kinetic fractionation during evaporation (Fiorella et al., 2021; T. Schneider et al., 2010). In more humid environments, the reduced contrast between vapor and liquid phases suppresses isotopic fractionation, introducing vapor with lower d-excess into the atmosphere, especially when surface winds are weak and sea surfaces are relatively warm.

Second, the moisture transported to Arctic regions may increasingly originate from more proximal or recycled sources with shorter transport trajectories. While the increase in local evaporation due to sea ice loss may play a role, its magnitude remains relatively small compared to the dominant meridional transport of moisture (Siler et al., 2025). Nonetheless, reduced sea ice extent and enhanced surface warming expose open ocean areas, potentially facilitating more frequent local evaporation events. These nearer-source vapors may exhibit lower d-excess values, especially when formed under warm and humid conditions that suppress kinetic fractionation and

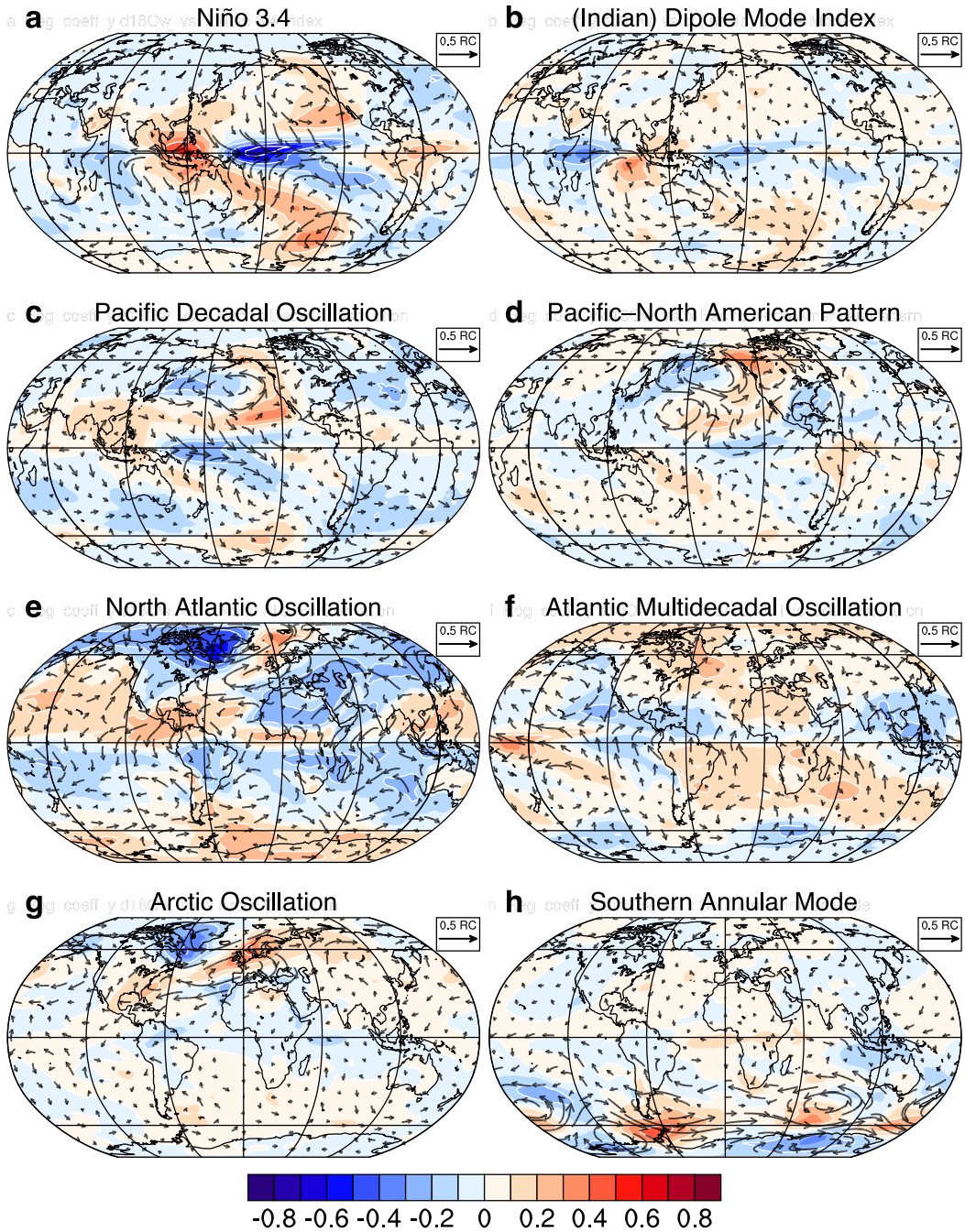

Figure 9. Regression coefficients between normalized climate indices and normalized $\delta^{18}O$ in precipitable water vapor, based on the WisoMIP ensemble. Each panels (a–h) corresponds to one climate mode: (a) Niño 3.4, (b) Dipole Mode Index (DMI), (c) Pacific Decadal Oscillation (PDO), (d) Pacific–North American Pattern (PNA), (e) North Atlantic Oscillation (NAO), (f) Atlantic Multidecadal Oscillation (AMO), (g) Arctic Oscillation (AO), and (h) Southern Annular Mode (SAM). Shading indicates the unitless regression coefficient between standardized climate indices and standardized isotopic values, with red indicating positive and blue negative responses to the index. Arrows show the regression coefficients of vertically integrated horizontal moisture flux (kg m^{-1} s^{-1}), reflecting changes in large-scale moisture transport associated with each mode. The corresponding regression results for d-excess in precipitable water vapor are shown in Figure S18. Additional regression maps for related hydrometeorological and isotopic variables are provided in Figures S19–S31 of Supporting Information S1, offering a broader view of the climate mode influences.

limit Rayleigh distillation. However, exceptions may occur under conditions such as cold-air outbreaks, where d-excess can remain high.

Taken together, these results suggest that d-excess trends reflect two distinct regimes: (a) a recycling-dominated continental regime, where warming enhances re-evaporation and increases d-excess, and (b) a source-controlled high-latitude marine regime, where warming and higher humidity suppress kinetic fractionation and decrease d-excess. While our analysis identifies multiple plausible mechanisms, quantitatively disentangling their relative contributions remains challenging due to overlapping effects of evaporation conditions, transport pathways, and recycling processes, which are not easily separable in current model diagnostics.

Overall, the rise in $\delta^{18}O$ can be seen as a robust thermodynamic signal of warming, whereas the decline in d-excess at high latitudes more likely reflects changes in the characteristics of moisture sources and evaporation conditions rather than temperature alone. In contrast, over the Antarctic continent, $\delta^{18}O$ tends to decrease while d-excess increases, likely reflecting long-range transport from cold, remote oceanic sources and minimal local recycling, which enhance kinetic fractionation at the source.

The modeled isotopic depletion trend over the Maritime Continent may be associated with an enhanced equatorial Pacific sea surface temperature gradient, along with intensified convection and rainout under warming, which leave the remaining vapor more depleted (Figure 8g and Figure S13 in Supporting Information S1). Diagnostics of surface temperature (Figure S14a in Supporting Information S1), vertical motion (Figures S14b–S14j in Supporting Information S1), water vapor (Figure S15 in Supporting Information S1), and zonal wind (Figure S16 in Supporting Information S1) indicate locally intensified ascent and stronger upper-level westerlies over the tropical central Pacific, features that are consistent with a modest strengthening of the Walker circulation. The column-mean $\delta^{18}O$ decrease likely reflects the increasing contribution of isotopically lighter lower-tropospheric vapor (mass-weighted effect) resulting from enhanced condensation and precipitation, while the vertical profile shows a transition from depletion below ∼500 hPa to enrichment aloft, consistent with stronger upward motion. Future work using water-tagging experiments and targeted diagnostics will help clarify the respective roles of convection, circulation, and moisture transport in shaping the isotopic trends.

Interestingly, while the WisoMIP ensemble shows a negative trend in $\delta^{18}O$ over Antarctica, recent ice core syntheses suggest a modest positive trend of approximately $0.11 \pm 0.02‰$ per decade for the 1950–2005 period (Casado et al., 2023). Although the ensemble mean generally improves large-scale isotopic patterns, it still exhibits a negative Antarctic $\delta^{18}O$ trend, indicating that ensemble averaging cannot remove shared structural biases (i.e., errors correlated across models due to similar physics and parameterizations). In addition, the precipitable water trend over Antarctica remains of low statistical confidence, and because all models are nudged to the same reanalysis, differences in the nudged circulation's representation of Antarctic moisture transport (as well as known discrepancies among reanalyzes themselves) may also contribute to the mismatch. Taken together, this discrepancy highlights a potential mismatch not in the isotopic parameterizations themselves, but in the representation of large-scale transport or polar amplification. Previous studies have shown that CMIP5 and CMIP6 models tend to underestimate Antarctic warming, likely due to limited representation of feedbacks and modes of variability such as the Southern Annular Mode.

Isotope-enabled models—even with the same nudged wind fields—can still exhibit differences in long-range moisture transport to Antarctica. This is because nudging constrains the large-scale wind patterns but not the amount or thermodynamic properties of moisture transported along those paths, which depend on model-specific representations of specific humidity, cloud microphysics, and precipitation efficiency. Isotopic fields are particularly sensitive to these differences in source moisture characteristics and rainout history, making them effective tracers for detecting such inter-model discrepancies. Thus, the divergence between modeled and observed $\delta^{18}O$ trends may reflect differences in how models simulate the thermodynamic aspects of transport, even when the dynamic circulation is constrained.

Taken together, these results highlight the importance of not only thermodynamic drivers of isotope variability over the past several decades, but also the role of dynamical processes such as moisture transport and convergence in altering the isotope fields. To better understand the mechanisms shaping regional isotopic patterns, we next examine how large-scale climate phenomena and modes of variability modulate the spatial distribution of $\delta^{18}O$

and d-excess through moisture-flux convergence and divergence, as well as variations in moisture source distance, atmospheric residence time, and source characteristics.

4.2. Isotopic Response to Climate Modes of Variability

With the goal of capturing a coherent isotopic fingerprint of the present-day climate, the WisoMIP ensemble—an integration of expertise from multiple modeling groups—provides a robust modeling framework that achieves the closest agreement with surface and satellite observations to date. Leveraging this capability, we use this ensemble to examine how normalized climate indices—including the El Niño–Southern Oscillation (ENSO; Niño 3.4, NOAA PSL, https://psl.noaa.gov/data/correlation/nina34.data), the Dipole Mode Index (DMI; a common metric of the Indian Ocean Dipole, IOD, NOAA PSL, https://psl.noaa.gov/gcos_wgsp/Timeseries/Data/dmi.had.long.data), the Pacific Decadal Oscillation (PDO; NOAA NCEI, https://www.ncei.noaa.gov/access/monitoring/pdo/), the Pacific–North American Pattern (PNA; NOAA NCEI, https://www.ncei.noaa.gov/access/monitoring/pna/), the North Atlantic Oscillation (NAO; NOAA NCEI, https://www.ncei.noaa.gov/access/monitoring/nao/), the Atlantic Multidecadal Oscillation (AMO; NCAR Climate Data Guide, https://climatedataguide.ucar.edu/sites/default/files/2022-03/amo_monthly.txt), the Arctic Oscillation (AO; NOAA NCEI, https://www.ncei.noaa.gov/access/monitoring/ao/), and the Southern Annular Mode (SAM; British Antarctic Survey, https://legacy.bas.ac.uk/met/gjma/sam.html)—influence the normalized isotopic signals of precipitable water, specifically δ^{18}O and d-excess (Figure 9 and Figure S16 in Supporting Information S1, respectively). Based on regression coefficients, we analyze the spatial patterns of isotopic depletion or enrichment associated with each climate phenomenon. This analysis provides insights into finer-scale spatiotemporal weather variability and supports interpretations of past climate changes from paleoclimate records. In addition to isotopic fields, regression maps for surface temperature, pressure, precipitation, evaporation, surface specific humidity, precipitable water vapor, and precipitation efficiency are included in Figures S19–S25 of Supporting Information S1. Furthermore, isotopic responses in δ^{18}O and d-excess in precipitation, surface specific humidity, and evaporation are shown in Figures S26–S31 of Supporting Information S1, offering a more complete view of the hydrological and isotopic sensitivity to each climate mode.

Moisture-flux convergence forces strong ascent and heavy-isotope rainout, leaving the column vapor depleted in δ^{18}O. For instance, during El Niño, enhanced convergence into the eastern Pacific produces the largest δ^{18}O minima (blue in Figure 9a); positive NAO/AO phases intensify the westerlies, drive convergence over the subpolar Atlantic, and yield the deepest δ^{18}O signal in the Iceland–North Sea region (Figures 9e and 9g); and a positive SAM shifts storm tracks poleward, focuses the convergence circulation system over Antarctica, and causes localized δ^{18}O depletion along the coastal margin. This SAM-related isotope pattern aligns with the findings of (Kino et al., 2021), which identify strong δ^{18}O–SAM correlations over the Antarctic interior.

In contrast, moisture-flux divergence and anticyclonic outflow suppress ascent and local rainout, allowing the vapor column to retain or import heavier isotopes and thus become enriched in δ^{18}O. For example, positive PDO and PNA phases establish a subtropical anticyclone over the North Pacific that exports moisture toward western North America, producing pronounced δ^{18}O maxima (red in Figures 9c and 9d); a positive IOD induces divergence over the eastern Indian Ocean, where Walker-type subsidence leads to clear enrichment (Figure 9b); and under a positive SAM, the divergent branch of the poleward-shifted westerly belt exports moisture from the southern midlatitudes, yielding enriched δ^{18}O across the South Atlantic, South Indian Ocean, and parts of the South Pacific basins (Figure 9h).

Consistent with the mechanisms described above, d-excess in atmospheric vapor—governed primarily by kinetic fractionation at the moisture source—often exhibits spatial patterns that differ from those of δ^{18}O. In convergence-driven regions, strong rainout generally leads to depletion in both δD and δ^{18}O, but the extent to which d-excess decreases depends on source vapor characteristics and subsequent atmospheric processes. For example, in the Niño 3.4 core, elevated d-excess values emerge despite strong convergence, likely due to the overriding influence of evaporation under warm and dry conditions that enhance kinetic fractionation. Unlike δ^{18}O, which primarily reflects local rainout and Rayleigh distillation, d-excess anomalies often extend more broadly, as they retain information about source conditions and cumulative transport history. However, interpreting d-excess requires caution, as it is highly sensitive to droplet exchange, microphysical processes, and both vertical and

horizontal mixing pathways—factors that contribute to significant spatial variability and inter-model disagreement.

5. Discussion and Conclusions

This paper presents first results from WisoMIP, the third undertaking of the Stable Water Isotope Intercomparison Group, and describes the experimental design of the coordinated experiment in which eight isotope-enabled atmospheric general circulation models were nudged to ERA5 reanalysis winds and forced with ERA5 sea-surface conditions for 1979–2023. We find that ensemble-averages across models reduce residual biases exhibited by individual simulations. Furthermore, by prescribing the same large-scale circulation, we can isolate the influence of physical and microphysical parameterizations on simulated water-isotope behavior. We discuss here the models evaluation, the isotope responses to global warming and internal climate variability, and the perspectives enabled by the WisoMIP data set.

5.1. Model Evaluation Against Observations

The results reveal that the ensemble mean reproduces the meridional and vertical gradients of δ^{18}O and d-excess with substantially smaller biases than any individual model. In particular, all models capture the expected simple Rayleigh distillation model which predicts that heavy isotopes condense first, and remain preferentially in liquid form. Thus, in the atmosphere, δ^{18}O of surface vapor is depleted compared to surface water; precipitation is relatively enriched compared to surface vapor, while total column precipitable water is more depleted than surface vapor. This structure of relative enrichment or depletion in various water reservoirs reflects the cumulative effects of isotopic fractionation throughout the atmospheric column: column water vapor primarily integrates the distillation history of transported moisture; precipitation is relatively enriched compared to the remaining vapor due to equilibrium fractionation during condensation, where the fractionation factor (α) is relatively large; however, the degree of enrichment ultimately depends on the extent of rainout and the evolving isotopic composition of the column water vapor; and surface vapor is influenced by near-surface processes such as sublimation, re-evaporation, and turbulent mixing within the atmospheric boundary layer.

Validation against GNIP precipitation records, Antarctic snow isotope measurements, and multiple satellite retrievals demonstrates that the ensemble mean effectively captures both temporal and spatial variability in δ^{18}O in precipitation. Correlation coefficients reach as high as 0.66 for monthly time series at GNIP stations. Over Antarctica, site-level comparisons between modeled and observed annual-mean isotopic composition—derived from long-term monthly observations—yield correlation coefficients up to 0.95 (Table S7 in Supporting Information S1), confirming strong agreement in spatial patterns across individual sites. For free-tropospheric δD near 500 hPa, the correlations range from 0.54 (TES) to 0.71 (IASI), with intermediate values of 0.62 (AIRS) and 0.60 (CrIS). These metrics confirm that the ensemble mean reproduces the observed variability across space and time, and across multiple validation products spanning water vapor and precipitation.

The higher-order (and certainly more stringent) water isotope metric, d-excess, remains one of the more challenging tracers to simulate accurately, partly due to uncertainties in the representation of kinetic fractionation and cloud microphysics. In particular, differences in how models treat ice-supersaturation (often parameterized as $S = 1 - \lambda \times (T - 273.15\ \mathrm{K})$, with λ ranging from about 0.002 to 0.0045 K^{-1}) can lead to varying kinetic effects under cold, supersaturated conditions. These choices mainly affect d-excess and^{17}O-excess whereas large-scale δ^{18}O patterns are less affected. For example, simulated surface vapor δ^{18}O values in East Antarctica (e.g., −55‰) differ substantially from observations at Dome C and Kohnen Station, on opposite sides of the East Antarctic Ice Sheet, suggesting potential deficiencies in the simulation of sublimation-driven vapor (Hu, Yan, et al., 2022) and boundary-layer exchange, such as post-depositional changes by airborne snow (Wahl et al., 2024). Importantly, fractionation associated with sublimation can vary depending on the physical process; for instance, the sublimation of entire ice grains is considered non-fractionating. Satellite data has helped to constrain these processes in the tropics and mid-latitudes allowing improvement in isotope enabled models (Field et al., 2014). In contrast, relatively few observations exist for sublimation in polar regions, and this requires in situ observations (Madsen et al., 2019; Ritter et al., 2016). In these polar areas, isotopic sensitivities to moisture source and transport history are particularly high, underscoring the need for additional observations to improve model fidelity and interpretation.

Taken together, the ensemble mean reduces individual-model biases, yet residual discrepancies remain, most notably in d-excess amplitude and polar surface-vapor isotopic composition, indicating process-level differences that are not eliminated by the common dynamical forcing. We therefore consider the structural factors that plausibly generate the inter-model spread.

5.2. Sources of Inter-Model Differences

Despite the common ERA5-based forcing, notable differences persist among the WisoMIP models due to variations in their internal physical parameterizations and microphysical treatments of water isotopologues. A primary source of spread arises from how each model represents cloud microphysics and phase transitions, including condensation, evaporation, and re-evaporation, which set equilibrium and kinetic fractionation and thereby shape simulated $\delta^{18}O$ and d-excess fields. Additional spread originates from convective and boundary-layer schemes that regulate vertical mixing, entrainment/detrainment, and near-surface exchange, modulating isotopic gradients between surface vapor and precipitation. Land–atmosphere coupling further contributes through model-specific treatments of soil moisture, vegetation, and evaporation regimes, including how near-surface humidity and evaporation conditions are represented, which in turn alter the isotopic composition of recycled moisture. Finally, modest differences in nudging strength and in the vertical application of reanalysis winds affect regional moisture convergence, transport pathways, and rainout efficiency. Collectively, these structural and numerical distinctions explain much of the remaining diversity in isotopic responses across models.

5.3. Isotope Responses to Global Warming and Climate Modes

Under contemporary warming, the WisoMIP ensemble exhibits a coherent moistening trend of 0.037 kg m^{-2} yr^{-1}, consistent with reanalysis estimates and Clausius–Clapeyron scaling. However, the accompanying isotopic responses are spatially heterogeneous. Across much of the tropics and mid-latitudes, $\delta^{18}O$ becomes heavier as warmer, more humid air weakens Rayleigh distillation. The largest enrichments occur over the Arctic Ocean and mid-to high-latitude continents, areas with the largest temperature trends, where abundant moisture limits isotopic depletion during transport. By contrast, $\delta^{18}O$ becomes lighter in deep convection zones—such as the Maritime Continent and Indian monsoon region—and over Antarctica, where long-range, rainout-depleted vapor dominates. In the tropics, this isotopic depletion is consistent with a strengthened Walker Circulation, which enhances deep convection and rainout in the western Pacific and Maritime Continent. The latter diverges from recent in situ trends, highlighting uncertainties in simulating polar isotope responses. In depletion regimes, intense rainout or prolonged distillation preferentially removes heavy isotopes, leaving vapor and precipitation isotopically lighter. Confidence in d-excess trends remains limited due to sparse observations.

5.4. Implications of Modeled Isotopic Responses to Climate Drivers

D-excess is highly sensitive to near-surface conditions such as relative humidity, wind speed, and evaporation regime due to its dependence on kinetic fractionation at the moisture source. In addition to these physical sensitivities, d-excess also accumulates numerical and process-level uncertainties inherited from both $\delta^{2}H$ and $\delta^{18}O$. As a result, even small modeling errors in $\delta^{18}O$ can propagate nonlinearly and lead to amplified biases in d-excess. This contributes to the weak correlation between modeled d-excess and available observations (Pearson's $r \approx 0.2$), as well as large spatial variability in standardized anomalies. To improve interpretability, future modeling efforts must refine the treatment of secondary processes such as boundary-layer exchange, moisture recycling, and source-region dynamics, and enhance numerical consistency in isotopic tracers.

Regression analyses against eight major climate indices reveal that isotopic responses in the WisoMIP ensemble align closely with large-scale convergence–divergence patterns in the atmosphere. For instance, convergence associated with positive ENSO, NAO, and SAM phases produces strong $\delta^{18}O$ depletion due to enhanced rainout, whereas divergence during positive PDO, PNA, or IOD phases leads to $\delta^{18}O$ enrichment by suppressing local precipitation and favoring long-range moisture transport. These patterns demonstrate that isotopic variability is dynamically consistent with known circulation regimes. Meanwhile, d-excess, controlled by kinetic fractionation at the moisture source, often exhibits opposing signals to $\delta^{18}O$ and tends to be more spatially widespread due to its sensitivity to source conditions and transport history. While these reproducible isotopic fingerprints provide a powerful framework for linking modern atmospheric circulation to paleoclimate proxies, interpreting d-excess

remains challenging due to its dependence on complex and incompletely resolved processes such as droplet exchange, mixing, and microphysics.

These physically grounded responses to recent climate variability provide a critical stepping stone toward broader applications. In particular, further investigation of water-isotope trends under both anthropogenic warming and internal climate modes will deepen our understanding of natural variability and strengthen paleoclimate interpretations. For example, during El Niño events, enhanced convection and moisture convergence over the eastern tropical Pacific lead to pronounced $\delta^{18}O$ depletion due to increased rainout. Such isotope–ENSO relationships not only inform modern diagnostics, but also provide a reference for interpreting past hydroclimatic conditions in tropical ice cores or speleothem records. By elucidating the isotopic expressions of large-scale modes that modulate meteorological events, WisoMIP facilitates improved mechanistic insight into the background states that shape modern hydrological extremes. Additionally, quantifying the inter-model spread in these responses offers a path to constrain uncertainty and evaluate the robustness of isotopic signals under varying physical parameterizations. Collectively, these capabilities highlight WisoMIP as not only the most comprehensive present-day isotope data set to date, but also a credible tool for testing hypotheses and guiding interpretations in both modern and paleo-hydroclimate research.

5.5. Outlook and Future Directions

The WisoMIP data set includes a broad set of isotope-related and atmospheric variables (Table S1 in Supporting Information S1), which provide information for not only water isotope research but also model process evaluation through reanalysis-nudged simulations. These standardized variables support diagnostics of moisture transport, kinetic effects, and cloud-related processes under unified experimental conditions. They also serve as a foundation for assessing model skill and guiding future isotope-enabled modeling efforts. We offer the following conclusions for our study, the first phase of WisoMIP:

1. Under the common ERA5 reanalysis forcing, isotope-enabled models in WisoMIP produce broadly consistent large-scale patterns. Nevertheless, inter-model differences persist and are most evident over high- and mid-latitude continents and in the tropics. Over the oceans, prescribed sea-surface conditions tightly constrain temperature, whereas over land, larger temperature biases emerge owing to diversity in land–surface schemes such as soil moisture, vegetation, and inland water bodies. Water-vapor fields exhibit greater spread in the tropics due to differences in convective parameterizations. In addition, differing microphysical treatments of water isotopologues, including equilibrium and kinetic fractionation and ice supersaturation, are the primary drivers of inter-model spread in challenging metrics such as d-excess and polar isotopes, with additional contributions from nudging strength and the vertical application of reanalysis winds.
2. The ensemble mean provides the closest agreement with observational data sets, including the precipitation isotope records from global monitoring networks, snow measurements in Antarctica, and satellite-based retrievals. This demonstrates the effectiveness of multi-model averaging in reducing individual model biases and improving overall fidelity.
3. Simulated trends in atmospheric isotopes under recent warming conditions reflect shifts in moisture transport, convergence patterns, and large-scale circulation variability. These modeled responses offer a physically interpretable basis for using stable isotopes to investigate regional changes in the hydrological cycle.

This study—remarkably—demonstrates that a carefully designed, reanalysis-nudged isotope-model ensemble can outperform its own driving fields. Moreover, the ensemble of nudged water isotope-enabled simulations provides a publicly available community benchmark for process-oriented analyses, and serves as a springboard for next-generation isotope-enabled modeling efforts. By standardizing inputs and experimental design, WisoMIP enables rigorous inter-model comparisons, targeted evaluations of parameterization sensitivities, and clearer detection of circulation-driven climate signals. The resulting ensemble offers the most comprehensive present-day assessment of isotope-enabled AGCMs to date, deepening our understanding of model strengths and limitations while highlighting persistent challenges in simulating kinetic fractionation, cloud microphysics, and moisture transport.

Future WisoMIP efforts and phases will build on this foundation by testing the impacts of increasing spatial resolution (including convection-permitting and cloud-resolving models), investigating seasonal isotope processes and their inter-model variability, incorporating oceanic isotope cycling and extreme-event analyses, and

high carbon dioxide forcing experiments. Indeed, beyond modern climate evaluation, the WisoMIP data set holds strong potential for a wide range of applications, including paleoclimate simulations enabling direct isotope-model intercomparisons, development and training of artificial-intelligence frameworks for climate diagnostics, and improved interpretation of future water-isotope projections by isolating the role of model physics in shaping isotopic responses. Several of these extensions are already being planned as follow-up studies within the Water Isotope Model Intercomparison Project. We will continue to advance isotope-enabled modeling and hydroclimate interpretation as a means for improving hydroclimate projections on our warming planet.

This interdisciplinary water isotope modeling work links atmospheric, remote-sensing, modeling, and paleoclimate specialists in the climate science community at-large to improve our understanding of hydrologic extremes. Water isotope science opens the door to a large body of extended scientific broader impacts. For example, WisoMIP models form the basis for water-isotope data assimilation reconstructions for modern and paleoclimate periods (Tada et al., 2021); the WisoMIP suite of isotope-enabled model simulations serve as model priors to assimilate water isotope data *in the same units*, avoiding assumptions inherent to linear regression methods in data assimilation. In doing so, we may improve reanalysis products, critical for our understanding of current rates and spatial patterns of climate change.

In closing, as Earth warms over the next century, the hydrological cycle is projected to accelerate, with increases in both wet and dry extremes (Prudhomme et al., 2014; Stevenson et al., 2022; Trenberth, 1999, 2011). These present and future changes to the hydrological cycle impact our global society in myriad ways, from prolonged drought to flood hazard. Moreover, the hydrological cycle plays an enormous role in the climate system's response to anthropogenic forcing: water vapor, precipitation, ocean- and land-atmosphere fluxes and cloud feedbacks control radiative feedbacks via the greenhouse effect and shortwave forcing, and may either mitigate or exacerbate Earth's temperature response. Large regime changes in the hydrological cycle could manifest as non-linear, abrupt reorganizations in response to steady greenhouse gas forcing. Finally, modes of natural climate variability also face an uncertain future, and may be altered leading to cascading impacts on regional hydroclimate. To plan for a future in an altered water cycle, the full range of the hydrological cycle's variability and its response to external forcing must be *constrained in time and space* and *modeled accurately*. This will only be possible with a new array of approaches that harness and connect disparate data sources spanning multiple timescales. WisoMIP seeks to generate new mechanistic understanding of how and why the hydrological cycle and regional patterns of atmospheric circulation will respond to greenhouse gas forcing using *stable water isotopes*. We hope this first contribution will be the first of many elucidating our planet's rapidly changing water cycle through a water isotopic lens.

Conflict of Interest

The authors declare no conflicts of interest relevant to this study.

Data Availability Statement

All model outputs from the WisoMIP project are publicly available at: https://portal.nccs.nasa.gov/datashare/giss-publish/pub/paleoclimate/wisomip/. Observational data sets used for validation include CRU TS v4.06 for near-surface temperature (https://crudata.uea.ac.uk/cru/data/hrg/), GPCP v2.3 for precipitation (https://doi.org/10.7289/V5RX998Z), and GNIP for water isotopes, accessible via the WISER database maintained by the IAEA (https://nucleus.iaea.org/wiser). Daily to annual precipitation isotope data from Concordia Station (East Antarctica) for the period 2008–2017 are also used, available via Zenodo (Dreossi et al., 2024; https://doi.org/10.5281/zenodo.11613330). Satellite-based isotope products are also available from multiple sources. The TES/Aura L2 HDO Lite Nadir V006 (TL2HDOLN_6) data set is available through NASA Earthdata (https://cmr.earthdata.nasa.gov/search/concepts/C1000000361-LARC.html). The AIRS and CrIS deuterated water vapor products from the TROPESS project can be obtained via NASA GES DISC (https://disc.gsfc.nasa.gov/datasets/TRPSYL2H-DOAIRSORS_1/summary for AIRS; https://disc.gsfc.nasa.gov/datasets/TRPSYL2HDOCRSRS_1/summary for CrIS). The MUSICA IASI isotopologue data set (version 2) is available in two forms. The Level-3 regridded product used in this study ($1° \times 1°$ resolution, twice daily) is accessible at https://doi.org/10.35097/495. The full-resolution data set is available at https://doi.org/10.35097/415. The TROPOMI data set is available at https://tropomi.grid.surfsara.nl/hdo/. Core representative analysis and plotting scripts used to process the WisoMIP outputs are openly available at https://github.com/hayoungbong/WisoMIP.git.

Acknowledgments
This project involved the collaboration of a team of international researchers, each contributing through specific roles. Sylvia Dee coordinated the broader collaborative activities and facilitated group discussions and meetings; she gratefully acknowledges the support of this work from National Science Foundation (NSF) Climate and Large-Scale Dynamics CAREER Award No. 2338861. Allegra N. LeGrande served as the primary advisor, guiding the scientific framing and interpretation of the results. National Aeronautics and Space Administration (NASA) High-End Computing Program provides computational resources through the NASA Center for Climate Simulation at Goddard Space Flight Center. We extend our gratitude to NASA Goddard Institute for Space Studies for institutional support, including its hosting of Hayoung Bong's appointment through the NASA Postdoctoral Program (NPP), whose support is likewise acknowledged. Part of this research was carried out at the Jet Propulsion Laboratory, California Institute of Technology, under a contract (80NM0018D0004) with NASA, with funding support from the ROSES Terra/Aqua call 20-TASNPP20-0003, task order 80NM0018F0583. The CESM project is supported primarily by the NSF. This material is based upon work supported by the National Center for Atmospheric Research (NCAR), which is a major facility sponsored by the NSF under Cooperative Agreement No. 1852977. Jiang Zhu acknowledge support from the NSF Grant 2513025 and 2530608. Rich Fiorella acknowledges support from NSF Award 2309269 and a U.S. Department of Energy Early Career Research Award through the Office of Science Office of Biological and Environmental Research. The IsoGSM3 simulations were supported by JSPS KAKENHI (JP21H05002, JP22H04938), the MEXT SENTAN Program (JPMXD0722680395), the ERCA S-20 Project (JPMEERF21S12020), the Arctic Challenge for Sustainability III (ArCS III) Project (JPMXD1720251001), and the Japan Science and Technology Agency (JST; JPMJSC22E4 and JPMJMI24I1). The LMDZ6 simulations, overseen with scientific guidance from Cécile Agosta, were performed with computing HPC and storage resources by GENCI at IDRIS thanks to the grant 2025-AD010114000R2 on the supercomputer Jean Zay's CSL partition. Model outputs were contributed by Qinghua Ding (iCAM5) with assistance from Jiang Zhu, Rich Fiorella (iCAM6), Alexandre Cauquoin (ECHAM6-wiso), Niels Dutrievoz (LMDZ6), Masahiro Tanoue (NICAM-WISO), and Hayoung Bong (IsoGSM3, GISS-E2.1, MIROC5-iso). Satellite data were prepared by Michelle Frazer, Mampi Sarkar, John Worden, Stephen Good, Adriana Bailey, Matthias Schneider,

References

Adler, R., Wang, J.-J., Sapiano, M., Huffman, G., Bolvin, D., Nelkin, E., & Program, N. C. (2017). Global precipitation climatology project (GPCP) climate data record (CDR), version 1.3 (daily) [Dataset]. *NOAA National Centers for Environmental Information*. https://doi.org/10.7289/V5RX998Z

Angert, A., Lee, J.-E., & Yakir, D. (2008). Seasonal variations in the isotopic composition of near-surface water vapour in the eastern Mediterranean [Dataset]. *Tellus B: Chemical and Physical Meteorology*, *60*(4), 674–684. https://doi.org/10.1111/j.1600-0889.2008.00357.x

Armour, K. C., Marshall, J., Scott, J. R., Donohoe, A., & Newsom, E. R. (2016). Southern ocean warming delayed by circumpolar upwelling and equatorward transport. *Nature Geoscience*, *9*(7), 549–554. https://doi.org/10.1038/ngeo2731

Ayache, M., Dutay, J.-C., Mouchet, A., Tachikawa, K., Risi, C., & Ramstein, G. (2024). Modelling the water isotopes distribution in the Mediterranean Sea using a high-resolution oceanic model (NEMO-MED12-watiso-v1. 0): Evaluation of model results against in-situ observations. *Geoscientific Model Development Discussions*, *2024*, 1–33. https://doi.org/10.5194/gmd-17-6627-2024

Bagheri Dastgerdi, S., Behrens, M., Bonne, J.-L., Hörhold, M., Lohmann, G., Schlosser, E., & Werner, M. (2021). Continuous monitoring of surface water vapour isotopic compositions at Neumayer Station III, East Antarctica [Dataset]. *The Cryosphere*, *15*(10), 4745–4767. https://doi.org/10.5194/tc-15-4745-2021

Bailey, A., Blossey, P., Noone, D., Nusbaumer, J., & Wood, R. (2017). Detecting shifts in tropical moisture imbalances with satellite-derived isotope ratios in water vapor [Dataset]. *Journal of Geophysical Research: Atmospheres*, *122*(11), 5763–5779. https://doi.org/10.1002/2016JD026222

Bailey, A., Noone, D., Berkelhammer, M., Steen-Larsen, H., & Sato, P. (2015). The stability and calibration of water vapor isotope ratio measurements during long-term deployments [Dataset]. *Atmospheric Measurement Techniques*, *8*(10), 4521–4538. https://doi.org/10.5194/amt-8-4521-2015

Bailey, A., Noone, D., Dee, S. G., Nusbaumer, J., Conroy, J. L., Stevenson, S., & Atwood, A. (2025). Toward a process-oriented understanding of water in the climate system: Recent insights from stable isotopes. *Environmental Research: Climate*, *4*(1), 012002. https://doi.org/10.1088/2752-5295/ada17b

Bastrikov, V., Steen-Larsen, H., Masson-Delmotte, V., Gribanov, K., Cattani, O., Jouzel, J., & Zakharov, V. (2014). Continuous measurements of atmospheric water vapour isotopes in western Siberia (Kourovka) [Dataset]. *Atmospheric Measurement Techniques*, *7*(6), 1763–1776. https://doi.org/10.5194/amt-7-1763-2014

Berkelhammer, M., Noone, D., Wong, T., Burns, S., Knowles, J., Kaushik, A., et al. (2016). Convergent approaches to determine an ecosystem's transpiration fraction [Dataset]. *Global Biogeochemical Cycles*, *30*(6), 933–951. https://doi.org/10.1002/2016GB005392

Blossey, P. N., Kuang, Z., & Romps, D. M. (2010). Isotopic composition of water in the tropical tropopause layer in cloud-resolving simulations of an idealized tropical circulation. *Journal of Geophysical Research*, *115*(D24). https://doi.org/10.1029/2010JD014554

Bogenschutz, P., Gettelman, A., Morrison, H., Larson, V., Schanen, D., Meyer, N., & Craig, C. (2012). Unified parameterization of the planetary boundary layer and shallow convection with a higher-order turbulence closure in the community atmosphere model: Single-column experiments. *Geoscientific Model Development*, *5*(6), 1407–1423. https://doi.org/10.5194/gmd-5-1407-2012

Bolot, M., Legras, B., & Moyer, E. (2013). Modelling and interpreting the isotopic composition of water vapour in convective updrafts. *Atmospheric Chemistry and Physics*, *13*(16), 7903–7935. https://doi.org/10.5194/acp-13-7903-2013

Bong, H., Cauquoin, A., Okazaki, A., Chang, E.-C., Werner, M., Wei, Z., et al. (2024). Process-based intercomparison of water isotope-enabled models and reanalysis nudging effects. *Journal of Geophysical Research: Atmospheres*, *129*(1), e2023JD038719. https://doi.org/10.1029/2023JD038719

Bonne, J.-L., Masson-Delmotte, V., Cattani, O., Delmotte, M., Risi, C., Sodemann, H., & Steen-Larsen, H. C. (2014). The isotopic composition of water vapour and precipitation in Ivittuut, southern Greenland [Dataset]. *Atmospheric Chemistry and Physics*, *14*(9), 4419–4439. https://doi.org/10.5194/acp-14-4419-2014

Bonne, J.-L., Meyer, H., Behrens, M., Boike, J., Kipfstuhl, S., Rabe, B., et al. (2020). Moisture origin as a driver of temporal variabilities of the water vapour isotopic composition in the Lena River Delta, Siberia [Dataset]. *Atmospheric Chemistry and Physics*, *20*(17), 10493–10511. https://doi.org/10.5194/acp-20-10493-2020

Bony, S., Risi, C., & Vimeux, F. (2008). Influence of convective processes on the isotopic composition ($\delta^{18}O$ and δD) of precipitation and water vapor in the tropics: 1. Radiative-convective equilibrium and tropical ocean–global atmosphere–coupled ocean-atmosphere response experiment (toga-coare) simulations. *Journal of Geophysical Research*, *113*(D19). https://doi.org/10.1029/2008JD009942

Boucher, O., Servonnat, J., Albright, A. L., Aumont, O., Balkanski, Y., Bastrikov, V., et al. (2020). Presentation and evaluation of the IPSL-CM6A-LR climate model. *Journal of Advances in Modeling Earth Systems*, *12*(7), e2019MS002010. https://doi.org/10.1029/2019MS002010

Bowen, G. J., Cai, Z., Fiorella, R. P., & Putman, A. L. (2019). Isotopes in the water cycle: Regional-to global-scale patterns and applications. *Annual Review of Earth and Planetary Sciences*, *47*(1), 453–479. https://doi.org/10.1146/annurev-earth-053018-060220

Bowman, K. W. (2023a). TROPESS airs-aqua L2 deuterated water vapor for reanalysis stream, summary product v1 [Dataset]. *Goddard Earth Sciences Data and Information Services Center (GES DISC)*. https://doi.org/10.5067/55XVECXA26EK

Bowman, K. W. (2023b). TROPESS CrIS-SNPP L2 deuterated water vapor for reanalysis stream, summary product V1 [Dataset]. *Goddard Earth Sciences Data and Information Services Center (GES DISC)*. https://doi.org/10.5067/5SOLOJ3T692X

Brady, E., Stevenson, S., Bailey, D., Liu, Z., Noone, D., Nusbaumer, J., et al. (2019). The connected isotopic water cycle in the Community Earth System Model Version 1. *Journal of Advances in Modeling Earth Systems*, *11*(8), 2547–2566. https://doi.org/10.1029/2019MS001663

Casado, M., Hébert, R., Faranda, D., & Landais, A. (2023). The quandary of detecting the signature of climate change in Antarctica. *Nature Climate Change*, *13*(10), 1082–1088. https://doi.org/10.1038/s41558-023-01791-5

Casado, M., Landais, A., Masson-Delmotte, V., Genthon, C., Kerstel, E., Kassi, S., et al. (2016). Continuous measurements of isotopic composition of water vapour on the East Antarctic Plateau. *Atmospheric Chemistry and Physics*, *16*(13), 8521–8538. https://doi.org/10.5194/acp-16-8521-2016

Cauquoin, A., Risi, C., & Vignon, E. (2019). Importance of the advection scheme for the simulation of water isotopes over Antarctica by atmospheric general circulation models: A case study for present-day and last glacial maximum with LMDZ-iso. *Earth and Planetary Science Letters*, *524*, 115731. https://doi.org/10.1016/j.epsl.2019.115731

Cauquoin, A., & Werner, M. (2021). High-resolution nudged isotope modeling with ECHAM6-wiso: Impacts of updated model physics and ERA5 reanalysis data. *Journal of Advances in Modeling Earth Systems*, *13*(11), e2021MS002532. https://doi.org/10.1029/2021MS002532

Cauquoin, A., Werner, M., & Lohmann, G. (2019). Water isotopes–climate relationships for the mid-Holocene and preindustrial period simulated with an isotope-enabled version of MPI-ESM. *Climate of the Past*, *15*(6), 1913–1937. https://doi.org/10.1029/2021MS002532

Chang, E.-C., & Yoshimura, K. (2015). A semi-lagrangian advection scheme for radioactive tracers in the NCEP regional spectral model (RSM). *Geoscientific Model Development*, *8*(10), 3247–3255. https://doi.org/10.5194/gmd-8-3247-2015

Stefan Noël, Soumyajit Mandal, and Kevin Bowman, support for the collection and use of surface vapor isotope data was facilitated by Hans Christian Steen-Larsen, and guidance on Antarctic analysis was provided by Mathieu Casado and Sonja Wahl. The study design and interpretation further benefited from the expertise of co-advisors Cécile Agosta, Kei Yoshimura, Martin Werner, Atsushi Okazaki, Camille Risi, and Gavin A. Schmidt, who not only provided scientific guidance but also played key roles in the development of the models. Jesse Nusbaumer and Yifan Li contributed in supporting capacity in discussion. We also thank David Noone for providing access to the SWING1 data sets and for sharing background information on the early development of this water-isotope-enabled model intercomparison project. The authors thank the editor, Dr. Yafang Cheng, and the anonymous reviewers for their insightful comments and constructive suggestions, which improved the quality of this study.

Chen, M., Gao, J., Luo, L., Zhao, A., Niu, X., Yu, W., et al. (2024). Temporal variations of stable isotopic compositions in atmospheric water vapor on the southeastern Tibetan plateau and their controlling factors [Dataset]. *Atmospheric Research*, *303*, 107328. https://doi.org/10.1016/j.atmosres.2024.107328

Christner, E., Kohler, M., & Schneider, M. (2017). The influence of snow sublimation and meltwater evaporation on δD of water vapor in the atmospheric boundary layer of central Europe [Dataset]. *Atmospheric Chemistry and Physics*, *17*(2), 1207–1225. https://doi.org/10.5194/acp-17-1207-2017

Craig, H. (1961). Standard for reporting concentrations of deuterium and oxygen-18 in natural waters. *Science*, *133*(3467), 1833–1834. https://doi.org/10.1126/science.133.3467.1833

Cropper, S., Solander, K., Newman, B. D., Tuinenburg, O. A., Staal, A., Theeuwen, J. J., & Xu, C. (2021). Comparing deuterium excess to large-scale precipitation recycling models in the tropics. *npj Climate and Atmospheric Science*, *4*(1), 60. https://doi.org/10.1038/s41612-021-00217-3

Dai, D., Gao, J., Steen-Larsen, H. C., Yao, T., Ma, Y., Zhu, M., & Li, S. (2021). Continuous monitoring of the isotopic composition of surface water vapor at Lhasa, Southern Tibetan Plateau [Dataset]. *Atmospheric Research*, *264*, 105827. https://doi.org/10.1016/j.atmosres.2021.105827

Dansgaard, W. (1964). Stable isotopes in precipitation. *Tellus*, *16*(4), 436–468. https://doi.org/10.1111/j.2153-3490.1964.tb00181.x

Dee, S., Bailey, A., Conroy, J. L., Atwood, A., Stevenson, S., Nusbaumer, J., & Noone, D. (2023). Water isotopes, climate variability, and the hydrological cycle: Recent advances and new frontiers. *Environmental Research: Climate*, *2*(2), 022002. https://doi.org/10.1088/2752-5295/accbe1

Dee, S., Noone, D., Buenning, N., Emile-Geay, J., & Zhou, Y. (2015). SPEEDY-IER: A fast atmospheric GCM with water isotope physics. *Journal of Geophysical Research: Atmospheres*, *120*(1), 73–91. https://doi.org/10.1002/2014JD022194

Diekmann, C. J., Schneider, M., & Ertl, B. (2021). Regular 1°×1° re-gridded MUSICA IASI water isotopologue pair dataset (a posteriori processing version 2) [Dataset]. *Institute of Meteorology and Climate Research, Atmospheric Trace Gases and Remote Sensing (IMK-ASF). Karlsruhe Institute of Technology (KIT)*. https://doi.org/10.35097/495

Dietrich, L. J., Steen-Larsen, H. C., Wahl, S., Jones, T. R., Town, M. S., & Werner, M. (2023). Snow-atmosphere humidity exchange at the ice sheet surface alters annual mean climate signals in ice core records. *Geophysical Research Letters*, *50*(20), e2023GL104249. https://doi.org/10.1029/2023GL104249

Dreossi, G., Masiol, M., Stenni, B., & Zannoni, D. (2024). Daily, monthly and annual data from a decade (2008–2017) of water stable-isotope composition of precipitation at Concordia station, east Antarctica [Dataset]. *Zenodo*. https://doi.org/10.5281/zenodo.11613330

Dutrievoz, N., Agosta, C., Risi, C., Vignon, É., Nguyen, S., Landais, A., et al. (2025). Antarctic water stable isotopes in the global atmospheric model LMDZ6: From climatology to boundary layer processes. *Journal of Geophysical Research: Atmospheres*, *130*(5), e2024JD042073. https://doi.org/10.1029/2024JD042073

Dütsch, M., Blossey, P. N., Steig, E. J., & Nusbaumer, J. M. (2019). Nonequilibrium fractionation during ice cloud formation in iCAM5: Evaluating the common parameterization of supersaturation as a linear function of temperature. *Journal of Advances in Modeling Earth Systems*, *11*(11), 3777–3793. https://doi.org/10.1029/2019MS001764

Ehleringer, J., & Dawson, T. (1992). Water uptake by plants: Perspectives from stable isotope composition. *Plant, Cell and Environment*, *15*(9), 1073–1082. https://doi.org/10.1111/j.1365-3040.1992.tb01657.x

Elsaesser, G. S., Del Genio, A. D., Jiang, J. H., & van Lier-Walqui, M. (2017). An improved convective ice parameterization for the NASA GISS global climate model and impacts on cloud ice simulation. *Journal of Climate*, *30*(1), 317–336. https://doi.org/10.1175/JCLI-D-16-0346.1

Elsaesser, G. S., van Lier-Walqui, M., Yang, Q., Kelley, M., Ackerman, A. S., Fridlind, A. M., et al. (2025). Using machine learning to generate a GISS ModelE calibrated physics ensemble (CPE). *Journal of Advances in Modeling Earth Systems*, *17*(4), e2024MS004713. https://doi.org/10.1029/2024MS004713

Extier, T., Caley, T., & Roche, D. M. (2024). Modelling water isotopologues ($^{1}h^{2}h^{16}O$, $^{1}h^{217}O$) in the coupled numerical climate model iLOVECLIM (version 1.1. 5). *Geoscientific Model Development*, *17*(5), 2117–2139. https://doi.org/10.5194/gmd-17-2117-2024

Eyring, V., Bony, S., Meehl, G. A., Senior, C. A., Stevens, B., Stouffer, R. J., & Taylor, K. E. (2016). Overview of the Coupled Model Intercomparison Project Phase 6 (CMIP6) experimental design and organization. *Geoscientific Model Development*, *9*(5), 1937–1958. https://doi.org/10.5194/gmd-9-1937-2016

Fairall, C. W., Bradley, E. F., Hare, J., Grachev, A. A., & Edson, J. B. (2003). Bulk parameterization of air–sea fluxes: Updates and verification for the Coare algorithm. *Journal of Climate*, *16*(4), 571–591. https://doi.org/10.1175/1520-0442(2003)016⟨0571:BPOASF⟩2.0.CO;2

Federer, B., Brichet, N., & Jouzel, J. (1982). Stable isotopes in hailstones. Part I: The isotopic cloud model. *Journal of the Atmospheric Sciences*, *39*, 1323–1335. https://doi.org/10.1175/1520-0469(1982)039⟨1323:SIIHPI⟩2.0.CO;2

Field, R. D., Kim, D., LeGrande, A. N., Worden, J., Kelley, M., & Schmidt, G. A. (2014). Evaluating climate model performance in the tropics with retrievals of water isotopic composition from aura tes. *Geophysical Research Letters*, *41*(16), 6030–6036. https://doi.org/10.1002/2014GL060572

Fiorella, R. P., Siler, N., Nusbaumer, J., & Noone, D. C. (2021). Enhancing understanding of the hydrological cycle via pairing of process-oriented and isotope ratio tracers. *Journal of Advances in Modeling Earth Systems*, *13*(10), e2021MS002648. https://doi.org/10.1029/2021MS002648

Frazer, M., Bailey, A., Nusbaumer, J., Hu, J., Niezgoda, K., & Dee, S. (2025). CLUBB reduces low-cloud dependency on shallow convective mixing in the community atmosphere model: Insight from stable water isotopes. *Journal of Geophysical Research: Atmospheres*, *130*(13), e2024JD042053. https://doi.org/10.1029/2024JD042053

Galewsky, J. (2018). Using stable isotopes in water vapor to diagnose relationships between lower-tropospheric stability, mixing, and low-cloud cover near the island of Hawaii [Dataset]. *Geophysical Research Letters*, *45*(1), 297–305. https://doi.org/10.1002/2017GL075770

Galewsky, J. (2019). *Water vapor isotopic composition from the Azores field campaign report* (Technical Report No. DOE/SC-ARM-19-027). Oak Ridge National Laboratory (ORNL). (ARM Climate Research Facility).

Galewsky, J. (2024). Water vapor isotopic composition from Scripps Pier during EPCAPE [Dataset]. DOE ARM Data Center. https://doi.org/10.5439/2477150

Galewsky, J., Steen-Larsen, H. C., Field, R. D., Worden, J., Risi, C., & Schneider, M. (2016). Stable isotopes in atmospheric water vapor and applications to the hydrologic cycle. *Reviews of Geophysics*, *54*(4), 809–865. https://doi.org/10.1002/2015RG000512

Gettelman, A., & Morrison, H. (2015). Advanced two-moment bulk microphysics for global models. Part I: Off-line tests and comparison with other schemes. *Journal of Climate*, *28*(3), 1268–1287. https://doi.org/10.1175/JCLI-D-14-00102.1

Giorgetta, M. A., Jungclaus, J., Reick, C. H., Legutke, S., Bader, J., Böttinger, M., et al. (2013). Climate and carbon cycle changes from 1850 to 2100 in MPI-ESM simulations for the Coupled Model Intercomparison Project Phase 5. *Journal of Advances in Modeling Earth Systems*, *5*(3), 572–597. https://doi.org/10.1002/jame.20038

Gonfiantini, R. (1978). Standards for stable isotope measurements in natural compounds. *Nature*, *271*(5645), 534–536. https://doi.org/10.1038/271534a0

González, Y., Schneider, M., Dyroff, C., Rodríguez, S., Christner, E., García, O. E., et al. (2016). Detecting moisture transport pathways to the subtropical north Atlantic free troposphere using paired h^2O-δD in situ measurements [Dataset]. *Atmospheric Chemistry and Physics*, *16*(7), 4251–4269. https://doi.org/10.5194/acp-16-4251-2016

Graf, P., Wernli, H., Pfahl, S., & Sodemann, H. (2019). A new interpretative framework for below-cloud effects on stable water isotopes in vapour and rain. *Atmospheric Chemistry and Physics*, *19*(2), 747–765. https://doi.org/10.5194/acp-19-747-2019

Griffis, T. J., Wood, J. D., Baker, J. M., Lee, X., Xiao, K., Chen, Z., et al. (2016). Investigating the source, transport, and isotope composition of water vapor in the planetary boundary layer [Dataset]. *Atmospheric Chemistry and Physics*, *16*(8), 5139–5157. https://doi.org/10.5194/acp-16-5139-2016

Grootes, P. M., Stuiver, M., White, J., Johnsen, S., & Jouzel, J. (1993). Comparison of oxygen isotope records from the GISP2 and grip Greenland ice cores. *Nature*, *366*(6455), 552–554. https://doi.org/10.1038/366552a0

Harris, I., Osborn, T. J., Jones, P., & Lister, D. (2020). Version 4 of the cru ts monthly high-resolution gridded multivariate climate dataset [Dataset]. *Scientific Data*, *7*(1), 109. https://doi.org/10.1038/s41597-020-0453-3

He, C., Liu, Z., Otto-Bliesner, B., Brady, E., Zhu, C., Tomas, R., et al. (2021b). Hydroclimate footprint of Pan-Asian monsoon water isotope during the last deglaciation. *Science Advances*, *7*(4), eabe2611. https://doi.org/10.1126/sciadv.abe2611

He, C., Liu, Z., Otto-Bliesner, B. L., Brady, E. C., Zhu, C., Tomas, R., et al. (2021a). Abrupt Heinrich Stadial 1 cooling missing in Greenland oxygen isotopes. *Science Advances*, *7*(25), eabh1007. https://doi.org/10.1126/sciadv.abh1007

Held, I. M., & Soden, B. J. (2006). Robust responses of the hydrological cycle to global warming. *Journal of Climate*, *19*(21), 5686–5699. https://doi.org/10.1175/JCLI3990.1

Henry Juang, H.-M., & Hong, S.-Y. (2010). Forward semi-Lagrangian advection with mass conservation and positive definiteness for falling hydrometeors. *Monthly Weather Review*, *138*(5), 1778–1791. https://doi.org/10.1175/2009MWR3109.1

Hersbach, H., Bell, B., Berrisford, P., Hirahara, S., Horányi, A., Muñoz-Sabater, J., et al. (2020). The ERA5 global reanalysis [Dataset]. *Quarterly Journal of the Royal Meteorological Society*, *146*(730), 1999–2049. https://doi.org/10.1002/qj.3803

Hoffmann, G., Jouzel, J., & Masson, V. (2000). Stable water isotopes in atmospheric general circulation models. *Hydrological Processes*, *14*(8), 1385–1406. https://doi.org/10.1002/1099-1085(20000615)14:8⟨1385::AID-HYP989⟩3.0.CO;2-1

Hoffmann, G., Werner, M., & Heimann, M. (1998). Water isotope module of the ECHAM atmospheric general circulation model: A study on timescales from days to several years. *Journal of Geophysical Research*, *103*(D14), 16871–16896. https://doi.org/10.1029/98JD00423

Hourdin, F., Ferster, B., Deshayes, J., Mignot, J., Musat, I., & Williamson, D. (2023). Toward machine-assisted tuning avoiding the underestimation of uncertainty in climate change projections. *Science Advances*, *9*(29), eadf2758. https://doi.org/10.1126/sciadv.adf2758

Hourdin, F., Rio, C., Grandpeix, J.-Y., Madeleine, J.-B., Cheruy, F., Rochetin, N., et al. (2020). Lmdz6a: The atmospheric component of the IPSL climate model with improved and better tuned physics. *Journal of Advances in Modeling Earth Systems*, *12*(7), e2019MS001892. https://doi.org/10.1029/2019MS001892

Hu, J., Bailey, A., Nusbaumer, J., Dee, S., Sasser, C., & Worden, J. (2022). Tracking shallow convective mixing and its influence on low-level clouds with stable water isotopes in vapor. *Journal of Geophysical Research: Atmospheres*, *127*(5), e2021JD035355. https://doi.org/10.1029/2021JD035355

Hu, J., Emile-Geay, J., Nusbaumer, J., & Noone, D. (2018). Impact of convective activity on precipitation $\delta^{18}O$ in isotope-enabled general circulation models. *Journal of Geophysical Research: Atmospheres*, *123*(23), 13–595. https://doi.org/10.1029/2018JD029187

Hu, J., Yan, Y., Yeung, L. Y., & Dee, S. G. (2022). Sublimation origin of negative deuterium excess observed in snow and ice samples from McMurdo Dry Valleys and Allan Hills Blue Ice Areas, East Antarctica. *Journal of Geophysical Research: Atmospheres*, *127*(11), e2021JD035950. https://doi.org/10.1029/2021JD035950

IAEA/WMO. (2006). Global network of isotopes in precipitation [Dataset]. *International Atomic Energy Agency/World Meteor-ological Organization*. Retrieved from https://nucleus.iaea.org/wiser

Jacob, H., & Sonntag, C. (1991). An 8-year record of the seasonal variation of ^2H and ^{18}O in atmospheric water vapour and precipitation at Heidelberg, Germany [Dataset]. *Tellus B: Chemical and Physical Meteorology*, *43*(3), 291–300. https://doi.org/10.3402/tellusb.v43i3.15276

Jing, Z., Liu, Z., Zhang, S., Wen, Q., He, C., Bao, Y., & Yu, W. (2025). Precipitation oxygen isotope variability across timescales in East Asia records two sub-processes of summer monsoon system. *Communications Earth & Environment*, *6*(1), 513. https://doi.org/10.1038/s43247-025-02448-1

Joussaume, S., & Jouzel, J. (1993). Paleoclimatic tracers: An investigation using an atmospheric general circulation model under ice age conditions: 2. Water isotopes. *Journal of Geophysical Research*, *98*(D2), 2807–2830. https://doi.org/10.1029/92JD01920

Joussaume, S., Sadourny, R., & Jouzel, J. (1984). A general circulation model of water isotope cycles in the atmosphere. *Nature*, *311*(5981), 24–29. https://doi.org/10.1038/311024a0

Jouzel, J., Alley, R., Cuffey, K., Dansgaard, W., Grootes, P., Hoffmann, G., et al. (1997). Validity of the temperature reconstruction from water isotopes in ice cores. *Journal of Geophysical Research*, *102*(C12), 26471–26487. https://doi.org/10.1029/97JC01283

Jouzel, J., Hoffmann, G., Koster, R., & Masson, V. (2000). Water isotopes in precipitation:: Data/model comparison for present-day and past climates. *Quaternary Science Reviews*, *19*(1–5), 363–379. https://doi.org/10.1016/S0277-3791(99)00069-4

Jouzel, J., & Merlivat, L. (1984). Deuterium and oxygen 18 in precipitation: Modeling of the isotopic effects during snow formation. *Journal of Geophysical Research*, *89*(D7), 11749–11757. https://doi.org/10.1029/JD089iD07p11749

Jouzel, J., Russell, G., Suozzo, R., Koster, R., White, J., & Broecker, W. (1987). Simulations of the HDO and $H^2{}^{18}O$ atmospheric cycles using the NASA GISS general circulation model: The seasonal cycle for present-day conditions. *Journal of Geophysical Research*, *92*(D12), 14739–14760. https://doi.org/10.1029/JD092iD12p14739

Kalnay, E., Kanamitsu, M., Kistler, R., Collins, W., Deaven, D., Gandin, L., et al. (2018). The NCEP/NCAR 40-year reanalysis project. In *Renewable energy* (pp. 146–194). Routledge. https://doi.org/10.1175/1520-0477(1996)077⟨0437:TNYRP⟩2.0.CO;2

Kanamitsu, M., Ebisuzaki, W., Woollen, J., Yang, S.-K., Hnilo, J., Fiorino, M., & Potter, G. (2002). NCEP–DOE AMIP-II reanalysis (R-2) [Dataset]. *Bulletin of the American Meteorological Society*, *83*(11), 1631–1644. https://doi.org/10.1175/BAMS-83-11-1631

Kanamitsu, M., Kumar, A., Juang, H.-M. H., Schemm, J.-K., Wang, W., Yang, F., et al. (2002). NCEP dynamical seasonal forecast system 2000 [Dataset]. *Bulletin of the American Meteorological Society*, *83*(7), 1019–1038. https://doi.org/10.1175/1520-0477(2002)083⟨1019:NDSFS⟩2.3.CO;2

Kelley, M., Schmidt, G. A., Nazarenko, L. S., Bauer, S. E., Ruedy, R., Russell, G. L., et al. (2020). GISS-E2. 1: Configurations and climatology. *Journal of Advances in Modeling Earth Systems*, *12*(8), e2019MS002025. https://doi.org/10.1029/2019MS002025

Kino, K., Okazaki, A., Cauquoin, A., & Yoshimura, K. (2021). Contribution of the southern annular mode to variations in water isotopes of daily precipitation at dome Fuji, East Antarctica. *Journal of Geophysical Research: Atmospheres*, *126*(23), e2021JD035397. https://doi.org/10.1029/2021JD035397

Kobayashi, S., Ota, Y., Harada, Y., Ebita, A., Moriya, M., Onoda, H., et al. (2015). The jra-55 reanalysis: General specifications and basic characteristics [Dataset]. *Journal of the Meteorological Society of Japan. Series II*, *93*(1), 5–48. https://doi.org/10.2151/jmsj.2015-001

Konecky, B., Noone, D., & Cobb, K. (2019). The influence of competing hydroclimate processes on stable isotope ratios in tropical rainfall. *Geophysical Research Letters*, *46*(3), 1622–1633. https://doi.org/10.1029/2018GL080188

Koster, R. D., Bosilovich, M. G., Akella, S., Lawrence, C., Cullather, R., Draper, C., et al. (2016). *MERRA-2: Initial evaluation of the climate (dataset nos. NASA/TM–2015–104606, Vol. 43)*. (NASA Technical Report Series on Global Modeling and Data Assimilation). NASA Goddard Space Flight Center. https://doi.org/10.5067/QBZ6MG944HW0

Koster, R. D., Sud, Y., Guo, Z., Dirmeyer, P. A., Bonan, G., Oleson, K. W., et al. (2006). Glace: The global land–atmosphere coupling experiment. Part I: Overview. *Journal of Hydrometeorology*, *7*(4), 590–610. https://doi.org/10.1175/JHM510.1

Kurita, N., Fujiyoshi, Y., Nakayama, T., Matsumi, Y., & Kitagawa, H. (2015). East Asian monsoon controls on the inter-annual variability in precipitation isotope ratio in Japan [Dataset]. *Climate of the Past*, *11*(2), 339–353. https://doi.org/10.5194/cp-11-339-2015

Kurita, N., Newman, B., Araguas-Araguas, L., & Aggarwal, P. (2012). Evaluation of continuous water vapor δD and $\delta^{18}O$ measurements by off-axis integrated cavity output spectroscopy. *Atmospheric Measurement Techniques Discussions*, *5*(2), 2821–2855. https://doi.org/10.5194/amt-5-2069-2012

Kurita, N., Noone, D., Risi, C., Schmidt, G. A., Yamada, H., & Yoneyama, K. (2011). Intraseasonal isotopic variation associated with the Madden-Julian oscillation. *Journal of Geophysical Research*, *116*(D24). https://doi.org/10.1029/2010JD015209

Lai, C.-T., Rambo, J., Welp-Smith, L., Bible, K., & Hollinger, D. Y. (2014). Comparing stable water isotope variation in atmospheric moisture observed over coastal water and forests. In *Abstract PP31D-1162 presented at 2014 Fall Meeting, AGU, San Francisco, Calif., 15–19 Dec*. https://doi.org/10.1002/2015RG000512

Lamb, K. D., Clouser, B. W., Bolot, M., Sarkozy, L., Ebert, V., Saathoff, H., et al. (2017). Laboratory measurements of HDO/H_2O isotopic fractionation during ice deposition in simulated cirrus clouds. *Proceedings of the National Academy of Sciences*, *114*(22), 5612–5617. https://doi.org/10.1073/pnas.1618374114

Landais, A., Agosta, C., Vimeux, F., Magand, O., Solis, C., Cauquoin, A., et al. (2024). Abrupt excursions in water vapor isotopic variability at the pointe benedicte observatory on Amsterdam island [Dataset]. *Atmospheric Chemistry and Physics*, *24*(8), 4611–4634. https://doi.org/10.5194/acp-24-4611-2024

Laskar, A. H., Huang, J.-C., Hsu, S.-C., Bhattacharya, S. K., Wang, C.-H., & Liang, M.-C. (2014). Stable isotopic composition of near surface atmospheric water vapor and rain–vapor interaction in Taipei, Taiwan [Dataset]. *Journal of Hydrology*, *519*, 2091–2100. https://doi.org/10.1016/j.jhydrol.2014.10.017

Lawrence, J. R., Gedzelman, S. D., Dexheimer, D., Cho, H.-K., Carrie, G. D., Gasparini, R., et al. (2004). Stable isotopic composition of water vapor in the tropics. *Journal of Geophysical Research*, *109*(D6). https://doi.org/10.1029/2003JD004046

Lee, J.-E., & Fung, I. (2008). "Amount effect" of water isotopes and quantitative analysis of post-condensation processes. *Hydrological Processes: International Journal*, *22*(1), 1–8. https://doi.org/10.1002/hyp.6637

Lee, J.-E., Fung, I., DePaolo, D. J., & Henning, C. C. (2007). Analysis of the global distribution of water isotopes using the ncar atmospheric general circulation model. *Journal of Geophysical Research*, *112*(D16). https://doi.org/10.1029/2006JD007657

Lee, J.-E., Pierrehumbert, R., Swann, A., & Lintner, B. R. (2009). Sensitivity of stable water isotopic values to convective parameterization schemes. *Geophysical Research Letters*, *36*(23). https://doi.org/10.1029/2009GL040880

Lee, X., Smith, R., & Williams, J. (2006). Water vapour $^{18}O/^{16}O$ isotope ratio in surface air in new England, USA [Dataset]. *Tellus B: Chemical and Physical Meteorology*, *58*(4), 293–304. https://doi.org/10.1111/j.1600-0889.2006.00191.x

LeGrande, A., & Schmidt, G. (2009). Sources of Holocene variability of oxygen isotopes in paleoclimate archives. *Climate of the Past*, *5*(3), 441–455. https://doi.org/10.5194/cp-5-441-2009

LeGrande, A. N., & Schmidt, G. A. (2006). Global gridded data set of the oxygen isotopic composition in seawater. *Geophysical Research Letters*, *33*(12). https://doi.org/10.1029/2006GL026011

Leroy-Dos Santos, C., Fourré, E., Agosta, C., Casado, M., Cauquoin, A., Werner, M., et al. (2023). From atmospheric water isotopes measurement to firn core interpretation in Adélie land: A case study for isotope-enabled atmospheric models in Antarctica [Dataset]. *The Cryosphere*, *17*(12), 5241–5254. https://doi.org/10.5194/tc-17-5241-2023

Leroy-Dos Santos, C., Masson-Delmotte, V., Casado, M., Fourré, E., Steen-Larsen, H., Maturilli, M., et al. (2020). A 4.5 year-long record of Svalbard water vapor isotopic composition documents winter air mass origin [Dataset]. *Journal of Geophysical Research: Atmospheres*, *125*(23), e2020JD032681. https://doi.org/10.1029/2020JD032681

Liu, Z., Wen, X., Brady, E., Otto-Bliesner, B., Yu, G., Lu, H., et al. (2014). Chinese cave records and the east Asia summer monsoon. *Quaternary Science Reviews*, *83*, 115–128. https://doi.org/10.1016/j.quascirev.2013.10.021

Louis, J.-F. (1979). A parametric model of vertical eddy fluxes in the atmosphere. *Boundary-Layer Meteorology*, *17*(2), 187–202. https://doi.org/10.1007/BF00117978

Luz, B., & Barkan, E. (2005). The isotopic ratios $^{17}O/^{16}O$ and $^{18}O/^{16}O$ in molecular oxygen and their significance in biogeochemistry. *Geochimica et Cosmochimica Acta*, *69*(5), 1099–1110. https://doi.org/10.1016/j.gca.2004.09.001

Madsen, M. V., Steen-Larsen, H. C., Hörhold, M., Box, J., Berben, S. M. P., Capron, E., et al. (2019). Evidence of isotopic fractionation during vapor exchange between the atmosphere and the snow surface in Greenland. *Journal of Geophysical Research: Atmospheres*, *124*(6), 2932–2945. https://doi.org/10.1029/2018JD029619

Majoube, M. (1971a). Fractionnement en oxygène 18 et en deutérium entre l'eau et sa vapeur. *Journal de Chimie Physique*, *68*, 1423–1436. https://doi.org/10.1051/jcp/1971681423

Majoube, M. (1971b). Oxygen-18 and deuterium fractionation between water and steam. *J. Clim. Phys.*, *68*(10), 1423–1436. https://doi.org/10.1051/jcp/1971681423

Masiol, M., Zannoni, D., Stenni, B., Dreossi, G., Zini, L., Calligaris, C., et al. (2021). Spatial distribution and interannual trends of $\delta^{18}O$, $\delta^{2}H$, and deuterium excess in precipitation across north-eastern Italy. *Journal of Hydrology*, *598*, 125749. https://doi.org/10.1016/j.jhydrol.2020.125749

Masson-Delmotte, V., Hou, S., Ekaykin, A., Jouzel, J., Aristarain, A., Bernardo, R., et al. (2008). A review of antarctic surface snow isotopic composition: Observations, atmospheric circulation, and isotopic modeling [Dataset]. *Journal of Climate*, *21*(13), 3359–3387. https://doi.org/10.1175/2007JCLI2139.1

Mathieu, R., Pollard, D., Cole, J. E., White, J. W., Webb, R. S., & Thompson, S. L. (2002). Simulation of stable water isotope variations by the GENESIS GCM for modern conditions. *Journal of Geophysical Research*, *107*(D4). ACL-2. https://doi.org/10.1029/2001JD900255

Mauritsen, T., Bader, J., Becker, T., Behrens, J., Bittner, M., Brokopf, R., et al. (2019). Developments in the MPI-M Earth system model version 1.2 (MPI-ESM1. 2) and its response to increasing CO_2. *Journal of Advances in Modeling Earth Systems*, *11*(4), 998–1038. https://doi.org/10.1029/2018MS001400

McFarlane, N. (1987). The effect of orographically excited gravity wave drag on the general circulation of the lower stratosphere and troposphere. *Journal of the Atmospheric Sciences*, *44*(14), 1775–1800. https://doi.org/10.1175/1520-0469(1987)044⟨1775:TEOOEG⟩2.0.CO;2

Meinshausen, M., Nicholls, Z. R., Lewis, J., Gidden, M. J., Vogel, E., Freund, M., et al. (2020). The shared socio-economic pathway (SSP) greenhouse gas concentrations and their extensions to 2500. *Geoscientific Model Development*, *13*(8), 3571–3605. https://doi.org/10.5194/gmd-13-3571-2020

Merlivat, L. (1978). Molecular diffusivities of H_2 ^{16}O, $HD^{16}O$, and H^2 ^{18}O in gases. *The Journal of Chemical Physics*, *69*(6), 2864–2871. https://doi.org/10.1063/1.436884

Merlivat, L., & Jouzel, J. (1979). Global climatic interpretation of the deuterium-oxygen 18 relationship for precipitation. *Journal of Geophysical Research*, *84*(C8), 5029–5033. https://doi.org/10.1029/JC084iC08p05029

Merlivat, L., & Nief, G. (1967). Fractionnement isotopique lors des changements d 'état solide-vapeur et liquide-vapeur de l'eau à des températures inférieures à 0 c. *Tellus*, *19*(1), 122–127. https://doi.org/10.3402/tellusa.v19i1.9756

Miller, M. F. (2002). Isotopic fractionation and the quantification of ^{17}O anomalies in the oxygen three-isotope system: An appraisal and geochemical significance. *Geochimica et Cosmochimica Acta*, *66*(11), 1881–1889. https://doi.org/10.1016/S0016-7037(02)00832-3

Moncrieff, M. W., Liu, C., & Bogenschutz, P. (2017). Simulation, modeling, and dynamically based parameterization of organized tropical convection for global climate models. *Journal of the Atmospheric Sciences*, *74*(5), 1363–1380. https://doi.org/10.1175/JAS-D-16-0166.1

Moon, I.-J., Ginis, I., Hara, T., & Thomas, B. (2007). A physics-based parameterization of air–sea momentum flux at high wind speeds and its impact on hurricane intensity predictions. *Monthly Weather Review*, *135*(8), 2869–2878. https://doi.org/10.1175/MWR3432.1

Morrison, H., & Gettelman, A. (2008). A new two-moment bulk stratiform cloud microphysics scheme in the community atmosphere model, version 3 (CAM3). Part I: Description and numerical tests. *Journal of Climate*, *21*(15), 3642–3659. https://doi.org/10.1175/2008JCLI2105.1

Nakanishi, M., & Niino, H. (2006). An improved Mellor–Yamada level-3 model: Its numerical stability and application to a regional prediction of advection fog. *Boundary-Layer Meteorology*, *119*(2), 397–407. https://doi.org/10.1007/s10546-005-9030-8

Neale, R., Gettelman, A., Park, S., Chen, C.-C., Lauritzen, P. H., Williamson, D., et al. (2012). *Description of the NCAR community atmosphere model (CAM 5.0)* (Technical Report). National Center for Atmospheric Research. https://doi.org/10.5065/wgtk-4g06

Nitta, T., Yoshimura, K., Takata, K., O'ishi, R., Sueyoshi, T., Kanae, S., et al. (2014). Representing variability in subgrid snow cover and snow depth in a global land model: Offline validation. *Journal of Climate*, *27*(9), 3318–3330. https://doi.org/10.1175/JCLI-D-13-00310.1

Noda, A. T., Oouchi, K., Satoh, M., Tomita, H., Iga, S.-I., & Tsushima, Y. (2010). Importance of the subgrid-scale turbulent moist process: Cloud distribution in global cloud-resolving simulations. *Atmospheric Research*, *96*(2–3), 208–217. https://doi.org/10.1016/j.atmosres.2009.05.007

Noël, S., Reuter, M., Buchwitz, M., Borchardt, J., Hilker, M., Schneising, O., et al. (2022). Retrieval of greenhouse gases from GOSAT and GOSAT-2 using the FOCAL algorithm. *Atmospheric Measurement Techniques*, *15*(11), 3401–3437. https://doi.org/10.5194/amt-15-3401-2022

Noone, D. (2012). Pairing measurements of the water vapor isotope ratio with humidity to deduce atmospheric moistening and dehydration in the tropical midtroposphere. *Journal of Climate*, *25*(13), 4476–4494. https://doi.org/10.1175/JCLI-D-11-00582.1

Noone, D., & Simmonds, I. (2002). Associations between $\delta^{18}O$ of water and climate parameters in a simulation of atmospheric circulation for 1979–95. *Journal of Climate*, *15*(22), 3150–3169. https://doi.org/10.1175/1520-0442(2002)015⟨3150:ABOOWA⟩2.0.CO;2

Nusbaumer, J., Wong, T. E., Bardeen, C., & Noone, D. (2017). Evaluating hydrological processes in the Community Atmosphere Model Version 5 (CAM5) using stable isotope ratios of water. *Journal of Advances in Modeling Earth Systems*, *9*(2), 949–977. https://doi.org/10.1002/2016MS000839

Okazaki, A., & Yoshimura, K. (2017). Development and evaluation of a system of proxy data assimilation for paleoclimate reconstruction. *Climate of the Past*, *13*(4), 379–393. https://doi.org/10.5194/cp-13-379-2017

Okazaki, A., & Yoshimura, K. (2019). Global evaluation of proxy system models for stable water isotopes with realistic atmospheric forcing. *Journal of Geophysical Research: Atmospheres*, *124*(16), 8972–8993. https://doi.org/10.1029/2018JD029463

Ollivier, I., Steen-Larsen, H. C., Stenni, B., Arnaud, L., Casado, M., Cauquoin, A., et al. (2025). Surface processes and drivers of the snow water stable isotopic composition at Dome C, East Antarctica–a multi-dataset and modelling analysis. *The Cryosphere*, *19*(1), 173–200. https://doi.org/10.5194/tc-19-173-2025

Prudhomme, C., Giuntoli, I., Robinson, E. L., Clark, D. B., Arnell, N. W., Dankers, R., et al. (2014). Hydrological droughts in the 21st century, hotspots and uncertainties from a global multimodel ensemble experiment. *Proceedings of the National Academy of Sciences*, *111*(9), 3262–3267. https://doi.org/10.1073/pnas.1222473110

Putman, A. L., Bowen, G. J., & Strong, C. (2021). Local and regional modes of hydroclimatic change expressed in modern multidecadal precipitation oxygen isotope trends. *Geophysical Research Letters*, *48*(5), e2020GL092006. https://doi.org/10.1029/2020GL092006

Ramos, R., LeGrande, A., Griffiths, M., Elsaesser, G., Litchmore, D., Tierney, J., et al. (2022). Constraining clouds and convective parameterizations in a climate model using paleoclimate data. *Journal of Advances in Modeling Earth Systems*, *14*(8), e2021MS002893. https://doi.org/10.1029/2021MS002893

Rind, D., Orbe, C., Jonas, J., Nazarenko, L., Zhou, T., Kelley, M., et al. (2020). GISS Model E2. 2: A climate model optimized for the middle atmosphere—Model structure, climatology, variability, and climate sensitivity. *Journal of Geophysical Research: Atmospheres*, *125*(10), e2019JD032204. https://doi.org/10.1029/2019JD032204

Risi, C., Bony, S., & Vimeux, F. (2008). Influence of convective processes on the isotopic composition ($\delta^{18}O$ and δD) of precipitation and water vapor in the tropics: 2. physical interpretation of the amount effect. *Journal of Geophysical Research*, *113*(D19). https://doi.org/10.1029/2008JD009943

Risi, C., Bony, S., Vimeux, F., & Jouzel, J. (2010). Water-stable isotopes in the lmdz4 general circulation model: Model evaluation for present-day and past climates and applications to climatic interpretations of tropical isotopic records. *Journal of Geophysical Research*, *115*(D12). https://doi.org/10.1029/2009JD013255

Risi, C., Landais, A., Winkler, R., & Vimeux, F. (2013). Can we determine what controls the spatio-temporal distribution of d-excess and ^{17}O-excess in precipitation using the lmdz general circulation model? *Climate of the Past*, *9*(5), 2173–2193. https://doi.org/10.5194/cp-9-2173-2013

Risi, C., Noone, D., Worden, J., Frankenberg, C., Stiller, G., Kiefer, M., et al. (2012). Process-evaluation of tropospheric humidity simulated by general circulation models using water vapor isotopologues: 1. Comparison between models and observations. *Journal of Geophysical Research*, *117*(D5). https://doi.org/10.1029/2011JD016623

Ritter, F., Steen-Larsen, H. C., Werner, M., Masson-Delmotte, V., Orsi, A., Behrens, M., et al. (2016). Isotopic exchange on the diurnal scale between near-surface snow and lower atmospheric water vapor at kohnen station, east Antarctica. *The Cryosphere*, *10*(4), 1647–1663. https://doi.org/10.5194/tc-10-1647-2016

Roche, D. M. (2013). δ 18 o water isotope in the iloveclim model (version 1.0)–Part 1: Implementation and verification. *Geoscientific Model Development*, *6*(5), 1481–1491. https://doi.org/10.5194/gmd-6-1481-2013

Roh, W., & Satoh, M. (2014). Evaluation of precipitating hydrometeor parameterizations in a single-moment bulk microphysics scheme for deep convective systems over the tropical central Pacific. *Journal of the Atmospheric Sciences*, *71*(7), 2654–2673. https://doi.org/10.1175/JAS-D-13-0252.1

Roh, W., Satoh, M., & Nasuno, T. (2017). Improvement of a cloud microphysics scheme for a global nonhydrostatic model using trmm and a satellite simulator. *Journal of the Atmospheric Sciences*, *74*(1), 167–184. https://doi.org/10.1175/JAS-D-16-0027.1

Rozanski, K., Araguás-Araguás, L., & Gonfiantini, R. (1993). Isotopic patterns in modern global precipitation. *Climate change in continental isotopic records*, *78*, 1–36. https://doi.org/10.1029/GM078p0001

Salamalikis, V., Argiriou, A., & Dotsika, E. (2015). Stable isotopic composition of atmospheric water vapor in Patras, Greece: A concentration weighted trajectory approach [Dataset]. *Atmospheric Research*, *152*, 93–104. https://doi.org/10.1016/j.atmosres.2014.02.021

Samuels-Crow, K. E., Galewsky, J., Sharp, Z. D., & Dennis, K. J. (2014). Deuterium excess in subtropical free troposphere water vapor: Continuous measurements from the Chajnantor Plateau, northern Chile [Dataset]. *Geophysical Research Letters*, *41*(23), 8652–8659. https://doi.org/10.1002/2014GL062302

Satoh, M., Matsuno, T., Tomita, H., Miura, H., Nasuno, T., & Iga, S.-I. (2008). Nonhydrostatic icosahedral atmospheric model (NICAM) for global cloud resolving simulations. *Journal of Computational Physics*, *227*(7), 3486–3514. https://doi.org/10.1016/j.jcp.2007.02.006

Satoh, M., Tomita, H., Yashiro, H., Miura, H., Kodama, C., Seiki, T., et al. (2014). The non-hydrostatic icosahedral atmospheric model: Description and development. *Progress in Earth and Planetary Science*, *1*, 1–32. https://doi.org/10.1186/s40645-014-0018-1

Schmidt, G. A. (1999). Forward modeling of carbonate proxy data from planktonic Foraminifera using oxygen isotope tracers in a global ocean model. *Paleoceanography*, *14*(4), 482–497. https://doi.org/10.1029/1999PA900025

Schmidt, G. A., Hoffmann, G., Shindell, D. T., & Hu, Y. (2005). Modeling atmospheric stable water isotopes and the potential for constraining cloud processes and stratosphere-troposphere water exchange. *Journal of Geophysical Research*, *110*(D21). https://doi.org/10.1029/2005JD005790

Schmidt, G. A., Kelley, M., Nazarenko, L., Ruedy, R., Russell, G. L., Aleinov, I., et al. (2014). Configuration and assessment of the GISS ModelE2 contributions to the CMIP5 archive. *Journal of Advances in Modeling Earth Systems*, *6*(1), 141–184. https://doi.org/10.1002/2013MS000265

Schmidt, G. A., Ruedy, R., Hansen, J. E., Aleinov, I., Bell, N., Bauer, M., et al. (2006). Present-day atmospheric simulations using giss modele: Comparison to in situ, satellite, and reanalysis data. *Journal of Climate*, *19*(2), 153–192. https://doi.org/10.1175/JCLI3612.1

Schneider, A., Borsdorff, T., Aan de Brugh, J., Lorente, A., Aemisegger, F., Noone, D., et al. (2022). Retrieving H^2 O/HDO columns over cloudy and clear-sky scenes from the tropospheric monitoring instrument (tropomi) [Dataset]. *Atmospheric Measurement Techniques*, *15*(7), 2251–2275. https://doi.org/10.5194/amt-15-2251-2022

Schneider, M., Toride, K., Khosrawi, F., Hase, F., Ertl, B., Diekmann, C. J., & Yoshimura, K. (2024). Assessing the potential of free-tropospheric water vapour isotopologue satellite observations for improving the analyses of convective events. *Atmospheric Measurement Techniques*, *17*(17), 5243–5259. https://doi.org/10.5194/amt-17-5243-2024

Schneider, T., O'Gorman, P. A., & Levine, X. J. (2010). Water vapor and the dynamics of climate changes. *Reviews of Geophysics*, *48*(3). https://doi.org/10.1029/2009RG000302

Sekiguchi, M., & Nakajima, T. (2008). A k-distribution-based radiation code and its computational optimization for an atmospheric general circulation model. *Journal of Quantitative Spectroscopy and Radiative Transfer*, *109*(17–18), 2779–2793. https://doi.org/10.1016/j.jqsrt.2008.07.013

Siler, N., Fiorella, R. P., & Kukla, T. (2025). A unified interpretation of variability in precipitation isotope ratios. *Journal of Climate*, *38*(6), 1403–1420. https://doi.org/10.1175/JCLI-D-24-0427.1

Sjolte, J., Hoffmann, G., & Johnsen, S. J. (2014). Modelling the response of stable water isotopes in Greenland precipitation to orbital configurations of the previous interglacial. *Tellus B: Chemical and Physical Meteorology*, *66*(1), 22872. https://doi.org/10.3402/tellusb.v66.22872

Steen-Larsen, H., Risi, C., Werner, M., Yoshimura, K., & Masson-Delmotte, V. (2017). Evaluating the skills of isotope-enabled general circulation models against in situ atmospheric water vapor isotope observations. *Journal of Geophysical Research: Atmospheres*, *122*(1), 246–263. https://doi.org/10.1002/2016JD025443

Steen-Larsen, H., Sveinbjörnsdottir, A., Jonsson, T., Ritter, F., Bonne, J.-L., Masson-Delmotte, V., et al. (2015). Moisture sources and synoptic to seasonal variability of north Atlantic water vapor isotopic composition [Dataset]. *Journal of Geophysical Research: Atmospheres*, *120*(12), 5757–5774. https://doi.org/10.1002/2015JD023234

Steen-Larsen, H. C., Sveinbjörnsdottir, A. E., Peters, A., Masson-Delmotte, V., Guishard, M., Hsiao, G., et al. (2014). Climatic controls on water vapor deuterium excess in the marine boundary layer of the north Atlantic based on 500 days of in situ, continuous measurements [Dataset]. *Atmospheric Chemistry and Physics*, *14*(15), 7741–7756. https://doi.org/10.5194/acp-14-7741-2014

Steiger, N. J., Steig, E. J., Dee, S. G., Roe, G. H., & Hakim, G. J. (2017). Climate reconstruction using data assimilation of water isotope ratios from ice cores. *Journal of Geophysical Research: Atmospheres*, *122*(3), 1545–1568. https://doi.org/10.1002/2016JD026011

Stenni, B., Scarchilli, C., Masson-Delmotte, V., Schlosser, E., Ciardini, V., Dreossi, G., et al. (2016). Three-year monitoring of stable isotopes of precipitation at concordia station, east Antarctica. *The Cryosphere*, *10*(5), 2415–2428. https://doi.org/10.5194/tc-10-2415-2016

Stevens, B., Giorgetta, M., Esch, M., Mauritsen, T., Crueger, T., Rast, S., et al. (2013). Atmospheric component of the mpi-m Earth system model: ECHAM6. *Journal of Advances in Modeling Earth Systems*, *5*(2), 146–172. https://doi.org/10.1002/jame.20015

Stevenson, S., Coats, S., Touma, D., Cole, J., Lehner, F., Fasullo, J., & Otto-Bliesner, B. (2022). Twenty-first century hydroclimate: A continually changing baseline, with more frequent extremes. *Proceedings of the National Academy of Sciences*, *119*(12), e2108124119. https://doi.org/10.1073/pnas.2108124119

Stewart, M. K. (1975). Stable isotope fractionation due to evaporation and isotopic exchange of falling waterdrops: Applications to atmospheric processes and evaporation of lakes. *Journal of Geophysical Research*, *80*(9), 1133–1146. https://doi.org/10.1029/JC080i009p01133

Tada, M., Yoshimura, K., & Toride, K. (2021). Improving weather forecasting by assimilation of water vapor isotopes. *Scientific Reports*, *11*(1), 18067. https://doi.org/10.1038/s41598-021-97476-0

Takata, K., Emori, S., & Watanabe, T. (2003). Development of the minimal advanced treatments of surface interaction and runoff. *Global and Planetary Change*, *38*(1–2), 209–222. https://doi.org/10.1016/S0921-8181(03)00030-4

Tanoue, M., Yashiro, H., Takano, Y., Yoshimura, K., Kodama, C., & Satoh, M. (2023). Modeling water isotopes using a global non-hydrostatic model with an explicit convection: Comparison with gridded data sets and site observations. *Journal of Geophysical Research: Atmospheres*, *128*(23), e2021JD036419. https://doi.org/10.1029/2021JD036419

Tharammal, T., Bala, G., & Noone, D. (2017). Impact of deep convection on the isotopic amount effect in tropical precipitation. *Journal of Geophysical Research: Atmospheres*, *122*(3), 1505–1523. https://doi.org/10.1002/2016JD025555

Thornton, E. (2010). Technical description of version 4.0 of the community land model (CLM). *NCAR, Climate and Global*.

Tian, L., Yu, W., Schuster, P. F., Wen, R., Cai, Z., Wang, D., et al. (2020). Control of seasonal water vapor isotope variations at Lhasa, southern Tibetan plateau [Dataset]. *Journal of Hydrology*, *580*, 124237. https://doi.org/10.1016/j.jhydrol.2019.124237

Tierney, J. E., Russell, J. M., Huang, Y., Damsté, J. S. S., Hopmans, E. C., & Cohen, A. S. (2008). Northern hemisphere controls on tropical southeast African climate during the past 60,000 years. *Science*, *322*(5899), 252–255. https://doi.org/10.1126/science.1160485

Tindall, J., Valdes, P., & Sime, L. C. (2009). Stable water isotopes in hadcm3: Isotopic signature of el niño–southern oscillation and the tropical amount effect. *Journal of Geophysical Research*, *114*(D4). https://doi.org/10.1029/2008JD010825

Tomita, H. (2008). New microphysical schemes with five and six categories by diagnostic generation of cloud ice. *Journal of the Meteorological Society of Japan. Series II*, *86*, 121–142. https://doi.org/10.2151/jmsj.86A.121

Toride, K., Yoshimura, K., Tada, M., Diekmann, C., Ertl, B., Khosrawi, F., & Schneider, M. (2021). Potential of mid-tropospheric water vapor isotopes to improve large-scale circulation and weather predictability. *Geophysical Research Letters*, *48*(5), e2020GL091698. https://doi.org/10.1029/2020GL091698

Tremoy, G., Vimeux, F., Mayaki, S., Souley, I., Cattani, O., Risi, C., et al. (2012). A 1-year long $\delta^{18}O$ record of water vapor in Niamey (Niger) reveals insightful atmospheric processes at different timescales [Dataset]. *Geophysical Research Letters*, *39*(8). https://doi.org/10.1029/2012GL051298

Trenberth, K. E. (1999). Conceptual framework for changes of extremes of the hydrological cycle with climate change. In *Weather and climate extremes* (pp. 327–339). Springer. https://doi.org/10.1023/A:1005488920935

Trenberth, K. E. (2011). Changes in precipitation with climate change. *Climate Research*, *47*(1–2), 123–138. https://doi.org/10.3354/cr00953

Trenberth, K. E., Fasullo, J. T., & Mackaro, J. (2011). Atmospheric moisture transports from ocean to land and global energy flows in reanalyses. *Journal of Climate*, *24*(18), 4907–4924. https://doi.org/10.1175/2011JCLI4171.1

Tripti, M., Lambs, L., Moussa, I., & Corenblit, D. (2019). Evidence of elevation effect on stable isotopes of water along highlands of a humid tropical mountain belt (western Ghats, India) experiencing monsoonal climate. *Journal of Hydrology*, *573*, 469–485. https://doi.org/10.1016/j.jhydrol.2019.03.086

Tsai, I., Chen, W.-Y., Chen, J.-P., & Liang, M.-C. (2019). Kinetic mass-transfer calculation of water isotope fractionation due to cloud microphysics in a regional meteorological model. *Atmospheric Chemistry and Physics*, *19*(3), 1753–1766. https://doi.org/10.5194/acp-19-1753-2019

Vimeux, F., Risi, C., Barthe, C., François, S., Cauquoin, A., Jossoud, O., et al. (2024). Is the isotopic composition of precipitation a robust indicator for reconstructions of past tropical cyclones frequency? A case study on Réunion island from rain and water vapor isotopic observations [Dataset]. *Journal of Geophysical Research: Atmospheres*, *129*(3), e2023JD039794. https://doi.org/10.1029/2023JD039794

Vimeux, F., Tremoy, G., Cattani, O., & Risi, C. (2014). Utilisation de la composition isotopique de la vapeur d'eau au sirta pour l'étude des processus atmosphériques, de l'échelle locale à la grande échelle [Dataset]. *Journées scientifiques sirta 2014*, 12. https://doi.org/10.1002/2015RG000512

Vimeux, F., Tremoy, G., Roca, M., Moreno, I., Cattani, O., Guilpart, E., et al. (2015). Continuous measurements of surface water vapor isotopic ratios in the Bolivian Andes during the monsoon period: Influence of regional convection and air masses mixing [Dataset]. In *EGU general assembly conference abstracts* (p. 5964). Retrieved from https://ui.adsabs.harvard.edu/abs/2015EGUGA..17.5964V/abstract

Vystavna, Y., Matiatos, I., & Wassenaar, L. (2021). Temperature and precipitation effects on the isotopic composition of global precipitation reveal long-term climate dynamics. *Scientific Reports*, *11*(1), 18503. https://doi.org/10.1038/s41598-021-98094-6

Wahl, S., Steen-Larsen, H. C., Hughes, A. G., Dietrich, L. J., Zuhr, A., Behrens, M., et al. (2022). Atmosphere-snow exchange explains surface snow isotope variability. *Geophysical Research Letters*, *49*(20), e2022GL099529. https://doi.org/10.1029/2022GL099529

Wahl, S., Walter, B., Aemisegger, F., Bianchi, L., & Lehning, M. (2024). Identifying airborne snow metamorphism with stable water isotopes. *The Cryosphere*, *18*(9), 4493–4515. https://doi.org/10.5194/tc-18-4493-2024

Wang, Y.-J., Cheng, H., Edwards, R. L., An, Z., Wu, J., Shen, C.-C., & Dorale, J. A. (2001). A high-resolution absolute-dated late pleistocene monsoon record from hulu cave, China. *Science*, *294*(5550), 2345–2348. https://doi.org/10.1126/science.1064618

Watanabe, M., Suzuki, T., O'ishi, R., Komura, Y., Watanabe, S., Emori, S., et al. (2010). Improved climate simulated by MIROC5: Mean states, variability, and climate sensitivity. *Journal of Climate*, *23*, 6312–=6335. https://doi.org/10.1175/2010JCLI3679.1

Wei, Z., Yoshimura, K., Okazaki, A., Ono, K., Kim, W., Yokoi, M., & Lai, C.-T. (2016). Understanding the variability of water isotopologues in near-surface atmospheric moisture over a humid subtropical rice paddy in Tsukuba, Japan [Dataset]. *Journal of Hydrology*, *533*, 91–102. https://doi.org/10.1016/j.jhydrol.2015.11.044

Wen, X.-F., Zhang, S.-C., Sun, X.-M., Yu, G.-R., & Lee, X. (2010). Water vapor and precipitation isotope ratios in Beijing, China [Dataset]. *Journal of Geophysical Research*, *115*(D1). https://doi.org/10.1029/2009JD012408

Werner, M., Barras, V., Brown, J., Gourcy, L., Henderson-Sellers, A., Hoffmann, G., et al. (2004). *The stable water isotope intercomparison group (swing) – Results of a new model intercomparison study (abstract)*. American geophysical union, fall meeting. (Abstract).

Werner, M., Langebroek, P. M., Carlsen, T., Herold, M., & Lohmann, G. (2011). Stable water isotopes in the ECHAM5 general circulation model: Toward high-resolution isotope modeling on a global scale. *Journal of Geophysical Research*, *116*(D15), D15109. https://doi.org/10.1029/2011JD015681

Werner, M., Mikolajewicz, U., Heimann, M., & Hoffmann, G. (2000). Borehole versus isotope temperatures on Greenland: Seasonality does matter. *Geophysical Research Letters*, *27*(5), 723–726. https://doi.org/10.1029/1999GL006075

Wong, T. E., Nusbaumer, J., & Noone, D. C. (2017). Evaluation of modeled land-atmosphere exchanges with a comprehensive water isotope fractionation scheme in version 4 of the community land model. *Journal of Advances in Modeling Earth Systems*, *9*(2), 978–1001. https://doi.org/10.1002/2016MS000842

Worden, J., Bowman, K., Noone, D., Beer, R., Clough, S., Eldering, A., et al. (2006). Tropospheric emission spectrometer observations of the tropospheric HDO/H_2O ratio: Estimation approach and characterization [Dataset]. *Journal of Geophysical Research*, *111*(D16). https://doi.org/10.1029/2005JD006606

Wu, Y., Gao, J., Zhao, A., Niu, X., Liu, Y., Ratnasekera, D., et al. (2025). One-year continuous observations of near-surface atmospheric water vapor stable isotopes at Matara, Sri Lanka, reveal a strong link to moisture sources and convective intensity [Dataset]. *Atmospheric Chemistry and Physics*, *25*(7), 4013–4033. https://doi.org/10.5194/acp-25-4013-2025

Yao, T., Masson-Delmotte, V., Gao, J., Yu, W., Yang, X., Risi, C., et al. (2013). A review of climatic controls on $\delta^{18}O$ in precipitation over the Tibetan plateau: Observations and simulations. *Reviews of Geophysics*, *51*(4), 525–548. https://doi.org/10.1002/rog.20023

Yeo, N., Chang, E.-C., & Yoshimura, K. (2025). Application of a semi-lagrangian advection scheme for transport of stable water isotopes over the antarctic plateau in the isotope-incorporated global spectral model (IsoGSM). *Journal of Geophysical Research: Atmospheres*, *130*(14), e2024JD043154. https://doi.org/10.1029/2024JD043154

Yoshimura, K., & Kanamitsu, M. (2008). Dynamical global downscaling of global reanalysis. *Monthly Weather Review*, *136*(8), 2983–2998. https://doi.org/10.1175/2008MWR2281.1

Yoshimura, K., Kanamitsu, M., Noone, D., & Oki, T. (2008). Historical isotope simulation using reanalysis atmospheric data. *Journal of Geophysical Research*, *113*(D19). https://doi.org/10.1029/2008JD010074

Yoshimura, K., Miyazaki, S., Kanae, S., & Oki, T. (2006). Iso-matsiro, a land surface model that incorporates stable water isotopes. *Global and Planetary Change*, *51*(1–2), 90–107. https://doi.org/10.1016/j.gloplacha.2005.12.007

Yoshimura, K., Miyoshi, T., & Kanamitsu, M. (2014). Observation system simulation experiments using water vapor isotope information. *Journal of Geophysical Research: Atmospheres*, *119*(13), 7842–7862. https://doi.org/10.1002/2014JD021662

Yuan, R., Li, F., & Ye, R. (2023). Global diagnosis of land–atmosphere coupling based on water isotopes. *Scientific Reports*, *13*(1), 21319. https://doi.org/10.1038/s41598-023-48694-1

Zhang, Y., LeGrande, A. N., Goodkin, N., Nusbaumer, J., He, S., Schmidt, G. A., & Wang, X. (2025). Exploring precipitation triple oxygen isotope dynamics: Insights from GISS-E2. 1 simulations. *Journal of Advances in Modeling Earth Systems*, *17*(4), e2024MS004509. https://doi.org/10.1029/2024MS004509